Continuous Structural Evaluation of Rigid Pavements(JCP)

Submitted November 2020, in partial fulfillment of
the conditions for the award of the degree **Ph.D. Civil Engineering.**

Pawan Deep
4312531

Supervised by Nick Thom & Davide Lo Presti at University of Nottingham; Mathias B. Andersen at Dynatest Denmark & Prof. Eyal Levenberg at Danmarks Tekniske Universitet - DTU, Denmark

Nottingham Transportation Engineering Centre
University of Nottingham

I hereby declare that this dissertation is all my own work, except as indicated in the text:

Signature 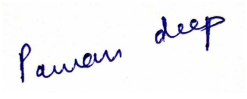

Date: 20/03/2021

I hereby declare that I have all necessary rights and consents to publicly distribute this dissertation via the University of Nottingham's e-dissertation archive.

Abstract

To evaluate the load capacity of pavements, pavement surface deflections are measured. The most common device used for measuring pavement surface deflections is the Falling weight deflectometer (FWD). However, significant attention has been given to the Rolling wheel deflectometer (RWD) type device because it can measure deflections continuously while driving at traffic speed. During the last decade, continuous deflection testing devices have shown promise as functional and structural tools to assess pavement condition at a network level. Therefore, theoretical studies demonstrating the use of RWD show it to be an effective tool to screen flexible pavement infrastructure. A complete mechanical development using RWD technology for flexible pavements has been carried out by a few industrial companies. It could be of importance to explore the significance of RWD technology for rigid pavements to expand its further usage and understand it's potential.

The idea is to evaluate the structural condition of jointed pavement by use of RWD technology. To achieve this aim, a three dimensional fast analytical forward calculation model that could be used in real-time to back-calculate these structural and load transfer parameters from the RWD measurements is used. A study of forward model validation of numerical and experimental methods demonstrates the possibility of evaluation of structural parameters. Performing experiments with a FWD and a reference beam mounted with camera-based distance measuring devices provided measurements of vertical deflections due to both a dropping weight and a loaded wheel rolling continuously across jointed rigid pavements. By using the known structural information, measurements from experimentation and the developed forward calculation model, techniques were developed for assessment of joint structural condition. Moving forward using these techniques on measurements from additional experiments by using a reference beam simultaneously with a commercial RWD equipment (designed for flexible pavement) helps to measure joint efficiency. This study is a first step in demonstrating the technical feasibility of the use of RWD technology on jointed rigid pavement assessment. A novel development for this study lies in the use of a three dimensional fast analytical model combined with continuous measurements across a structural discontinuity in the form of rigid pavement joints.

Acknowledgements

This thesis is submitted in fulfilment of the requirements for acquiring a PhD degree in civil engineering at the University of Nottingham (UNOTT). The first part of the PhD project was carried out at the department of Research and Development of Dynatest International, a pavement consulting engineering company in Denmark in the period October 1^{st} 2017 - October 31^{st} 2019. Industrial Supervisors were Mathias Bækbo Andersen, Søren Rasmussen until October 31^{st} 2019. The project continued at the department of Civil engineering (DTU Byg) at Denmark Technical University from March 2020 until December 2020. From March 2020, Professor Eyal Levenberg guided the remaining development in the aims of the research.

Throughout the whole research, Professor Nick Thom at the University of Nottingham (UNOTT) has supervised the work and research and Prof. David Lo Presti has also monitored and provided feedback on the development.

I am grateful to my supervisors for their support for different durations and roles in this research. This research collaboration has been crucial for development, experimentation and support provided by all the supervisors from the industry and University.

I am grateful to Mathias Bækbo Andersen for his regular guidance and insights into making me better at doing research. His regular feedback and opinions shaped this thesis. The team at the R&D at the Dynatest was encouraging in listening to what my thoughts were as I progressed. I would also like to thank Jack Larsen, Albert Navarro and Søren Rasmussen for their support in experiments.

At DTU- civil engineering, I am especially thankful to Professor Eyal Levenberg and Asmus Skar for the last year of the research project for their help in me continuing my project, transitioning from Dynatest.

The research presented in this report/paper/deliverable was carried out as part of the H2020-MSCA-ETN-2016. This project has received funding from the European Union's H2020 Programme for research, technological development and demonstration under grant agreement number 721493.

Contents

Abstract i

Acknowledgements iii

1 Introduction 1

1.1 Background 2

1.2 Aims 4

1.3 Structure of Thesis 6

2 Literature Review 7

2.1 Introduction 7

2.2 Joint types 8

2.2.1 Transverse contraction joints 8

2.2.2 Longitudinal joints 9

2.2.3 Construction joints 9

2.2.4 Expansion joints 9

2.2.5 Aggregate interlock between joints 10

2.2.6 Dowelled joints 12

2.2.7 Keyed joint 14

2.3 Load Transfer Efficiency 15

2.3.1 Transferred Load Efficiency 15

2.3.2 Load Transfer Efficiency or Deflection Efficiency 16

2.3.3 Load Transfer Efficiency of Stresses 17

2.3.4 Damage due to poor load transfer 19

2.4 Modelling of load transfer . . . 19
2.4.1 Based on Analytical methods . . . 19
2.4.2 Finite Element Method (FEM) . . . 21
2.4.3 Other Numerical Methods . . . 24
2.5 Devices for field measurements . . . 25
2.5.1 Deflection based method . . . 26
2.5.2 Technological development of continuous measurement devices . . . 38
2.6 Evaluation of Load transfer by field measurements . . . 41
2.6.1 Back-calculation . . . 43
2.7 Summary . . . 45

3 Methodology **48**
3.1 Objectives . . . 49
3.2 Methods . . . 49
3.2.1 Hypothesis . . . 51
3.2.2 Assumptions and limitations . . . 52

4 Modelling **54**
4.1 Boundary Value Problem . . . 54
4.2 Constitutive relations . . . 55
4.2.1 Slab . . . 55
4.2.2 Sub-grade . . . 56
4.3 Equilibrium equations . . . 57
4.4 Physics at the joints and Joint conditions . . . 60
4.4.1 Deflection transfer . . . 60
4.4.2 Moment . . . 61
4.4.3 Shear balance . . . 61
4.4.4 Assumptions . . . 61
4.5 Fourier representations . . . 62
4.5.1 Load and deflection . . . 62

4.6 Formulation 62
4.7 Implementation of analytical solution 65
4.7.1 Advantages 67
4.8 Summary 67

5 Numerical Validation 68
5.1 FEM solution 68
5.1.1 EverFE program 68
5.2 Analytical solution 69
5.3 Comparison 71
5.4 Summary 73

6 Experimental Validation 75
6.1 Test site - STAC 75
6.2 Comparison of measurements to the Analytical model 79
6.3 Summary 82

7 Experimentation 84
7.1 Measurement site- Værløse Flyvstation 85
7.2 FWD - offset load and geophone experiment 88
7.2.1 Objective 88
7.2.2 Test setup 88
7.2.3 Results 91
7.3 Reference beam mounted with laser experiment 94
7.3.1 Objective 95
7.3.2 Experimental setup 96
7.3.3 Modelled Deflections for the experiment 100
7.3.4 Results 101
7.3.5 Sensitivity of modelled deflection difference to Model parameters . 103
7.4 Rolling Wheel Deflectometer 104
7.4.1 Trailer description 106

7.4.2 Data collection devices 108
7.4.3 Calibration System 110
7.4.4 Using RWD technology for continuous evaluation of JCP pavements 112
7.5 Dynatest Raptor experiment 113
7.5.1 Objective 113
7.5.2 Continuously measured slab sections 114
7.5.3 RWD across a joint 115
7.6 Summary 119

8 Summary and Reflections **120**

Bibliography **121**

Appendices **132**

A Analytical solution for loaded slabs **132**

B Analytical solution for unloaded slab next to a loaded slab **140**

List of Tables

2.1 Summary of Major Features in Some 3DFE Concrete Pavement Models [75] 23

2.2 Comparison between the FWD and the Benkelman Beam [4] 29

2.3 Variability of Rolling Wheel Deflectometer Measurements in Research Sites at Various Testing Speeds [27] 38

2.4 General overview of existing pavement structural assessment devices [9] . . 39

2.5 Comparison of Continuous Deflection Testing Devices [26] 40

2.6 Comparison of Operating Conditions for Rolling Wheel Deflectometer and Falling Weight Deflectometer [27] 40

2.7 Summary of Moving-Load Devices for Pavement Deflection Measurements . 46

4.1 Expressions for 3D deflection response 66

5.1 Values of parameters for comparison 70

6.1 List of Model Parameters and their values used for comparison 79

7.1 Laser Specifications used in the experiment 98

List of Figures

2.1 Influence of Joint opening on effectiveness [18] 11

2.2 Deflection on the unloaded side vs deflections on the loaded side—development under wheel loading [45] 12

2.3 Load positions near jointed edge 16

2.4 Relationship between LTE based on stress and deflection 18

2.5 Relationship between compressive stresses and LTE in concrete slab under dowel for different diameters and spacing of dowel bars [55] 22

2.6 Simplified schematic of Benkelman beam 27

2.7 A Falling Weight Deflectometer(Modern version) 28

2.8 Location of Additional Sensors for Corner and Joint Testing with HWD (FAA AC 150_5370_11b) 29

2.9 Correlation between the FWD and Moving wheel deflections [6] 29

2.10 Lacroix Deflectograph 31

2.11 Schematic of a Rolling Dynamic Deflectometer 31

2.12 Curviameter (source BRRC) 32

2.13 Schematic of a Greenwood TSD 33

2.14 Detail of the sensors acquiring data close to the loading area, in the middle of a twin-wheel 34

2.15 The first rolling weight deflectometer trailer [46] 36

2.16 RWD developed by ARA and used in [85] 37

4.1 Equilibrium for bent plates 57

4.2 Bending moments and shear forces 57

4.3 An elementary parallelepiped from a plate 59
4.4 Example of a Fourier Integral 62
4.5 Coordinate system for the problem formulation 63
4.6 A typical 3D deflection response 67

5.1 Finite Element based software EverFE 70
5.2 A vertical displacement solution in EverFE 71
5.3 Analytical vs EverFE (Different LTE%, parameters fixed) 72
5.4 Comparison of 3D semi-analytical solution and FEM solution 73

6.1 Panoramic view of Instrumented Rigid pavement test site at STAC 76
6.2 The schematic of the measurement setup - Slab 1 76
6.3 The schematic of the measurement setup - Slab 2 77
6.4 Measured peak deflections (y-axis) for corner, edge and center loading from the research in [10] 78
6.5 Calculated peak deflections (y-axis) for corner, edge and center loading from the research in [10] 78
6.6 Cross-section of a rigid pavement test section by French Design method (HUGA- Humidified Untreated Graded Aggregate) 80
6.7 The two-parameter Pasternak Foundation 80
6.8 Experimental vs. 3D analytical Model deflections for Slab 1 81
6.9 Experimental vs. 3D analytical Model deflections for Slab 2 81

7.1 Apron area selected at Værløse Flyvstation 85
7.2 Satellite view of Apron area at Værløse Flyvstation (The blue line is the row of slabs, which has been used for testing in this research) 86
7.3 Ground view of Apron area Værløse Flyvstation 87
7.4 Technical drawing of the Apron pavement construction (Obtained via Forsvarsministeriets Ejendomsstyrelse) 87
7.5 Technical drawing of the pavement cross section details(Obtained via Forsvarsministeriets Ejendomsstyrelse) 87

7.6 Standard FWD Load transfer measurement test using geophones mounted on rear extension bars 89
7.7 FWD load plate drop positions relative to the Geophones (G^i) 89
7.8 Placement of the frame with Geophones across the joint 90
7.9 FWD load plate drop during the experiment next to Geophones 91
7.10 Measured Deflections by FWD Rear extension for Load transfer efficiency (LTE) 92
7.11 Center deflections for all ten drops 93
7.12 Fitting of modelled and the experimentally measured centre deflections . . 93
7.13 Fitting of full deflection bowls from 10 geophones for all ten drops 94
7.14 Centre Deflections of rigid pavement vs. increasing force for different distances to the joint(mm) 95
7.15 Non-linear Deflections of rigid pavement vs. the normalized force 96
7.16 Schematic of the Fixed beam reference Experiment 97
7.17 Coordinate system of the laser measurement system 98
7.18 Side view of the setup during experiment 99
7.19 Mounted lasers measuring during the experiment 100
7.20 Comparison of (a) modelled vs. measured deflections (b) modelled vs measured deflection difference 102
7.21 Variation of deflection difference across the joint for different (a) Subgrade stiffness k (b) Subgrade shear spring G 103
7.22 Variation of deflection difference across the joint for different (a) Slab Moduli (b) Slab thickness 104
7.23 Variation of deflection difference across the joint for different LTE 104
7.24 sketch of the RPT beam (gray line) with 3 lasers and laser beams (red lines) at times t_1 (top) and t_2 (bottom). Shown is the reference plane (full thin line), the undeflected road (thick dashed line) and the deflected road (thick full line) 105

7.25 Drawing of the load ballast placed on special rails on the lower part of the trailer . . . 107
7.26 Drawing of the load ballast placed on special rails . . . 107
7.27 Drawing of the frame of the RAPTOR trailer (Side view) . . . 107
7.28 Drawing of the frame of the RAPTOR trailer (Isotropic view from below) . 108
7.29 Picture of the RAPTOR trailer . . . 108
7.30 Available positions for the Line lasers and relative distance to the closer loading wheel . . . 109
7.31 Calibration system integrated into the RAPTOR trailer, with vertical and horizontal rails to scan a reference surface with the Line lasers. . . . 111
7.32 LTE evaluation . . . 112
7.33 Image from a Gocator inside the Dynatest RAPTOR . . . 114
7.34 A Joint tracked by 7 Raptor gocators (One column contains the measurement of a small patch of before and after including the joint i.e. dark horizontal line) . . . 114
7.35 Relative positions of gocators with respect to the joint . . . 116
7.36 Modelled and measured response by 11 Raptor gocators . . . 117
7.37 Variability in three runs (3 horizontal images) across the same joint, when measured with the Gocators . . . 118

Chapter 1

Introduction

Pavements are an important component of the infrastructure of a country. They bring about equality in society by providing an opportunity for the masses to do trade and logistical tasks in the supply chain. They facilitate people to move goods and travel safely and efficiently. Therefore pavements are crucial to the economics of a nation. They assist small business owners to grow their activity and thus increase their reach for product and services.

Huge capital and natural resources are required to construct the pavement infrastructure. Pavements require an extreme measure of planning as they are a strategic aspect of economic, political and tourism activity. This infrastructure is subject to deterioration as it takes on its role. It is thus urgent to maintain the health of pavement infrastructure as it deteriorates every year cumulatively. Of the pavement network, 3-5% is a rigid pavement, which is constructed of concrete. Concrete pavements have been used for highways, airports, streets, local roads, parking lots, industrial installations, and other types of infrastructure. When properly designed and made out of durable materials, concrete pavements can provide many decades of service with little or no maintenance. Concrete generally has a higher initial cost than asphalt, but lasts longer and has lower maintenance costs.

Rigid pavements have been an important part of pavement infrastructure over the years. As more highways have been built, they should be maintained, repaired, and reconstructed while, in many cases, allowing traffic to continue to use the roadway. The number of air-

ports and their size all across the world are increasing, particularly in the developing economies. More flights are being operated by flight operators to trim back down their operational costs and increase profits due to ever-increasing competition among the private airlines. The cost to the air travel industry of shutdowns for pavement maintenance or strengthening is a compelling reason for airport engineers to carefully anticipate the loadings and structural demands that will be made on a pavement during its design life and to design pavements to meet those demands with a minimum of future maintenance, reconstruction, and pavement strengthening. These developing scenarios have put airport infrastructure under severe pressure. Rigid pavement taxiways, runways and aprons are some of the most critical when it comes to increased traffic. Airport infrastructure will have to improve both in the management and maintenance aspects to sustain and perform under these increased demands. Rigid pavements have been becoming busier year by year.

Increasingly, construction and usage of flexible pavements have been popular, employing asphalt-based material as the top layer of pavement. In the defence aviation industry, heavy aircraft cannot be parked on flexible pavements. Military aircraft expose a pavement to heat blasts and oil spills. They require rigid pavements. Compared to military airports, in passenger airports, less construction of rigid pavement is done. Nevertheless, for passenger airports in the apron area, rigid pavement is still required. It is also required for places where operating temperatures are high and there are chances of oil spills and so on. Additionally, due to climatic changes (global warming) and tyre pressure increase (FAA reports – Navneet Garg, ICAO amendment in tyre pressure PCN classification), there is an increasing need of rigid pavements. Therefore for passenger airports, there is a gradual conversion from flexible pavements to rigid pavements.

1.1 Background

In most industrialised countries, road authorities specify that certain proportions of their highway networks be constructed in concrete. In the USA, more than 50 percent of interstate highways and 15 percent of arterial roads are constructed of concrete. Yet,

concrete pavements have in the past, (and still today according to many road engineers) been regarded as a pavement solution which is out of the ordinary and which requires greater attention than the more common asphalt pavement types. In Europe, jointed concrete pavements (JCPs) with doweled joints are commonly used. In the USA, a variety of concrete pavement types are used, which include JCPs, jointed reinforced concrete pavements (JRCPs), continuously reinforced concrete pavements (CRCPs) and even pre-stressed pavements. The performance of concrete pavements is influenced to a large extent by quality control during the construction phase [99]. However, even more important in [7], it was stated that the behaviour of joints was found to be significant in pavement behaviour as a whole. The ability of joints to transfer load not only influences the stresses in the pavement but also has, more importantly, a direct effect on the possible erosion of the sub-base material.

At many places across the world, other types of rigid pavement without joints or with fewer joints are common, for example, in France, Austria and some other countries there are kilometres of rigid pavements without joints. This is because unjointed rigid pavements are easy to maintain but costly at the time of construction. The type of rigid pavement chosen to be built is decided by the cost of maintenance. In the case of multiple one-way lanes on highways, it is impossible to stop traffic to do maintenance. There the pavement has to be such that there are no joints. One such alternative is reinforced concrete pavements for example in south of Chicago, highways have 6 lanes and there are no joints on rigid pavements. The most common type of rigid pavement is jointed plain concrete pavement as they cost less in comparison to other rigid pavements. But this pavement needs timely maintenance and checks.

There are different types of issue of pavement failure and performance issues in jointed plain concrete pavements, ranging from functional to structural issues. Faulting, cracks, corner failures, loss of slab support are some of the common issues. These mainly arise due to the poor performance of a joint caused by deterioration over the pavement use. This joint is also influenced by environmental effects such as temperature and rain. These changes affect the compression and expansion of concrete slabs due to change in temper-

ature. Additionally, if the joints are not properly sealed water enters inside the pavement through the gaps at the edges forming the joints and causes pumping action, which leads to poor slab support at the edges. This leads to deterioration faster than it would normally undergo. Thus, among 30-40% of issues arise from the joints.

Therefore, evaluation of joint structural conditions is important to prevent and slow down the deterioration. Structural condition can deteriorate due to several reasons. Reasons also depend on the type of joints used in Jointed plain concrete pavement. Vehicles continuously cross the joints on pavements and these joints act to transfer the load from one slab to the other slab as slabs cannot be continuous and thus should be joined to other slabs. Their efficiency to transfer load across the joints deteriorates as the use increases. Their ability to transfer load is a critical indicator of the joint condition. Additionally, Load transfer is one of the factors contributing to poor ride quality. A difference in the height of the surface near the slabs also known as faulting can arise due to poor load transfer. Surface cracks occurring due to poor slab support can cause discomfort to passengers. Therefore, if joints are not operating efficiently ride quality is poor. Thus, assessment of joints has been shown to provide information as they can potentially prevent the majority of defects.

By measuring the load transfer with Falling Weight Deflectometer(FWD) measurements, an assessment about the load transfer can be done and is standard practice. The FWD is a stop and go device and it will require the traffic to be stopped. However, with the ongoing development of continuous deflection measurement devices, the assessment of slabs' and joints' structural and functional condition could be more efficient compared to the classical Falling Weight Deflectometer. Measurements and testing of the network from continuous deflection devices would be fast and they have shown much promise for flexible pavements.

1.2 Aims

Joint efficiency is a major contributor to the deterioration of jointed plain concrete pavement. There are many ways to measure the efficiency, but the standard practice is to use

deflectometers, which measure the surface deflections when the pavement is loaded with sensors that touch the ground during the drop of a load detect the surface movement. These devices require the network not to be used while they measure. These devices work on all types of pavement.

As the condition of the joints and maintenance and rehabilitation processes are linked, so is the overall cost and frequency of these maintenance and rehabilitation treatments. From the structural deterioration point of view, maintenance methods depend directly or indirectly on the load transfer efficiencies of joints. The estimated service life for load transfer restoration is between 5 and 15 years [1]. The typical cost of a load transfer restoration or crack stitching is of the order of $50 to $100 per dowel bar or tie bar. Additional costs can be added due to downtime losses on the part of the airport pavement infrastructure as that part of the airport cannot be used and this leads to delays and severe management issues.

There is a growing demand and use of rigid pavement construction on highways and airport aprons. This continued use of rigid pavement requires high infrastructure quality. To meet this demand together with the client's requirements of extended performance and life expectancy requires the maintenance of the structure to be extremely thorough to ensure all specifications are met, damages are known early and unexpected failures are avoided.

To solve these issues continuous evaluation at traffic speed can help. Not only will it help to reduce the downtime, but will also reduce the overall cost to make such assessments. New technology has made it possible to measure deflections at traffic speed. So the central question here is whether continuous deflection devices can be used to assess the joint transfer in rigid pavement structures which are present in highways and airports? In this study, it is aimed to explore this possibility. It is aimed that by developing the knowledge to better measure the joint condition, the structural condition of rigid pavement, concrete slabs of highways and runway pavements, can be assessed by the use of continuous deflection measurement devices. With this research, it is aimed to answer this question.

The aim of this thesis to contribute to the effort of pavement evaluation without in-

terrupting traffic. As discussed earlier the joints are critical and need to be assessed. Therefore, this research focusses on the joint efficiency evaluation mainly. The research is focusing only on transversal joints in rigid pavement (rigid jointed) and the type of joints (transversal joints). Longitudinal joints and corner joints are physically connections, where transversal joint is a simper case to explore first and it is hoped that at first transversal joint will help us to develop the research for the other type of joints. There for continuous evaluation analysis, longitudinal and corner joints development has not been done in this thesis, but these remain promising research topics.

In particular, the research will focus on how to measure the load-transfer efficiency given that continuous measurement technology is ready for rigid pavement application. After the theoretical development is proven, then analysis of ideal experimental measurements is planned. In practical terms, measurements from the RWD (Rolling-Wheel Deflectometer) developed by Dynatest should help to understand the applicability. Simplified experiments are planned in this study to achieve the objectives which are presented after the literature review. Additionally, it is the final aim to provide a mechanical analysis tool to interpret measurements from continuous evaluation across the joints. This will help the Deflectometer manufacturers to set up the requirements on the sensing capabilities and help to analyse the data that comes from their deflectometers.

1.3 Structure of Thesis

A literature review to provide a critical summary of the state of the art, where the literature review focuses on joint types, load transfer efficiency, modelling and measuring devices is set forth. A review of maintenance and rehabilitation strategies is also performed to put the devices in the context of overall applicability. Then the methodology and objectives of the thesis are presented, highlighting the specific objectives and methodology for attaining those objectives. That is accompanied by the implementation of the model, its numerical and experimental validation and the experimentation leading to the conclusions.

Chapter 2

Literature Review

2.1 Introduction

In the previous chapter, it was established that rigid pavements network made of jointed plain concrete are key component of the network and a significant percentage of maintenance cases arise from joint inefficiency. This review starts with a re-examination of their usage and what these different types are. In the next sections, their efficiency and damage caused by inefficiency are introduced. After this modelling approaches and field measurement techniques are described. Next a review of continuous evaluation devices is introduced where the state of the art and research gaps are identified. In the final stage, a summary leading to objectives and methodology is presented.

A little discussion on design aspects is also presented later in this chapter. Design and maintenance are always linked in pavement engineering. Design of pavements can never provide a unique solution. Whenever there is a planned construction, there are typically several design choices for materials and type of pavement. All pavements require maintenance as they deteriorate and the type of deterioration will differ from design to design. Long-term performance should be emphasized along with the instant usability of pavement. While design principles are an extensive topic and cover aspects like sustainability, whole life cost and environmental factors at the same time, this research deals, especially with structural maintenance aspects. Concrete slabs are an inbuilt part of rigid pavements and need to be maintained and rehabilitated to reduce the costs. The costs of inadequate

maintenance can be huge [62]. Rigid pavements are everywhere, be it roads, highways, or airports. In different places, they have different roles. For instance, at airports, concrete slabs on taxiways and aprons take high loads from aircraft. An additional aspect of rigid pavement, considered from a maintenance perspective is to design against cracking. To put it simply, joints are designed cracks in the rigid pavement to overcome stresses due to environmental load. Hence, to avoid random cracking it is desirable to design these cracks in the form of joints. Various studies have been done to explain and understand structural behaviour, be it dowelled joints or aggregate interlocking and how to maintain such rigid pavement infrastructures.

2.2 Joint types

Maintenance of structural aspects is associated with the different designs of load transfer and the failure types that arise when the infrastructure is exposed to load and environmental conditions. Here a review of joint load transfer mechanisms such as aggregate interlock, dowelled joints and keyed joints will be presented. Environmental conditions acting on the infrastructure leading to cracking and faulting, are also presented. These themes are however often interdependent and influence the structural condition and performance of the rigid pavement.

2.2.1 Transverse contraction joints

A transverse contraction joint is a joint that is sawed, formed, or grooved in a concrete slab. The joint creates a weak vertical plane and a point of high stress where cracks initiate and propagate from. Contraction joints regulate the location of cracks formed due to dimensional changes caused by temperature and moisture changes in the concrete. Transverse joints in highways are used perpendicular to the direction of traffic, while longitudinal joints are placed parallel to the traffic and between traffic lanes. Airport pavements are much wider and use square concrete slabs that could be joined by aggregate interlock or dowels in transverse direction. Due to the cost, the aggregate interlock joint

is the most frequent solution adopted.

2.2.2 Longitudinal joints

Longitudinal joints are constructed between two slabs and allow the slabs to warp or deform without significant separation or cracking of the slabs. Although load transfer at longitudinal joints is achieved through aggregate interlock, tie-bars are commonly used across longitudinal joints to prevent slab separation and faulting. The tie-bars are usually thinner and longer deformed steel bars, unlike smooth and bigger diameter dowels. Tie-bars can also be epoxy coated for corrosion protection. Longitudinal joints can be sawn or constructed similar to transverse joints. For sawn joints, the tie-bars are pre-set in tie-bar baskets similar to dowels. Otherwise, they can be mechanically inserted at slab mid-depth to connect the old and new concrete slabs together.

2.2.3 Construction joints

Construction joints are either transverse or longitudinal joints that result when concrete is placed at different times. A good practice is that transverse construction joints should be placed where a planned contraction joint should be located. Construction joints should not be skewed due to the difficulty in construction and concrete consolidation. Transverse construction joints should be doweled, butted, but not keyed. A strong correlation has been obtained between [16] LTE along the longitudinal construction joint and slab edge deflections. A good correlation was also obtained between LTE and slab settlement. This finding signifies the importance of LTE along longitudinal joints, which could be improved substantially with better tie bar design.

2.2.4 Expansion joints

An expansion (or isolation) joint is a joint placed at a specific location to allow the pavement to expand without damaging adjacent structures such as bridges, drainage, and utility structures or the pavement itself. Properly designed and maintained contraction joints have practically eliminated the need for expansion joints, except at fixed objects

such as structures. As the pavement expands due to temperature and moisture changes, the expansion joints will tend to close over a period of several years. As this happens, adjoining contraction joints may open, which may destroy the joint seals and aggregate interlock. A special type of dowel assembly transfers load across expansion joints. The special joint dowel system is fabricated with a cap on one end of each dowel to create a void in the slab to accommodate the dowel as the adjacent slab closes the expansion joint.

2.2.5 Aggregate interlock between joints

Aggregate interlock is achieved through frictional shearing forces at the aggregate–paste interface that develops below a joint saw cut. If joints are typically saw-cut 1/4–1/3 of the way through the slab depth, then a crack develops naturally through the remainder of the slab depth. Aggregate interlock helps to transfer load through shear forces. Load transfer also depends on several parameters such as load magnitude, number of load repetitions, joint opening and other design parameters. A study relating the above mentioned designed parameters and effectiveness of joint is shown [18] in Fig 2.1. Load transfer effectiveness was rated using joint effectiveness and is computed using the formula

$$E(\%) = \frac{2d'_j}{d_j + d'_j} * 100$$

, where d'_j is the deflection of the unloaded slab and d_j is the deflection of the loaded slab. If load transfer at a joint were perfect, the deflections of the loaded and unloaded slabs would be equal and the effectiveness would be 100 percent. If, however, there were no load transfer at a joint, only the loaded slab would deflect and the effectiveness would be zero. All effectiveness values are computed from measured deflections.

These experimental results are used in the design and modelling of the joint. The constitutive behaviour of this interlock has been studied [94], for which as an applicable model has been recognized in [20]. A Finite element model of jointed concrete pavement with an aggregate interlocking load transfer system has demonstrated the dependency of design parameters such as aggregate size and modulus of interlocking [61]. This interlocking

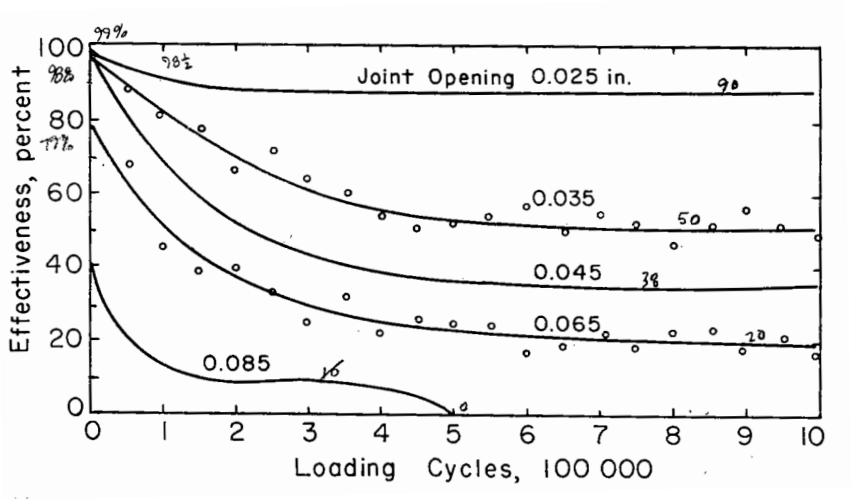

Figure 2.1: Influence of Joint opening on effectiveness [18]

simulated using a finite element model has also been studied for cracks by using a constitutive model [94] with different positional loading conditions and times of the day, all affecting the load transfer efficiency of the joint. This study, however, can help in the development of rational failure criteria.

Non-linearity of load transfer behaviour has been explored demonstrating the initial free slip until the two crack faces are in contact and then sliding as the crack is subjected to continuous loading, followed by dilation or build-up of normal stresses in the crack [45]. It is shown in Fig 2.2. The mechanisms of aggregate interlock were analyzed from continuous measurements of load and deflections, and the mechanisms of aggregate interlock are quantified through measures of wheel load and displacements across the crack. The development of deflections on either side of the crack as affected by crack width is shown in Fig. 2.2. For the sake of illustration, the deflections have been normalized by the free edge deflection. Three different behaviors are observed. For small crack widths, the two deflections develop with the same rate, resulting in a 1:1 slope. For increasing crack widths, the unloaded slab segment is not engaged before the loaded slab side has deflected a given distance denoted as the initial free slip. However, when the unloaded slab segment is engaged, the two sides deflect at an equal rate, that results in a 1:1 slope on the second part of the deflection curve. For large crack widths of 2.5 mm, the loaded side keeps deflecting at a higher rate than the unloaded side. The amount of initial free

slip and sliding is dictated by the properties of the crack such as crack width and crack roughness.

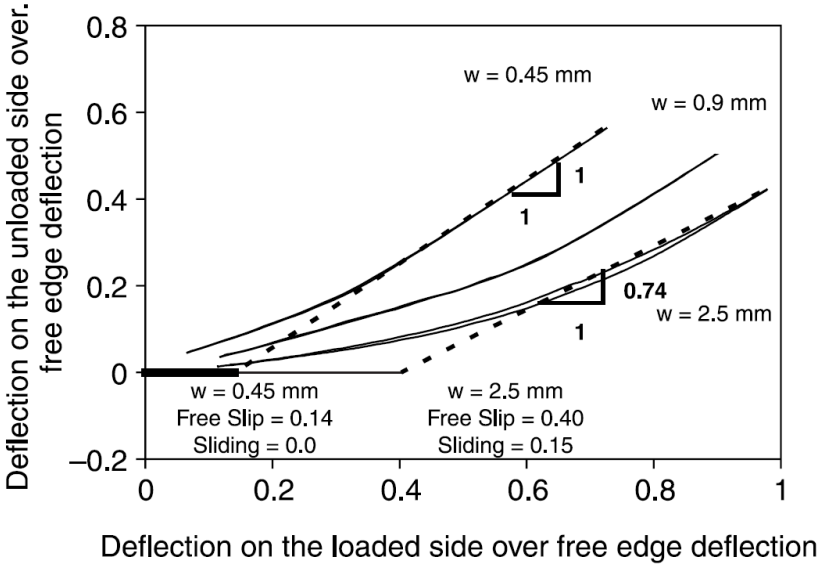

Figure 2.2: Deflection on the unloaded side vs deflections on the loaded side—development under wheel loading [45]

In this study, there was no data available on continuous measurements of wheel load and crack displacement and in general, the measured slab deflections were significantly larger than those observed in the field.

2.2.6 Dowelled joints

Dowels are used in transverse joints to enhance load transfer across the joint and prevent pumping and faulting distress (see Figure 3.16). Dowels are typically smooth metal rods that are lubricated to permit movement along the dowel's longitudinal axis and allow joints to open and close without stress build-up. The earliest mechanistic approach for designing dowelled transverse joints was developed by assuming an equal deflection of both the edges of jointed concrete slabs. It was concluded that only the two closest dowels on each side of a point load at the joint edge are active during load transfer [95]. Dowels lying within 1.8 times the radius of relative stiffness are effective in load transfer. Mathematical equations were also presented in this study [30]. To understand the distribution of load

transfer, a similar study was carried out [52]. A two-dimensional FEM study of the dowels was carried out where earlier assumptions and relationships were validated about dowel position and the radius of relative stiffness [86]. Load Transfer Efficiency (LTE) as a parameter was introduced in the calculation of compressive stress [44]. FEM was demonstrated to be a powerful method to predict dowel behaviour and be usable in design including non-linearity[14]. Non-linear behaviour was also explored concerning dowel looseness as a parameter [36]. Accuracy of earlier design procedures using the component model was developed and tested [35], [37]. Parameters like dowel diameter, slab thickness, concrete modulus, subgrade modulus were shown to affect the maximum bearing stress of the concrete under the critical dowel. It was also demonstrated that the Joint opening is not affected by the maximum bearing stress, but is sensitive to the dowel-concrete interaction. The radius of relative stiffness was shown to underestimate the maximum bearing stress.

A FEM program **EverFE** simulated the dowel alignment and dowel looseness in a series of studies [23] and [24]. In another study, a 3D FEM software PAVE3D which uses a mechanical model for dowel bars in the transverse joints of concrete pavement provided further insight about the influence of subgrade stiffness on both concrete slabs and the dowels [66]. Increasing the rigidity of the sub-base decreases the stresses in both dowel bars and the concrete slabs. By using 3D FEM contact element modelling, stresses were studied between dowels and concrete interfaces and a modified dowel design that reduces the intensity of concrete contact stresses was proposed in [76]. Similar studies utilizing 3D FEM with more powerful computers have shown that LTE is a function of dowel spacing and modulus of dowel support [60]. Dowel looseness and modulus of dowel support are inversely proportional to LTE. Maximum shear force taken by the dowel just below the load depends on pavement configuration and can be expressed in terms of the radius of relative stiffness, dowel spacing and relative stiffness of dowel and concrete. With the help of FEM, an attempt to reduce the friction at the concrete-dowel interfaces while maintaining the LTE was shown [8]. Compressive and tensile stresses surrounding the dowel are explored using FEM in [56] and these stress components were found to be more

influential in initiating cracks in concrete. By using a double layer pavement model and controlling three-dimensional positional parameters of dowels such as horizontal angle, vertical angle and embedded depth, joint load-transfer capacity was analysed and verified against experiments conducted with a Falling Weight deflectometer in [101]. Although these intricate developments and results from FEM are used in design processes, at the same time, they do not help in back-calculation of parameters from a maintenance point of view as FEM is computationally costly at the network level and ineffective for this purpose.

2.2.7 Keyed joint

To analyse the behaviour of keyed joints against dowel joints, by using numerical models in [67], characteristics of the load transfer efficiency were studied. If the aircraft gear loads are applied near a joint, the maximum tensile stresses in both the dowel and key joint slabs are almost the same when there is no joint gap. Once there is a joint gap, the dowel joint slabs are not much affected by the joint gap size; however, for the key joint slabs, the maximum tensile stresses become larger as the joint gap increases. If the aircraft gear loads are applied to the interior of a slab, the maximum tensile stresses increase slightly if there is a joint gap, but the joint gap size does not affect the maximum tensile stresses. The maximum tensile stresses of both the dowel and key joint slabs are the same under the interior aircraft gear loads.

If vertical temperature gradients are applied in two-slab pavement models, the maximum tensile stresses are almost the same for both the dowel and key joint slabs, and once there is a joint gap, the maximum tensile stress increases slightly, but the size of the joint gap does not affect the maximum tensile stresses. The maximum tensile stresses of both the dowel and key joint slabs increase under the combined loads of the joint gear loads and positive temperature gradient, and they decrease under the combined loads of the joint gear loads and negative temperature gradient compared to those under only one type of load. When the joint gear loads and positive temperature gradient are applied at the same time, the key joint slabs have larger maximum tensile stresses than the dowel joint slabs

as the joint gap increases. Therefore, the use of dowel joint pavement is recommended to mitigate failures observed in key joint pavements and to improve the performance of rigid pavements. Keyed joints have also been studied under Rolling Dynamic Deflectometer [4].

2.3 Load Transfer Efficiency

Efficient joints deflect the same on each side of the joint whereas poor joints do not deflect the same. The way to quantify and measure the joint efficiency depends upon how the definitions have been set up. Here follows a quick description of these terms and definitions.

- Transferred Load Efficiency
- Load Transfer Efficiency
- Load Transfer Efficiency based on stresses

2.3.1 Transferred Load Efficiency

The setup in Fig. 2.3 where point and circular pressure loads are shown are two configurations A, B as point loads and A' and B' as pressure loads. There are two slabs and there is a joint between them. The loaded slab 1 is denoted as L and the unloaded slab 2 as U. The point force A is placed at the edge. The load is applied on the one side close to the edge, close to the joint. Imagine that the load applied is a point load(B), that is applied to the loaded side close to the edge and then let's imagine that this load splits into two, then there are two loads P_U and P_L, both of them arising from the one that is applied, but because this is so close to the edge, it can be imagined that they are split. First, one load P_L is the load carried by the loaded slab and the P_U is carried by the unloaded side. The sum of these is the applied total load. It is not sophisticated but if the applied load (P_T) and $P_U = 0$, that means that the unloaded side doesn't take any part of the load coming onto it. It means the joint has zero efficiency for transferring loads. If there is

any transfer between the two, then they share the work and if this is 50%-50%, then it is the most efficient joint. This is the definition of transferred load efficiency. It is defined as P_U/P_T. The same definition applies to the pressure load as well.

If there is a 100% efficient joint, transferred load efficiency would be 50%. That means that 50% of the applied load is carried by the unloaded slab. The joint is so efficient that every load that comes to the joint is split into two equal parts.

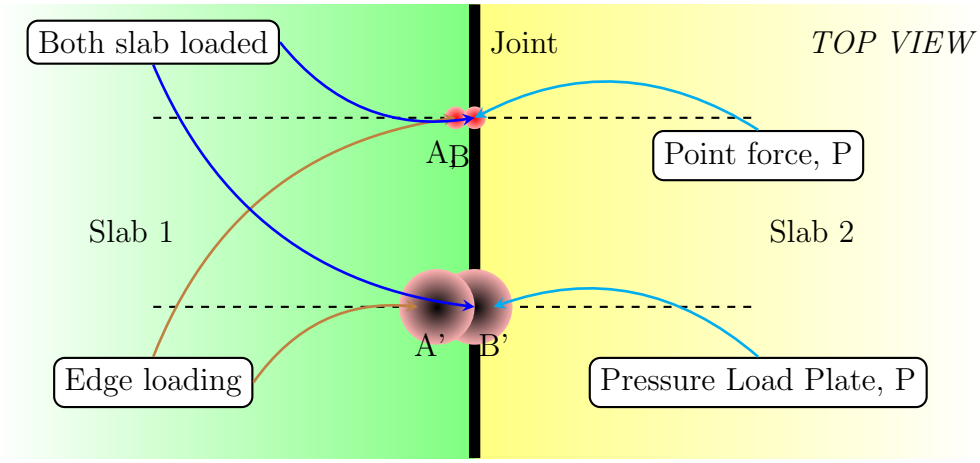

Figure 2.3: Load positions near jointed edge

2.3.2 Load Transfer Efficiency or Deflection Efficiency

From the physics of deformation point of view, deflection results from the load applied to the elastic continuum body and the stresses from the load produce the strains in all directions. The concrete slabs are plate-like structures supported by a soil foundation, therefore concrete deformation in the direction parallel to the load is termed here as 'deflection' for ease of understanding. Here load transfer efficiency is defined by the ratio of vertical deflections. It is defined as δ_U/δ_L. Deflection at the edge of the unloaded side divided by deflection in the unloaded side is the definition of the load transfer efficiency with respect to the deflections. $\delta_L + \delta_U = \delta_e$, where δ_e is the maximum deflection for an edge case. 'Edge case' means there is no slab adjacent to it. So if there are two plates and there is a joint between them and the load is applied on the loaded side as a point load, calculation of the deflections is possible if the efficiency is zero. In that case, then P_L is

non-zero and $P_U = 0$ given it is an edge case. If there is some part of the load going to the other side there will be a distribution. The edge deflection equation is assumed to be linear with P. There is a connection between the deflection on the loaded side, efficiency of the joint and the deflection for an edge case.

So for a 100% efficient joint $LTE_\delta = 100\%$, then the deflection will be half that of an edge case. $\delta_L = \delta_U = \frac{1}{2}\delta_e$ and if $LTE_\delta = 0\%$, then the loaded side deflection would be equal to the edge case loading and the other side would not be affected at all. Westergaard gave an analysis of this case of transfer efficiency. Imagine that there are two plates, and they are connected by springs at the joint, what happens when one side is loaded, then this spring is responsible for the transfer efficiency. If the spring stiffness value here is 0, there is no spring, then they are completely independent. If the spring stiffness is infinite, this means that these two are connected and both edges would be deflecting identically. The formula for spring stiffness has the unit of force per unit length. The spring will only work if there is a difference between these deflections.

One of the practical aspects in the concrete pavement industry is that if there is a joint in an old concrete pavement or even in a new one, it is important to know what the efficiency of this joint is. If a load of known value is placed close to the edge on one side, that side becomes the loaded slab. The deformation generated by the load on both loaded and unloaded slabs at the same time can be measured. The deformation measured on two sides of the joint represented as δ_L and δ_U is obtained and if measured values are accurate, the efficiency of the joint is known from the deflections. Spring stiffness values can be calculated as a ratio of subgrade stiffness to radius of relative stiffness and this can assist in calculating the transferred load efficiency.

2.3.3 Load Transfer Efficiency of Stresses

For the LTE based on stresses, stresses need to be calculated. This efficiency is simply the ratio of slab edge stresses on the unloaded side to the loaded side. Therefore, this is a transferred efficiency concerning the bending. As has been mentioned before, if the loads applied are point forces, then the stresses will be infinity. So this measure of load transfer

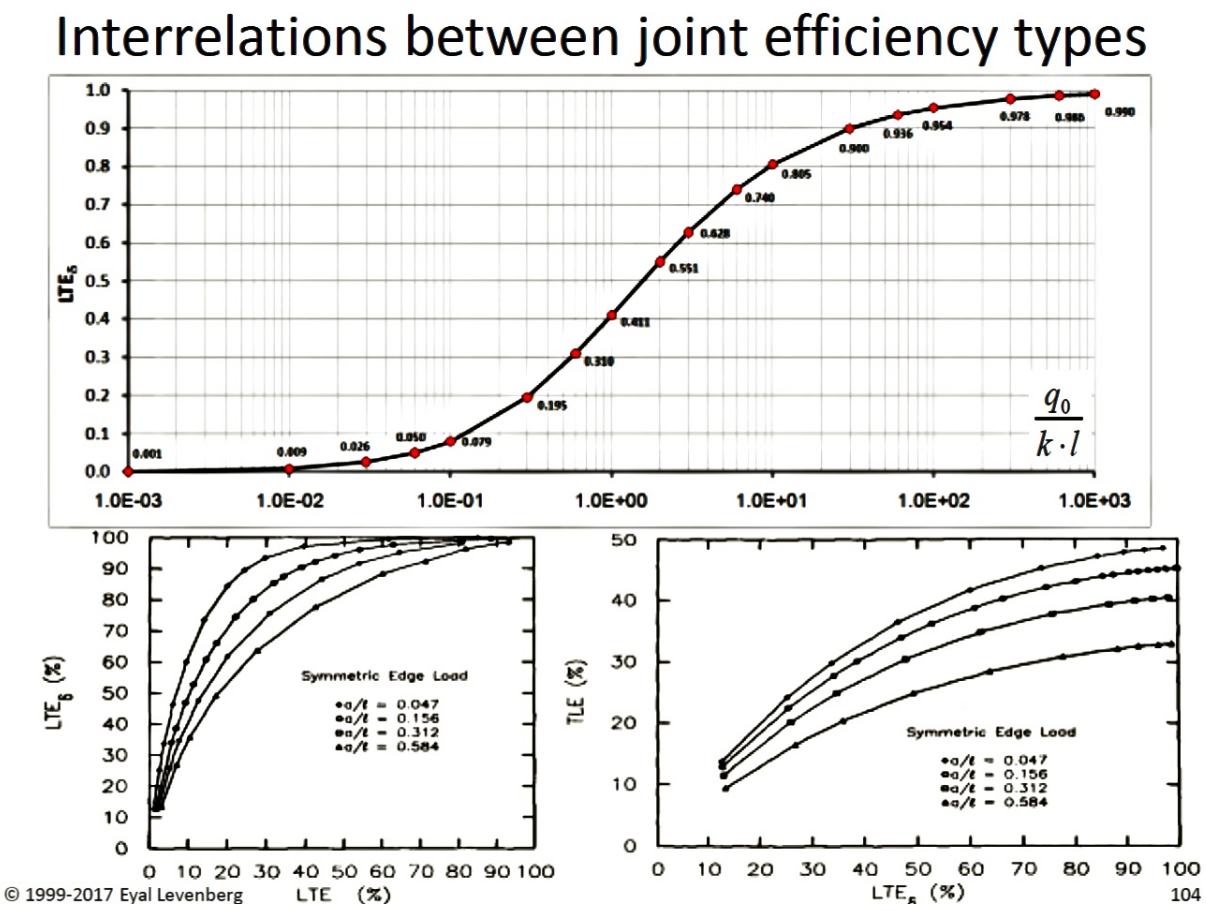

Figure 2.4: Relationship between LTE based on stress and deflection

does not apply to point forces, but to loads over a circular area or other areas as in cases A' and B' in Fig. 2.3. There exists a relationship between the stress on the unloaded side and the stress on the loaded side. That is to say that by summing these the edge case stresses can be obtained in a similar way as for deflection. So Westergaard's solution for the edge case stress can be used. The sum of bending stresses on each side of the joint is equal to Westergaard's solution for the edge case. Using these formulae, the relationship can be expressed as in Figure 2.4.

It is routine engineering practice in the concrete pavement business to test joint efficiency. Engineers bring the Falling Weight Deflectometer and they place the loading area next to a joint. They apply a load and measure using geophones on the loaded side and unloaded side. The ratio between the deflections is directly related to other definitions through the charts in Figure 2.4. The loading shape is a circle and its area is known, so by knowing radius(a), information about the radius of relative stiffness l is known. Deflection calcu-

lated from the point load solution also works fine. The force load can also be considered, but then the Westergaard's correction needs to be taken into account. Westergaard had demonstrated that if the load is applied in a small region then a correction is to be used, that is to use a fictitious area, which can be done here as well.

2.3.4 Damage due to poor load transfer

The failures in rigid pavement can arrive from different sources including exposure of pavement to weather conditions. Problems such as faulting, cracks, subgrade de-stabilization, water ingressing, void creation below the slabs, joint gap widening, joint opening, dowel loosening and degradation of joint transfer mechanisms eg. tie bar, dowels, can occur. If the load transfer is poor then these issues can become more pervasive and frequent.

2.4 Modelling of load transfer

2.4.1 Based on Analytical methods

Westergaard's solutions for structural responses of a rigid slab resting on a Winkler foundation [97], [98], [96] have been widely applied in the analysis and design of concrete pavement. Theoretical solutions to an improved model for rigid slab supported on a Pasternak foundation [69], one solution for vertically applied loads and another for thermal loading, have been supplied by [74]. In [74], the analytical solution developed is valid for an arbitrary vertical load applied at any point along the thick plate. The underlying equations for the thick plate on Pasternak foundation were established by applying the variational principle of Reissner [70]. A Pasternak foundation allows a transverse connection in the supporting subgrade or subbase layer of a slab to be considered in addition to the modulus of subgrade reaction. A Winkler foundation is a special example of the more general Pasternak foundation.

In [33], an improvement over the work by [74] led to a novel way to estimate the shear parameter for a Pasternak foundation. Additionally, a relationship was developed for finite slab dimensions, which particularly improved the model. But the whole development was

for a free edge of finite dimensions. For this research, a model where load transfer is handled analytically is preferred. Thus a free edge condition cannot be used.

In [34], two semi-infinite slabs resting on a Winkler foundation were represented. This example implementation is based on analytical formulation and is derived from Westergaard's earlier work. Here, the implementation is for a point load with joint parameter based on a joint stiffness as input. This model requires improvement for continuous evaluation measurements to be used. In such evaluation, load and sensors are not in the same plane. The distance between the sensors and load is less than the radius of the relative stiffness of pavements. Another measure that will be required is to link the stiffness-based relationship for joints to a deflection based relationship because a deflection ratio is easy to measure. Fortunately, there already exists such a relationship in [43], where a non-dimensional relationship between load transfer efficiency as a function of non-dimensional joint stiffness has been demonstrated.

Given these shortcomings, an analytical model presented in [34] based on a simpler formulation could be useful. In [13], the formulation uses semi-infinite plates resting on the Pasternak foundation. However, this formulation is not implemented in [13]. This model formulation uses a pressure load and the load transfer is modelled by a deflection ratio parameter. This model formulation if implemented, could offer a solution for deflections as a pavement response from a 3D analytical forward model. It would require a load transfer as an input parameter, which does deliver an advantage because the focus of this research to measure joint efficiency while moving continuously. Even so, this model does not study how deflection based load transfer efficiency values change, when position of load is changing. It is however known that load transfer is not constant for different distances of the load positions to the joint.

With the knowledge of the shear parameter with finite slab size in [33], resting on a Pasternak foundation, it is possible to use that as an input in [13]. Thus, if this model is implemented it would be an ideal tool to predict the pavement response and measure joint efficiency. The inputs for this model for deflection ratio can always be related to joint stiffness [43].

2.4.2 Finite Element Method (FEM)

A three dimensional FEM with commercial code such ABAQUS can simulated jointed concrete pavement with discontinuities. The deflection modelled under a Falling weight deflectometer load and both static and dynamic loading has been simulated [87]. Transverse joints with dowel bars have been simulated using the gap elements. Then, a static and dynamic back-calculation has been carried out to show that a lower back-calculated modulus is expected in the cracked pavement. Such analysis can not be carried out by using traditional multi-layered elastic analysis [90].

A versatile and open-source interactive rigid pavement tool 'EverFE' was developed using 3D FEM. The tool uses a novel technique for modelling aggregate interlock joint shear transfer [21]. Modelling of dowels is also possible and a solution strategy is developed allowing the efficient and rigorous consideration of dowel/slab interaction. Both a layered elastic with an asphalt treated base and a dense liquid foundation can be used. A parametric study considering the effect of slab curling and foundation type is shown in [24], on joint load transfer. In [24], the potential for fatigue damage to the concrete surrounding the dowels is quantified. Thus, it is concluded that a stiff base is less prone to experience dowel looseness and damage to the concrete surrounding the dowels.

An FEM based solution [41] determined the stresses and deflections in multiple slabs resting on elastic solids when the load was applied at different distances to the pavement edge. It was concluded that if the partial contact is modelled then the computed deflections are close to the measured deflections. Stresses around the dowels are a major factor that contributes to transverse joint stiffnesses. Moreover, these stresses contribute to crack initiation and propagation and has been studied using FEM [56]. Dowel length is shown to be susceptible to tensile stresses and dowel diameter is susceptible to compressive stresses . When the transfer is by aggregate interlocking, even then it is possible to model that by using advanced models. A cohesive zone model to describe the fracture of cement bound mixtures and an idealized finite element model has been developed [82] and shown to describe the structural subjected to heavy loads. This model also includes a cyclic formulation of the cohesive zone and aggregate interlock behaviour and can be

used for the development of more rational failure criteria. Multiple slabs, dowel misalignment, nonlinear thermal shrinkage gradient and nonlinear horizontal shear stress transfer between slabs and base has been studied in [22].

The effects of different parameters on the load transfer efficiency of a joint with the help of a three-dimensional finite-element model for the analysis of a dowel-jointed concrete pavement has also been studied [60]. The model was compared to experimental data available in the literature. LTE decreases with increase in DL and increases with the increase in modulus of dowel support. The maximum shear taken by the dowel just below the load depends on pavement configuration expressed in terms of the radius of relative stiffness, dowel spacing and relative stiffness of dowel and concrete.

To understand the nature and magnitude of the stresses at the dowel-concrete interface in rigid pavement joints, the influence of different diameters and spacing of dowel bars on the slab interaction was considered by [55]. Calculations were carried out with the application of a 3D Finite Element Method. Dowels with small diameters can result in damage in the concrete slab because of the high concentration of vertical compressive stresses. It was seen that considerable compressive stresses (>10 MPa) appear in a concrete slab under dowel with diameters smaller than 0.025 m for LTE < 75 %. Vayring dowel spacing and diameters, a change of LTE from 95 to 70 % was observed. A relationship allows stresses

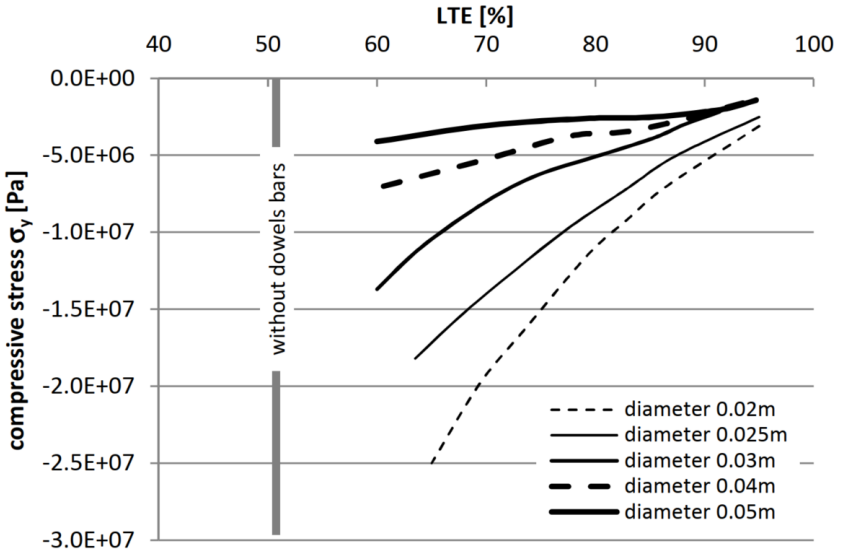

Figure 2.5: Relationship between compressive stresses and LTE in concrete slab under dowel for different diameters and spacing of dowel bars [55]

	Loading			Gradient				Dowel Bars			Interfaces		
Source	Static	FWD impact	Superposition of pulses	Linear+static load	Thermal gradient only	Nonlinear+FWD load	Nonlinear+moving load	Spring	Beam/embedded formulation	Brick	Dowel bar-concrete	Concrete-base	Winkler foundation
Ioannides and Donelly (1988)	●												●
Chatti (1992)			●						●			●	●
Channakeshava et al. (1993)	●			●					●		●		●
Zaghloul et al. (1994)			●						●			●	
Darter et al. (1995)	●				●				●			●	●
Masad et al. (1996)					●							●	
Hammons (1997)	●							●			●	●	●
Kennedy and Everhart (1998)			●									●	
Uddin et al. (1997)		●							●		●	●	
Sargand and Beegle (1998)			●					●				●	
Davids (1998, 2000)	●			●					●			●	●
Lee et al. (1998)	●											●	
Brill and Parsons (2000)	●								●			●	
Shoukry (2000)		●				●				●	●	●	

Table 2.1: Summary of Major Features in Some 3DFE Concrete Pavement Models [75]

in concrete to be efficiently determined under a dowel based on its diameter and LTE. It is shown in Fig. 2.5.

Increased computing power allows taking account of nonlinearity in numerical modelling. Nonlinear Finite Element Analysis of dowel jointed concrete pavement includes nonlinearities arising from distresses such as cracking of the concrete, compressive yielding of concrete and loss of support at the end of concrete slabs due to lift offs. This distress generates local deformations of concrete around the dowels at the joint. This dowel concrete stiffness has been shown to affect the deflection profiles [14]. Similar efforts have been carried out with the addition of cyclic loading considering nonlinear fatigue damage accumulation [5]. A more advanced study employing the general-purpose nonlinear explicit finite element equation solver 'LS-DYNA' has solved a model which includes the combined effect of non-linear thermal gradient and moving axle load [75].

In Table 2.1, a summary with an overall classification of FEM development literature based on modelling of loading categories, gradient modelling including thermal, nonlinearity and moving load is shown, plus classification based on dowel bar modelling and interface modelling concerning the sub-base and foundation types. This presents an overview of the current state of FEM modelling.

It is clear from the FEM based models that they are accurate, accessible and easy to implement. However, fewer FEM models have been used in the inverse analysis of measurements. Theoretically, it is possible and a good line of research to explore. Additionally, FEM models include complexity when it comes to discontinuities in the domain

and using such models for inverse analysis might be difficult and time-consuming. The focal point of the research is to measure the joint efficiency and that constitutes a discontinuity in the model domain. A FEM model can predict response and then possibly back-calculate from measurements, but when such a tool is intended for continuous evaluation, the model should be fast for inverse analysis because the forward model needs to be calculated many times for each measurement set. In the next section, a review of field techniques to measure rigid pavement response and joint efficiency is presented.

2.4.3 Other Numerical Methods

In [37], comparison between experimental and analytical results has verified that a component model, which was developed to simulate the dowelled joints, can reasonably predict the state of a dowel bar load transfer system. It was concluded that the neglect of the equilibrium condition in the dowel-bar stiffness matrix causes significant differences in the prediction of dowel-bar forces and critical slab stresses. The bending beam model should be replaced by a shear-bending beam to simulate the dowel segment in the joint (between two slabs). A good concept to simulate the dowel-bar mechanism is shown in detail in [65]. But, the error in their derivation should be corrected. The bending beam model should be replaced by a shear-bending beam to simulate the dowel segment in the joint (between two slabs).

A double-layer structure model of pavements that considered interlayer contact status was established [102], to manage the dowel-bar position deviation problem in rigid pavements. The deviation effect of three-dimensional positions, such as horizontal angle, vertical angle, and embedded depth, on joint load-transfer capacity, was analysed. By contrast, the joint load-transfer coefficient decreased almost linearly as the vertical angle increased. The coefficient reduced by approximately 12% when the vertical angle was 15°. Meanwhile, the load-transfer coefficient was maximized when a dowel bar was embedded in the middle of a surface. The coefficient would decline either upward or downward. The coefficient decreased by 10% when the position was 2 cm downward.

2.5 Devices for field measurements

To measure the pavement response from the surface by using sensors with contact or non-contact for structural monitoring of top layers and sub-layers requires a knowledge of the aim of the measurements. For rigid pavements, these can be the measurement of structural and functional defects. Detection of these defects is essential because any signs of weakening can lead to problems requiring expensive maintenance and reclamation. These problems can be figured out by performing field tests with measuring devices, analysing measured data and then arriving at conclusions from the tests. The analysis of measurements requires forward modelling of the pavement, which is utilized in the back-calculation/ inverse analysis.

Structural evaluation methods can be categorized by technology, measurement entity or application area. Categorization of measurement methods/devices by a single aspect is challenging, for instance, if the measurement aims to know about long term residual calculations. This calculation requires measuring devices such as the STBA trailer, which provides information about fatigue behaviour and therefore an indication of future performance [54]. The measurements will be aimed at fatigue calculations. As another example, for determination of layer stiffness, surface wave velocity needs to be measured by devices. A few devices measure surface wave propagation velocity at small strain, hence as the material stiffness is in the elastic range, by knowing the wave speed stiffness can be calculated from the measurements. One of such devices is Seismic Pavement Analyzer [64]. Layer stiffness can also be measured by devices that measure surface deflection in a vertical direction, which likewise can provide engineers with knowledge about layers and subgrade conditions. These devices, though they provide the same conclusions about layers, target different measuring quantities. Thus, different measurable quantities are produced via different methods. These methods can host a range of measuring technology. Technology based on deflection measurement is chosen to be reviewed as this research intends to measure the joint efficiency, which is defined using deformations in the sense of vertical deflection, devices measuring deflections as a raw quantity are presented next.

Devices use sensors that measure a raw quantity and then these sensor measurements

are interpreted to make sense of the information. These sensor measurements in raw form may or may not be deflections. Deflections are anticipated as the final output, but the raw measurement might not be the deflection but something else. For example, geophones measure surface velocity, which is integrated to provide deflections. In the review presented in the next section, discussions on sensor technology are avoided.

2.5.1 Deflection based method

Deflection-based Nondestructive Testing (NDT) methods involve application of force on a pavement surface to measure vertical deflections. The surface deflection information is used to detect weak portions of the pavement, evaluate the modulus of pavement layers, estimate the modulus of subgrade reaction, and the load transfer efficiency of joints in Jointed Concrete Pavement (JCP) and cracks in Continuous Reinforced Concrete Pavement (CRCP). Moreover, the shape and magnitude of the deflections are functions of traffic and environmental effects, pavement structural capacity, and subgrade conditions. These conditions can wreak havoc on rigid pavements as rigid pavements use concrete. Therefore to evaluate JCP, deflection-based NDT methods can generally be divided into two groups, discrete testing devices which stop to apply the forces and measure slab deflections (hence, stationary devices) and continuous testing devices which apply forces and measure pavement deflections while the device is moving along the pavement.

Discrete Pavement Deflection Testing Devices

1. **Benkelman Beam** This device developed by A.C. Benkelman in 1953 was used in the WASHO road test. Using this device during the test, the moving truck wheel applied the load on the pavement and the deflected pavement surface was measured by a stationary dial gauge. This device is composed of a stationary reference frame and a probe arm pivoting at one point supported by the reference frame.

   A major limitation of the Benkelman beam is the inability to determine the entire deflection basin and avoid front support interference with the deflection basin. Furthermore, it was found that the Benkelman beam is unable to measure the deflection

in thick rigid pavements [72]. As a solution to this problem, two or more beams were joined to conduct the test. Simplicity and low cost are major advantages of this type of deflection testing with a daily production of 50-100 test points using a crew of three technicians [83]. This number of test points can suffice as a tool for measuring joint efficiency in developing countries as a low cost alternative [48]. An example of Benkelman beam is shown in Fig. 2.6.

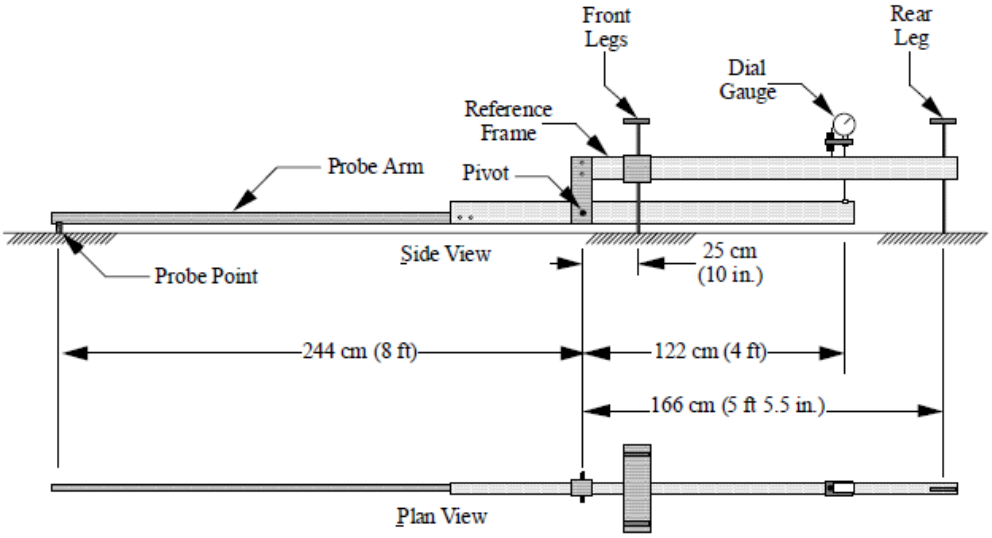

Figure 2.6: Simplified schematic of Benkelman beam

2. **Falling Weight Deflectometer (FWD)** This was first developed to measure pavement surface deflection at airports, due to aircraft loading while moving at intermediate speeds. FWD devices consist of the following four main components, An impulsive-force generator that enables application of variable weights to the pavement surface from different heights, a loading plate to spread the impulsive-force uniformly through the tested layer surface, three or more sensors (currently available FWD devices have up to 9 sensors) for deflection basin determination, data acquisition, processing, and storage system. The FWD has been commercialized and sold by different manufacturers and has been used for many years. A modern device manufactured by Dynatest is shown in Fig. 2.7. Dynatest manufactures both a FWD and a HWD with models that generate dynamic loads up to 54,000 lb (240 kN). The weights are dropped onto a rubber buffer system. Seven to nine velocity

transducers are then used to measure the load and dynamic response. The test is repeated several times, and the results are averaged. Tests may also be performed using different drop heights, and hence different force levels, at each testing location. After testing is complete, the loading plate and sensors are raised, and the device is towed to the next test location. After field testing is complete, FWD data are prepared for the analysis phase. Several analysis tools and software packages are used by highway agencies for performing both back-calculation and forward calculation, calculating load transfer efficiency, and assisting in quality control and assurance purposes.

Figure 2.7: A Falling Weight Deflectometer(Modern version)

The HWD Non Destructive Test(NDT) plan may require tests to be performed at the center, corner, transverse joint, and longitudinal joints of PCC slabs. These tests may also have to be performed at these locations for Hot Mix Asphalt overlaid PCC when cracks have reflected to the surface from underlying joints. The manufacturer's NDT devices and operation software may permit additional sensors to be installed on both sides and behind the load plate, as shown in Fig 2.8.

Table 2.2 is a comparison of the principles of the discrete deflection measuring devices. The basic idea behind the FWD was to simulate the moving impulsive load and this has been studied theoretically. The validity of comparing the effect of the falling weight to the effect of a moving wheel load has been investigated by two means, both showing good correlation between the two effects [6]. This correlation is shown in Fig.2.9.

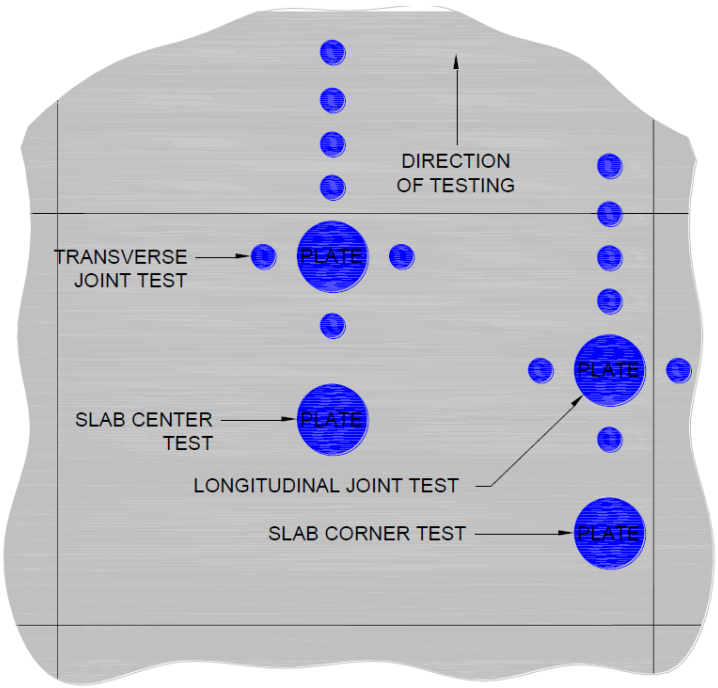

Figure 2.8: Location of Additional Sensors for Corner and Joint Testing with HWD (FAA AC 150_5370_11b)

Device	Type of Applied Force	Force Level	Force Measurement	Deflection Reference	Number of Measured Points	Maximum Daily Production
Benkelman Beam	Static	5,000 - 10,000 lbs	Dead Weight on Wheels	Elevation Datum	1	50 - 100 points
FWD	Broadband Dynamic	1,000 - 35,000 lbs	Load Cell	Inertial	Up to 9	100 -300 points

Table 2.2: Comparison between the FWD and the Benkelman Beam [4]

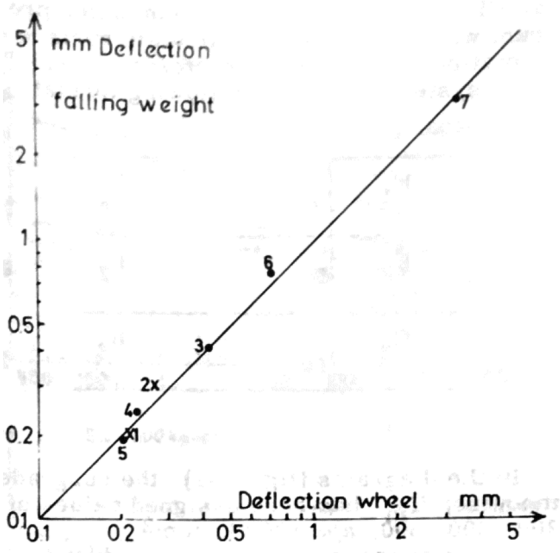

Figure 2.9: Correlation between the FWD and Moving wheel deflections [6]

Pavement Deflection Testing Devices that Move Continuously while Testing

1. **Road Surface Deflectometer (RSD)** The RSD was developed by the Council for Scientific and Industrial Research (CSIR) in South Africa and measures surface deflection under a loaded, moving wheel. The RSD is a modified Benkelman Beam that uses two reference feet at the stationary end for stability and one measuring point at the other end. For testing, the standard 18-kips (80 kN) axle load is used. A linear variable differential transformer (LVDT) is used in place of the dial gauge in the Benkelman Beam. The beam is 10-ft (3 m) long and thin enough to be located between the dual tires of the moving load. There is no study conducted on feasibility joint testing by RSD.

2. **LaCroix Deflectograph** The Lacroix Deflectograph was developed based on the deflection beam technology in 1957 [53]. Several versions of this device have been constructed [3] until the 'Flash' version [91]. The measurement is performed through automated Benkelman Beam tests under both rear dual wheels. A measurement cycle is divided into 3 steps. First, each beam is placed on the pavement surface. Second, the slope variations passing under the corresponding dual rear wheels are measured and third, the beam is taken away and repositioned in its initial position relative to the vehicle frame for the next measurement cycle. Measured slopes allow capturing the vertical displacements so that the influence line of the vertical displacement is obtained. However, the load moves at a slow walking speed and the measurements are not continuous and the length of the beam is not enough to establish a fixed reference for the deflection measurements. The device is shown in Fig. 2.10. There is no study conducted on feasibility joint testing by this device.

3. **Rolling Dynamic Deflectometer(RDD)** The Center for Transportation Research at The University of Texas at Austin developed a nondestructive tool for pavement deflection due to traffic loading. Cooperation between the US Air Force, the College of Engineering at the University of Texas at Austin, and Teledyne, Inc. funded the development and it used a modification of a Vibroseis truck that was

Figure 2.10: Lacroix Deflectograph

originally used for oil exploration [4]. The dynamic loading system of the Vibroseis truck was modified to a servo-hydraulic loading system, for the truck to apply dynamic forces while moving. The RDD demonstrated good potential for providing continuous profiles of flexible (and rigid) pavement structures. A comparison between RDD and FWD data showed a good correlation [4]. However, the RDD extracts only three deflection values compared with 7-9 for most currently-used FWDs. Additionally, the maximum operating speed of the RDD is 4.82 km/h, which makes the testing extremely time-consuming and inappropriate for operating on interstates and primary roads [2]. The device is shown in Fig. 2.11.

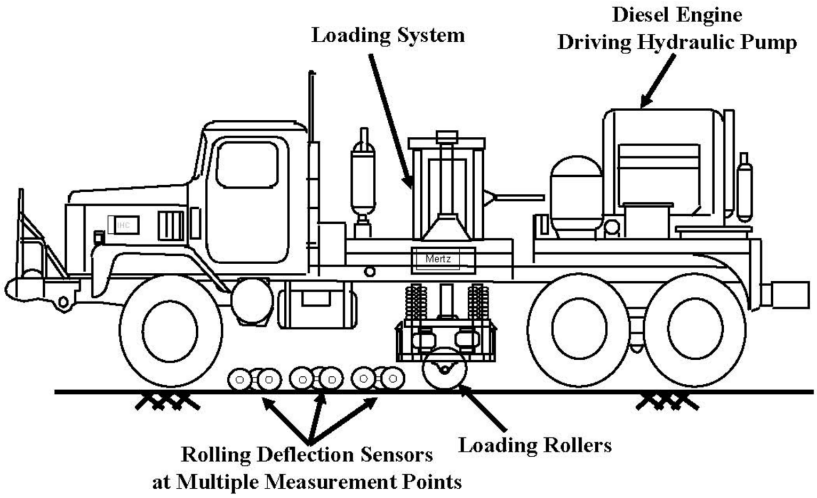

Figure 2.11: Schematic of a Rolling Dynamic Deflectometer

4. **Curviameter** This equipment was developed in 1977 [68]. Here the setup comprises of measurement geophones on a chain of 15 m. In contrast to the Lacroix deflectograph, only the right rear wheel is instrumented. The system is set up such that at each moment multiple geophones are touching the pavement and it remains at the same position on the pavement as the rear wheels roll over close to it while deforming the pavement. The curviameter measurements are not continuous, slow speed and restricted to flexible pavements. This device is shown in Fig. 2.12. There is no study conducted on feasibility joint testing by this device.

Figure 2.12: Curviameter (source BRRC)

5. **Traffic Speed Deflectometer (TSD)** This is a deflectograph with high travelling speed to overcome problems in traditional, stationary-pavement deflection measurement devices. The High-Speed Deflectograph (HSD) is based on Doppler technology, with two laser sensors to measure the deflection velocity of the pavement surface. The deflection is equal to the difference between the deflected shape and the undeflected pavement as the truck travels [40]. The trailer is capable of measuring pavement deflections at speeds up to 80 km/h. The pavement is loaded through a wheel load of around 4.989 kg, with sensors to maintain consistency in loading. Various calibration issues and the setup duration are the main challenges with the equipment making it unreliable [81]. In 2006, the name was changed from HSD to TSD, which then became commercially available. The current version of the TSD

has the potential to estimate the deflection velocity bowl, which enhances the accuracy of results. The device does not directly measure pavement or engineering properties as it measures the deflection velocity instead and calculates the deflection based on these measurements. The TSD is composed of a towing truck with a horizontal beam placed between the trailer axles, parallel to the direction of travel. Several equally spaced, measuring laser sensors are fixed on the beam. A secondary measuring system is used for adjusting positions of the sensors and their focus. The truckload is then transferred to the road surface through the tires while travelling at highway speed. The laser sensors direct laser rays to the pavement surface and thus measure the velocity in the direction of the rays. The laser pattern on the pavement is shown in Fig. 2.14. The Danish highway M30 was tested in 2001 by the high-speed deflectograph, at a 70-80 km/h travelling speed. The resulting data were compared with existing FWD data to determine testing reliability. Results showed that there was a significant deviation in the velocity measurements, compared to existing data from previous testing. An FWD and TSD comparison has been done using the limits of agreement method to compare the surface curvature index and the base damage index [49]. The device is shown in Fig. 2.13.

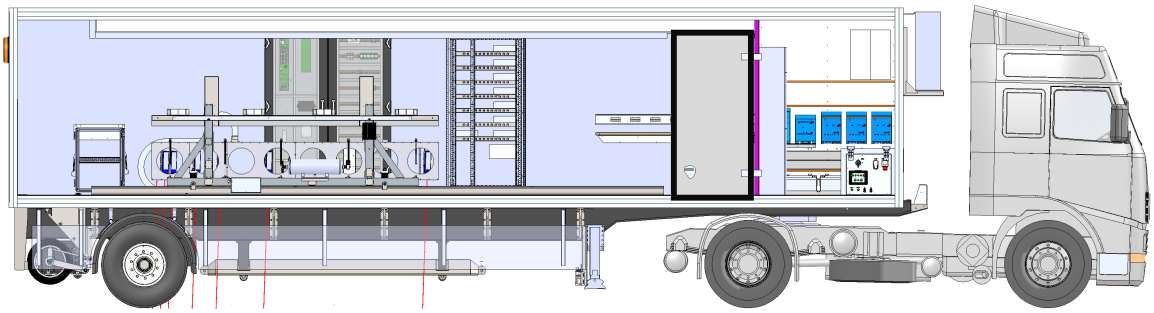

Figure 2.13: Schematic of a Greenwood TSD

6. **Rolling Wheel Deflectometer (RWD)**

This is a procedure for non-destructively evaluating and predicting the deflection response of various flexible pavements to loads imposed by different aircraft. Trans-

Figure 2.14: Detail of the sensors acquiring data close to the loading area, in the middle of a twin-wheel

fer function theory formed the basis of a pavement evaluation and response scheme. Two mobile systems were initially developed for the measurement of pavement deflections; the Light Emitting Diode (LED) system and the Linear Variable Differential Transformer (LVDT) system. It was concluded in [38], that the rapid non-destructive measurement of pavement deflections due to moving prototype loads was feasible and that a total non-destructive evaluation scheme based entirely on the use of prototype loads and measured deflections can be fabricated to evaluate and predict instantaneous response and cumulative effects of loads of various magnitudes and configurations. The next trial was done in 1983. Purdue University and the USAE waterways Experiment station developed a non-contact nondestructive deflection and profile measuring system using lasers. The guages were arranged so that their readings can be interpreted to provide the loaded and unloaded pavement profiles and a measure of its texture. Four guages were mounted on a rigid beam that in turn is mounted on the side of a loaded vehicle. The guages were located outside the range of influence of the load wheel. Hence the pavement below these gages was undeflected. One of the guages was adjacent to the load wheel to measure the induced deflection. An algorithm was developed that relates all the measurements to a common datum [11]. A feasibility study of a proposed method for measurement of highway pavement deflection under a moving load was presented in [84]. Non-contact displacement sensors measured pavement deflections at speeds

up 80 km/h. Anticipated problem areas with this measurement task were discussed and proposed solutions to them were presented along with equipment recommendations to implement the solutions. Test data was presented on an optical sensor of the type proposed for the measurement of pavement deflection. A recommendation was made to build a prototype pavement deflection measurement system based on the results of this work.

A prototype continuous deflection device [71], which they termed a Rolling Weight Deflectometer, has been developed as a nondestructive evaluation tool for airfield pavements. The system consists of a rigid trailer equipped with specially designed optical triangulation pavement sensors, a high-speed data acquisition system, and a high-pressure tire/load platform assembly. Pavement sensors are mounted on a rigid box beam equipped with an internal sensor system that corrects, in real-time, the relative pavement height position measurements for displacements induced in the beam by mechanical vibrations, changes in temperature, or non-uniform dynamic loads at points where the beam attaches to the frame. The device produces continuous deflection profiles that show pavement response to a moving loaded wheel along the path of travel. These deflection profiles, combined with multiple passes along a lane, provide a far more detailed picture of the pavement structural integrity than has ever before been possible because existing evaluation tools only produce response information at discrete points. Preliminary results show deflections measured by the device are in general agreement with the expected pavement response for various loads. A discussion of the device configuration, preliminary data, and potential as a pavement management tool is presented in [71].

A machine termed as 'rolling weight deflectometer' has been developed for directly measuring the deflection of airfield pavements under a rolling load wheel in [46]. It optically measures the maximum amplitude of the deflection basin using a new type of laser sensor. The bending-compensated measurements produce a deflection measurement with an accuracy of 40 μm (0.0015 inch). The deflectometer consists of a horizontally transported beam, strategically placed pavement sensors, a subsystem

that monitors beam bending, an odometer, and a data acquisition computer. The bending-compensated rolling weight deflectometer is a new method to rapidly and accurately assess pavement strength. Future improvements such as the speed of 13 m/s (30 mph) or more, pavement temperature coherent to deflection point, axle load and acceleration, ability to measure the shape of the deflection basin using additional pavement sensors, a higher-speed data acquisition network, and automatic power control of lasers in-pavement sensors have been suggested in [46] This device is shown in fig. 2.15.

Figure 2.15: The first rolling weight deflectometer trailer [46]

The deflectometer was patented in [47], that incorporates an alignment laser beam emitter that measures the vertical displacement of each of a plurality of distance sensors mounted on a horizontal sensor bearer member that bends or vibrates as it is transported over pavement for deflection measurement. The measured vertical displacements, due to member bending, allow the deflectometer to compensate for errors introduced by member bending and thereby provide a more accurate measurement of pavement deflection.

The modern device termed as Rolling Wheel Deflectometer(RWD) consists of a dual-wheel, single-axle semi-trailer equipped with four spot lasers mounted on an aluminium beam beneath the trailer[85]. Three lasers measure the unloaded pavement surface, and the fourth laser, placed near the centre of the dual tires, measures within the deflection basin under a 8164 kg single axle load. The RWD has been as-

sembled, and preliminary field runs have been made on thin and thick AC pavement sections. The RWD results have been compared to Falling Weight Deflectometer (FWD) and accelerometer-determined deflections on the same pavement sections and have produced encouraging results, although with some limitations. Several needed improvements have been identified. Plans for the RWD include system upgrade, further field testing over a wider variety of pavement types and conditions, demonstrations, including comparisons to instrumented test pavements, and eventually the manufacture of a production-level device[85] and is shown in fig. 2.16.

Figure 2.16: RWD developed by ARA and used in [85]

Measurements were used to assess the repeatability and characteristics of the RWD measurements, the effect of truck speeds, and the relationship between RWD deflection measurements and pavement conditions and is shown in table 2.3.

Development of a screening tool, referred to as the pavement-assessment triangular model, to predict overall pavement conditions based on RWD deflection, roughness measurements, and surface conditions as described by a pavement condition index (PCI) has been studied. Using the rolling wheel deflectometer (RWD), which measures pavement deflections at traffic speeds, offers the potential to characterize the structural capacity of the road network without major delays. The assessment tool is needed to incorporate RWD data into a current pavement management system (PMS) and to identify pavements in need of maintenance or rehabilitation [28].

In Table 2.4, a summary of existing structural assessment devices has been presented and it categorises these devices based on speed, discrete or continuous, static or dynamic and

Site identification	Test speed (km/h)						Average coefficient of variation (%)
	32		48	64	80	96	
	Average deflection	Coefficient of variation (%)	Coefficient of variation (%)				
1	0.41	16	17	14	13	—	15
2	0.4275	14	17	18	—	—	16
3	0.3125	13	12	13	—	—	13
4	0.39	6	8	9	—	—	8
5	0.2375	13	13	16	15	—	14
6	0.3725	6	7	8	9	—	7
7	0.1925	9	11	17	13	16	13
8	0.3975	18	22	19	20	—	20
9	0.2375	20	18	16	13	—	17
10	0.3875	14	17	16	—	—	16
11	0.4975	15	23	—	—	—	19
12	0.46	12	39	15	—	—	22
13	0.2375	18	18	16	20	—	18
14	0.3575	16	21	—	—	—	19
15	0.3375	14	14	16	15	—	15
16	0.5375	15	17	—	—	—	16

Table 2.3: Variability of Rolling Wheel Deflectometer Measurements in Research Sites at Various Testing Speeds [27]

the possible improvements for these devices. In Table 2.5, a comparison of continuous devices has been done based on manufacturers, estimated cost, operational speed, applied load, deflection accuracy and number of measurement points has been done. In Table 2.6, a one to one comparison of FWD and RWD has been done.

2.5.2 Technological development of continuous measurement devices

Among the different continuous deflection measuring devices, differences in technology lie in the ways in which the pavement responses are being measured. There are technologies based on the light phase difference method by using structured light to capture the deflection by employing the fringe projection method [63]. There have been attempts to experimentally define threshold levels relating vertical movements of the underlying joints and cracks by using the device known as the Rolling dynamic deflectometer. This device measures continuous deflection profiles by using a rolling geophone [15], [17]. Pavement simulations have shown that some parameters describing the deflection basin are more sensitive to pavement damage than the maximum deflection. To detect, locate and identify damages, the deflection basin has to be measured in a continuous way. A new

	Continue /Discrete	Max. speed [$m.s^{-1}$]	Max. load [kN/wheel or dual wheel]	Possible improvements
STBA Trailer	D		400	Operational weakness (Heavy + Time consuming tests)
Goodman	D			This device has been given up
SPA	D			Representativity of SASW tests?
STAC's Inclinometers	D	3-4	250	Speed to be increased because of creep phenomena.
Lacroix Deflectograph	D	8	65	Load to be adapted for airfield pavement. Speed to be increased because of creep phenomena.
Curviameter	D	18	65	Load to be adapted for airfield pavement
WES 16-kip	D		Static: 70 Dynamic: 70	This device has been given up (Operational weakness)
Road Rater	D		Static: 35 Dynamic: 35	Load and measurement system to be adapted to airfield pavements
Dynaflect	D		Static: 8 Dynamic: 4,5	Load and measurement system to be adapted to airfield pavements
F/HWD	D		300	
RDD	C	2,4	Static: 45 Dynamic: 22,5	Load to be adapted to airfield pavements. Speed to be increased because of creep phenomena.
RWD	C	105	80	Laser maybe not adapted to problem Problem of the reference to be solved.
ARWD v0	C	10	222	
ARWD v1	C	32	40	
RDT	C	97	70	
HSD/TSD	C	80	49	Load to be adapted for airfield pavement
SL	C			In early test phase

Table 2.4: General overview of existing pavement structural assessment devices [9]

Device	Rolling Dynamic Deflectometer (RDD)	Airfield Rolling Weight Deflectometer (ARWD)	Road Deflection Tester (RDT)	Traffic Speed Deflectometer (TSD)	Rolling Wheel Deflectometer (RWD)
Manufacturer	UT Austin	Dynatest Consulting and Quest Integrated	Swedish National Road Administration and VTI	Greenwood Engineering, Denmark	Applied Research Associates
Estimated Cost	N/A	N/A	N/A	$2,400,000	N/A
Operational Speed	3 mph	20 mph	60 mph	50 mph	20 to 60 mph
Applied Load	10 kips static + 5 kips dynamic	9 kips	8-14 kips	11 kips	18 kips (fixed)
Sampling Frequency	2-3 ft.	9 ft.	0.5 in.	0.8 in.	0.6 in.
Deflection Accuracy	0.05 mils	N/A	±10 mils	±4 mils/s	±2.5 mils
Number of Measurement Points	Up to 4	1	Up to 3	Up to 7	Up to 4
Comments	Very slow for network level testing	Unavailability of previous data	Unavailability of previous data	N/A	Appropriate for network level deflection testing

Table 2.5: Comparison of Continuous Deflection Testing Devices [26]

Factor	Rolling wheel deflectometer	Falling weight deflectometer
Operational speed	Traffic speed	Stationary
Deflection sensor accuracy	6.25 microns	0.254 microns
Number of operators	2	1
Productivity (km/day)	160–320	4–40
Number of sensors	1–2	7–9
Applied load (kN)	80	26–80
Load type	Transient wheel load	Impact circular plate
Backcalculation of layer moduli	Not possible	Possible

Table 2.6: Comparison of Operating Conditions for Rolling Wheel Deflectometer and Falling Weight Deflectometer [27]

measurement technology based on camera imaging detects the pattern from reflection of light projected on the pavement, allowing for a continuous measured deflection [80]. In order to measure continuous deflection by triangulation, an array of sensors can be used and this idea is not new. With the improvement of laser scanning technologies, it is now possible to measure surface deflection under moving load. At Dynatest, by means of patented system, which employs more than four sensors, the pavement deflection can be detected by using triangulation. Additional sensors compensate for the influence the measurements can have as the load-deflection basin is beyond those at the wheel load [88]. By extending a frame along the measuring surface in the direction of the rolling wheel and using the line scanning lasers mounted on this frame, several virtual images can be obtained. The images are matched to identify the corresponding regions to calculate the deflection value [57]. This idea has been used to develop the Rolling Wheel Deflectometer(RWD). To analyse the continuous monitoring by RWD, a finite element model for obtaining the response has been developed [59]. As the RWD is operating at traffic speeds, the load is moving with high speed and a formulation in a moving mesh is therefore more convenient. Therefore, a formulation of the Perfectly Matched Layer is developed in the moving frame of reference. Numerical results are presented in [58], for a single layer and a double layer half-space, respectively, subjected to a moving load of different velocities. To be able to properly interpret deflection measurements from an RWD device, more knowledge about the structural behaviour of a pavement when subjected to transient dynamic loads moving with different speeds is needed.

2.6 Evaluation of Load transfer by field measurements

Pure shear load transfer devices are shown to be particularly desirable under a combined externally applied and thermal loading condition since they offer no additional restraint to longitudinal curling [43]. Design guidelines are outlined for assessing the need for load transfer at transverse joints so that significant faulting is prevented [44].

The accuracy of the measurement technique of LTE was investigated in [77], as the results are important for maintenance decisions. It was found that LTE is a complex parameter

that depends on many factors that include load position, testing time, slab temperature, and load transfer device. Testing time and the season are found to have a significant effect on the measured LTE. THe greater the diameter of dowels, the more the variability of LTE measured. Joint openings changes daily and seasonally as the ambient temperature changes. As the number of joint opening increases due to slab contraction during winter, the measured load transfer efficiency generally decreases. Poor correlation was found between the deflection-based LTE and the percentage of the load transferred through the load transferring devices mounted across the transverse joint.

Similarities exist between the values of LTE(S) estimated from LTE(δ) measured by FWD [93]. Significant differences exist in the value of LTE(S) estimated from LTE(δ) and that directly measured under dynamic loading. Dowel joints exhibit uniform load transfer in two directions compared to a dummy or saw-cut joints. The study illustrates that the commonly used correlations between LTE(S) and LTE(δ) can be conveniently used in field evaluation of joint load transfer. However, the correlations are valid only for static loading.

In [100], a new approach to understand the real load transfer capability in airport and highway concrete pavements is presented, by not taking the assumptions followed earlier that the load is transferred under a wheel with zero speed and with fixed position, rather that the real load transfer commonly occurs with wheels under motion with non-zero speed. Dynamic effects are quantified comprising a moving wheel while it is crossing a joint on a pavement. The analysis is conducted using a model of a two-slab system on a Kelvin foundation. The peak value of the specified strains and deflections in unloaded slabs drops and its appearance time lags due to the presence of pavement damping. With the increase of the load moving speed v, the joint load transfer efficiency LTE(S) rises gradually. The larger the pavement damping, the bigger the variation of the peak strains, the longer the lag time, and the higher the LTE(S). The ratio (=LTE(S) dynamic/LTE(S) static) varies in the range of 1.0 to 2.0 mainly depending on speed and pavement damping. The influences of foundation reaction modulus and foundation damping on the joint load transfer efficiency are not significant, and therefore can be neglected.

The study results demonstrate how a non-destructive mechanistic evaluation procedure can quantify the key mechanics of a jointed PCC pavement site. These fundamental mechanistic responses are common to most design procedures and evaluation schemes. In this study, these fundamental mechanistic responses specifically were compared with the FAA airfield pavement design concept of the LT value. In the field, Load Transfer(LT) is continuously changing as a function of temperature and by joint type, age, and traffic [12].

2.6.1 Back-calculation

Using the principles of dimensional analysis, and leading to a closed-form back-calculation procedure for a two-layer slab-on-grade pavement system, the equations required have been derived in [42] and evaluated for four fundamental combinations of loading and support conditions. It is much more efficient and accurate than current approaches, allowing the use of any one of the measured sensor deflections in the back-calculation process. The concept proposed is powerful and versatile, and can easily be adapted for both rigid and flexible pavement systems.

In the development of a solution of surface deflections for the problem of infinite-slab-on-elastic foundation and its use in back-calculation analysis [78], numerical integration is employed to compute the surface deflections. The method adopted simplifies calculations and leads to the easy application in back-calculation of rigid-pavement parameters. The proposed closed-form back-calculation scheme presents a more general solution to the rigid-pavement-evaluation problem. The coded program can be used with deflections measured by any type of nondestructive surface deflection measuring device directly. A major advantage of this method is handling deflection data with measurement errors.

In a new procedure [79], for back-calculating the properties of concrete pavement with two slab layers using deflection measurements from nondestructive deflection testing, the two slab layers are first represented by an equivalent single slab layer based on the principle of equivalent flexural rigidity. In the back-calculation analysis, the pavement deflection response under load is evaluated using an analytical model for a slab supported on an

elastic foundation. Employing a closed-form back-calculation algorithm, it is shown that the back-calculated equivalent radius of relative stiffness and subgrade modulus is unique and independent of the characteristics of the two slab layers. It follows that the equivalent flexural rigidity for the two slab layers is also unique. The next step employs a trial-and-error algorithm to back-derive the moduli of the two slab layers by matching the equivalent flexural rigidity.

The development of a family of closed-form and semi-closed-form back-calculation algorithms for nondestructive evaluation of rigid pavement layer properties is presented in [31]. Using measured surface deflections as input, these closed-form algorithms were developed for a rigid pavement slab supported on a Winkler (i.e. liquid) foundation, an elastic solid foundation, and a two-layer elastic solid foundation. These closed-form algorithms were next employed to develop semi-closed-form algorithms for nondestructive evaluation of rigid pavements with two slab layers. The formulation of the algorithms and the corresponding methods of solution are presented. It is also highlighted that the closed-form algorithms can evaluate the quality of measured deflections and single out erroneous deflection sensor readings.

The results of a falling weight deflectometer (FWD) deflection analysis study performed as a part of a data analysis study under the Long-Term Pavement Performance (LTPP) program are given in [51]. Backcalculation procedures for rigid pavements adopted in this study and were performed using dense liquid (DL) and elastic solid (ES) subgrade models. Although back-calculated parameters determined in this study were found to be realistic for the majority of the LTPP rigid pavement sections, this study also uncovered some limitations of the current back-calculation procedures for rigid pavements. It was noted that back-calculated values may vary significantly due to factors such as the temperature at the time of testing, slab curling conditions, time of day, and time of year. Current rigid pavement back-calculation technology is inappropriate to adequately address all of these matters.

Computer algorithms and graphical solutions for deflection-based closed-form back-calculation of rigid pavement properties are available. However, a solution in the form of regression

equations would have useful practical applications because of the speed and convenience in computation. This work in [32] presents a regression model for this purpose based on the closed-form back-calculation algorithm NUS-BACK. The input parameters remain the same as the original closed-form algorithm, with no requirements for seed values or initial guess of pavement properties. The database for the development of the regression model was established by forwarding the computation of deflections for practical ranges of pavement properties. The verification of the regression model is presented by checking against the solutions of the closed-form algorithm NUS-BACK. The reliability of the regression equations was assessed against the closed-form algorithm for two conditions of input deflections: one for exact deflection measurements with no errors, another for deflection measurements with random errors. The analysis showed that the regression model could provide comparable reliability and accuracy to the analytical closed-form solution by NUS-BACK.

2.7 Summary

This review has identified a gap in the modelling requirement from the continuous evaluation perspective. The discussion has led to the choice of formulation that can be possibly implemented. Additionally, the continuous evaluation devices are still in an immature state and thus it is clear that experiments need to be set up to use these new measurement techniques to measure joint efficiency. It can be done by setting up such experiments and then using the forward analytical model to analyse such experimental data.

On the themes discussed above it can be concluded that the load transfer efficiency evaluation is an important design and maintenance parameter depending on the type of jointed pavement and application. There are several other distress types such as the cracking, voids, faulting, and loss of slab support which also contribute to the degradation of rigid pavements. This information has been known and non-destructive devices have helped to an extent to act as tools to evaluate rigid pavements. With the dawn of high frequency and more accurate continuous deflection testing devices such as the Dynatest ® *RAPTOR*, it is hoped that a faster and efficient evaluation of pavement can be achieved.

Category	Device name	Sensor type	Applied Load	No of sensors	No of data points per Km	Suitable for rigid pavements	Suitable for network level
Very slow-moving load and stationary sensors < 1 km/h	Benkelman Beam	Dial Gauge	80KN axle load	1	N/A	No	No
	RSD	LVDT	80KN axle load	1	N/A	No	No
Slow moving load and sensors<5km/h	LaCroix Deflectograph	Digital Guage	80KN axle load	2	N/A	No	No
	RDD	Geophone	45±20KN	3-4	2600	Yes(Partial)	Yes
	TPAD	Geophone	35±17KN	3	2600	No	
Moderately moving and stationary sensors <16km/h	Curviameter	Geophone	125KN axle load	3	320	Yes(Partial)	Yes
Fast moving load and sensors >60Km/h	TSD	Doppler Lasers	120KN axle load	4	Depends on user	Not studied	Yes
	Dynatest RWD	Line Lasers	50 KN wheel load	Up to 18	$2x10^5$ @60Km/h	*Subject of this thesis*	Yes

Table 2.7: Summary of Moving-Load Devices for Pavement Deflection Measurements

Rigid pavement is present on high-speed motorways and airports aprons. Varying in thickness according to application, load transfer devices are used according to the design of the pavements. These infrastructures need to be evaluated at low cost and high frequency without stopping the use of the pavements. Traditionally devices have been used for evaluation but that required the interruption of pavement use. Tackling this situation requires a high speed non-destructive continuous deflection measurement device for both structural and functional evaluation. Additionally, as more computing power is available at a low cost, intelligent and better efforts should be developed for a faster and more accurate assessment of the infrastructure.

This study aims to develop the knowledge required to understand continuous measurements. The latest laser-based deflection measuring devices are used to understand and set up experiments. The weight of the rolling system is limited to 5 tons for a single wheel and the laser is only accurate for measurements more than 10 microns, therefore the study is limited to joint evaluations. This should lead to a methodology to be used for rolling wheel deflectometer type measurements on rigid pavements for joint evaluations. In Table 2.7, a summary of moving load devices is presented and thus with this

literature review it is evident that no such study has been done concerning the evaluation of rigid pavement by a fast-moving rolling wheel deflectometer. This will allow a fast nondestructive evaluation of rigid pavements and save maintenance costs.

Chapter 3

Methodology

The final intention is to develop the research to analyse the continuously measured jointed pavement response to calculate joint efficiency. In the last chapter, it was concluded that there does not exist any implementation that is reasonable for predicting pavement deformation (deflection/response) in the vertical direction suitable for the research aim of this study. The methods that exist were found too slow for the intentions of this research. However, a model has been found in the literature that can help meet the aims of this research. This model is based on an analytical formulation. This formulation has been chosen to implement in this research. It has been selected for implementation because it solves a three-dimensional problem in an analytical context. It takes in parameters such as load transfer and other material parameters which could be calculated from the measurements. Additionally, being an analytical formulation, it would be flexible and computationally efficient when the task of inverse analysis comes up. One of the research aims is to continuously evaluate jointed plain concrete pavements, for which the prediction model should provide a deflection bowl in both directions in the slab plane. This deflection bowl should also contain the slabs forming the joint, which provides the load transfer. The chosen model for implementation will provide deflections considering these requirements.

Once the the model is implemented, the research aims to carry out its validation. Hence the vertical deflections from the analytical model across the jointed slabs are compared to a FEM based solution, which is deemed to be a standard numerical method. For con-

tinuous evaluation of jointed pavement the model implementation should to be validated experimentally and independently. Consequently, rigorous model validation is undertaken by comparing the model deflections to experimentally measured deflections.
Given the final purpose of the research, after the literature review, it is evident that continuous evaluation of jointed pavement with rolling wheel deflectometer technology has not been performed to the date. The RWD technology is not new but measurement devices built on this concept can be different as discussed in the literature review. For this research, the RWD technology measurement relies on a line-type distance laser sensor that was accessible for the study. It is the intention to use this sensor to continuously evaluate jointed pavement. After this experiments with a commercial RWD technology based device the Dynatest RAPTOR were planned.

3.1 Objectives

Given these research gaps in the context of the general aims of the research, it is important to specify the objectives.

- To implement a three-dimensional analytical forward model formulation to simulate the rigid pavement response close to the load and across joints.
- To validate the model numerically and experimentally.
- To apply this model to measure joint efficiency and back-calculate the pavement structural parameters, by developing experimental test setups and with a Rolling wheel deflectometer commercial device.

3.2 Methods

The selected model formulation involves a higher order differential equation and requires computer programs that can handle the system analytically to provide solutions. In previous research [13], only simpler formulations were solved numerically, because of what was possible computationally at the time. With increased computation power and by

using advanced mathematical software, nowadays it is possible to obtain solutions, which are expressed through variables of the problem, for example without having the exact numerical value of thickness of slab, a solution expression with thickness as a parameter can achieved. This helps to have a general solution which can be used to represent deflections. This result should provide a deflection solution for predicting jointed pavement deflections given the parameters are known. It is hence desired to solve the system in terms of the parameters, without putting in actual values of them. Additionally, in [13], several equations are wrong, and some of the complementary equations are missing, which causes additional challenges. The final step would be to write the correct programmed representation and program these in a way to arrive at the result. Thus, by leveraging the computationally correct implementation a solution would be made useable.

The next step is to execute the validation of the implementation, which is planned to be done by numerical and experimental means. The numerical validation is done by using a dedicated and peer-reviewed FEM code for simulating jointed pavement response called EVERFE [21]. A comparison of deflection bowls across the joints of the analytical model and the numerical method is planned. After this, research collaboration is planned to gather observational data from a database by collaborating with Service Technique de Aviation Civile (STAC) at Marne-la-Vallée, Paris. It is anticipated that the gathered data is a measured response from a deflectometer and the information about the section is known as it is a designed test section at their research facility. Thus, from this, it is hoped that experimental validation of model implementation will be accomplished.

The next step is to perform experiments. The first setup is prepared with geophones resting across the joints. Next, it is planned to construct a custom reference beam mounted with line laser sensors and continuous monitoring of joints is measured due to a rolling wheel load. It is hoped that by using the model the measured data could be utilized to calculate the joint efficiency. As a concluding step, an experiment with a commercial RWD device, the Dynatest RAPTOR, and a reference beam are both conducted simultaneously. With this experiment and by using the model it is expected to compute the joint efficiency. To measure joint efficiency, experimental tests are designed by employing industry-standard

non-destructive deflection measuring devices, such as the Falling Weight Deflectometer or Heavy Weight Deflectometer to collect field data. A test site for performing these measurements is chosen. The test site that is planned to be used is an abandoned, though well maintained military airport in Værløse, Denmark. To compute the joint efficiency by using the model, structural details of the pavement sections are required. To discover the construction details, inquiries are planned to Danish national archives as the field test site is part of the national heritage and protected. To conduct experiments that are simplified and mimic the model conditions for continuous evaluation, custom setup requires the usage of an information collection system.

This research is innovative because it will implement an analytical formulation that will be fast when it comes to estimating the joint efficiency. Subsequently, the process to calculate joint efficiency will require a solution to the inverse problem/ back-calculation. As is known, a back-calculation program requires several iterations of the forward model. Consequently, a fast implementation is crucial. The implemented forward model being analytical will be fast compared to the popular FEM and other mathematical methods. The additional innovation is that a rolling wheel load across the joint has not been looked into while being continuously measured to calculate joint efficiency. With this research, it is hoped to find methods to measure joint efficiency from a continuous evaluation point of view.

3.2.1 Hypothesis

A fast forward model is sought in the existing literature based on the applicable three-dimensional nature of the problem at hand rather than developing an ideal model from scratch. Thus, a simple two-layer model where the top layer is a jointed concrete slab resting on a two-parameter soil foundation is used throughout this study. The study assumes that the FWD and RWD devices for flexible pavement will work ideally on rigid pavement. It is hoped that these devices will work perfectly and the idea is to use these devices as a starting point to explore and understand the theoretical and technical feasibility for continuous assessment of rigid pavement. Beforehand it is known that the rigid

pavement has high modulus and thus will require higher loads to generate a measurable response but this should not prevent setting up simplified experimental test setups to measure, record and deduce analysable responses. Loads in these modern deflectometers can be varied and thus can be adjusted to meet the experimental needs.

3.2.2 Assumptions and limitations

It will be assumed that the physics of contact of two concrete slabs is simplified and microscopic behaviours at the joints and material aspects are not significant to the study and thus not discussed. The study focuses on the structural aspects of deformation of the slabs in the vertical direction i.e. parallel to the direction of load on the slabs. Additionally, extreme structural deformations leading to cracks and water pumping are not considered in the modelling.

A brief description of the terms and contextual hypothesis and assumptions will be presented. Then a description of the model formulation and the implementation will be described. The implementation of mathematical solutions and how they have been arrived at to get the solution will be presented. It is aimed that by using a mechanistic based accurate prediction of a jointed rigid pavement at the centre line of the edges of the discontinuity a reasonably accurate analysis of continuous measurements can be done.

To model the problem at hand, a mechanistic approach based formulation is selected. A model where pavement deflections can be predicted near the load and across the jointed pavement is ideal. However, physical and geometric aspects that need some context before modelling is presented next. Definitions of transfer efficiency among engineers and researchers can be different. These definitions are closely related and provide knowledge about the joints and are calculated differently. Sometimes the geometry of the slabs is not ideal, meaning they can be at an angle, so not perpendicular or rectangular. These considerations provide some context to a forward model and its applicability. However, it can be challenging to include geometries of dowels/slabs and other aspects sometimes. Subsequent chapters deal with the validation of the implementation of the model in this chapter and the experimentation to achieve the intended objectives of the research. To

keep the descriptions strictly relevant the next chapters have been separated into numerical and experimental validation of the model implementation respectively. In the experimentation chapter, all the preliminary experiments leading to the deflectometer experimentation have been presented.

Chapter 4

Modelling

Various modelling methods exist that can provide deflections. Methods such as empirical-mechanistic methods and mechanistic methods have been used in pavement engineering for decades. Such equations were developed from both experience and models. These models were used for back-calculation. Though accurate, these equations provide deflection values for fewer predefined positions of the load. Intending to predict vertical deflections at positions surrounding the load and the joint, based on a structural formulation as close as possible to a physical problem, a mechanical model simulating the jointed rigid pavement is set up.

The model implemented in this chapter is taken from [13]. Here a summary of the steps involved in the formulation is presented for consistency. To implement the mathematical model formulation, it was checked and details were incomplete. So in this chapter, all equations and mathematical formulations are given.

4.1 Boundary Value Problem

The boundary value problem here is **two jointed semi-infinite plates resting on a Pasternak foundation**, where the deflections are non-existent at infinity. The load is a pressure load and close to the discontinuity. To form a boundary value problem, constitutive equations, equilibrium equations, boundary conditions, continuity conditions and assumptions are required. These aspects are presented next.

4.2 Constitutive relations

Model formulation involves the inclusion of correct material behaviour. Material behaviour and the material model are usually linked and a model is arrived at once an assumed set of properties are fixed. An advanced model with detailed properties is more accurate as the behaviour predicted will be closer to reality. However realistic models tend to be complex to solve. It is reasonable to have a balance to avoid mathematical and computational complexity.

4.2.1 Slab

Slabs are made from concrete. Concrete material behaviour can vary but it follows the approximation of linear elasticity on a macro-continuum level. Given high moduli and toughness, usually the stresses and strains developed in the concrete for a given pressure load remain in the linear elastic zone before failure can happen. Slabs are made from concrete and if not reinforced, then it is an easy decision from the modelling point of view. In the research presented here, the stress-strain relationship in the linear elastic zone is the constitutive relationship. Thus, the relationship can be described as per linear elasticity, where σ_{ij} is the stress tensor and ϵ_{kl} is the strain tensor as

$$\sigma_{ij} = E_{ijkl}\epsilon_{kl} \forall (i,j,k,l) \in (x,y,z) \tag{4.1}$$

x, y, z are coordinates of the domain Ω of interest. E_{ijkl} is the material tensor relating stress and strain. Assuming, $\sigma_{zz} = \epsilon_{zz} = \epsilon_{xz} = \epsilon_{yz} = 0$, for plates and writing the strain as a function of displacement derivatives,

$$\epsilon_{i,j} = \frac{1}{2}(u_{i,j} + u_{j,i}) \tag{4.2}$$

$$\begin{aligned} \epsilon_{xx} &= \tfrac{1}{E}\left[\sigma_{xx} - \nu\left(\sigma_{yy} + \sigma_{zz}\right)\right] \\ \epsilon_{yy} &= \tfrac{1}{E}\left[\sigma_{yy} - \nu\left(\sigma_{xx} + \sigma_{zz}\right)\right] \\ \epsilon_{zz} &= \tfrac{1}{E}\left[\sigma_{zz} - \nu\left(\sigma_{xx} + \sigma_{yy}\right)\right] \end{aligned} \tag{4.3}$$

4.2.2 Sub-grade

The elastic modelling of the soil bed is based on an assumption for the behaviour of the subgrade reaction under loading. The most popular relation between forces and deformations is linear because of the simplicity of the equations' solution. The elastic subgrade reaction is represented by:

- One-, two- or three-parameter models;
- Continuum models;
- Mixed models.

Two-parameter models

Two-parameter soil models restore the continuity of the elastic foundation by introducing a second parameter. The two-parameter models of Filonenko-Borodich [29], Hetenyi [39] and Pasternak [69] provide the continuity of the soil medium by adding a second spring which interacts with the first one. In [50] Kerr generalizes the Pasternak model by including a third spring in a vertical direction. The models of Reissner [70] and Vlasov–Leontiev [92] make simplifying assumptions by introducing functions for distribution of the displacements or the stresses in the soil medium. The general expression for the strain energy in two parameter models is

$$U_{\mathrm{f}} = \int_0^{\ell} \frac{1}{2} k b w^2 \mathrm{d}x + \int_0^{\ell} \frac{1}{2} G b \left(\frac{\mathrm{d}w}{\mathrm{d}x} \right)^2 \mathrm{d}x \tag{4.4}$$

The second integral in Eq. 4.4 includes the second parameter G which represents the stiffness of a generalized rotation spring. Different interpretations exist of the physical meaning of G and the relation with the first parameter k : For the Pasternak model, the G parameter represents a shear modulus of a virtual layer that integrates the vertical spring elements. For the sub-grade or foundation modelling, a Pasternak foundation is chosen, where there is a shear layer or independent springs now have a shear connection between each of them, so they are not independent in the Pasternak foundation. Therefore, a Pasternak foundation is a two parameter foundation, where k is the Winkler spring

constant and the shear modulus is G.

4.3 Equilibrium equations

Consider a transversally loaded slab as given in figure 4.1. By postulating the hypothesis

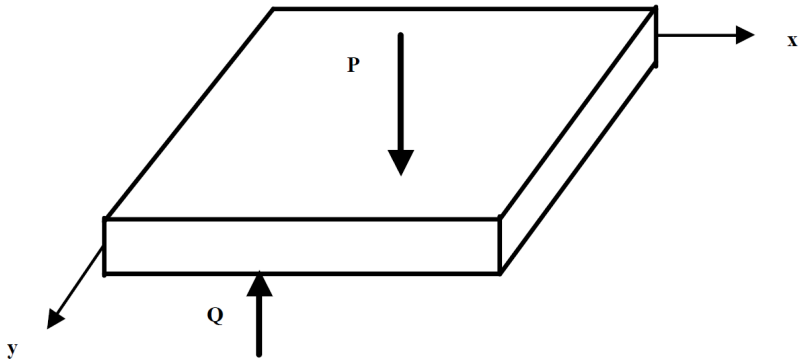

Figure 4.1: Equilibrium for bent plates

that the thickness of the slab can be considered thin against its other dimensions and that the deflections are small in comparison with the thickness, basic assumptions of the Theory of the Strength of Materials, allow the mid plane to be considered as a neutral plane wherein the horizontal displacements are zero.

Bending moment and shear forces

Consider a section of the slab parallel to the xz – plane, with a segment ab orthogonal to the neutral mid plane (Figure 4.2). w is the deflection in the z-direction. Again, one

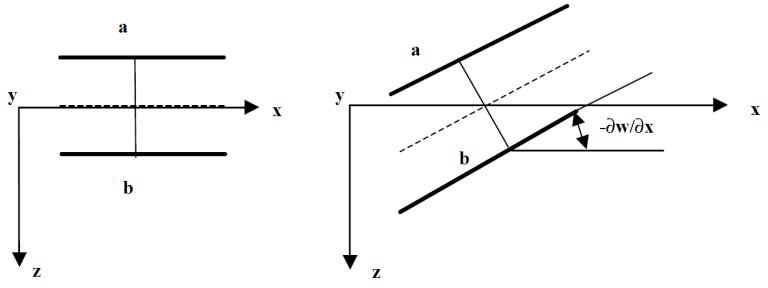

Figure 4.2: Bending moments and shear forces

may accept that the segment ab remains orthogonal to the neutral plane after bending. In the plane xz, segment ab will rotate over an angle equal to $\frac{\partial w}{\partial x}$ and in the plane yz, a

similar segment will rotate over an angle $-\frac{\partial w}{\partial y}$. If u is the displacement in the x-direction, one can write:

$$u = -z\frac{\partial w}{\partial x} \tag{4.5}$$

and if v is the displacement in the y-direction,

$$v = -z\frac{\partial w}{\partial y} \tag{4.6}$$

The strains can be deduced from the displacements

$$\begin{aligned} \varepsilon_x &= \tfrac{\partial u}{\partial x} = -z\tfrac{\partial^2 w}{\partial x^2} \\ \varepsilon_y &= \tfrac{\partial v}{\partial y} = -z\tfrac{\partial^2 w}{\partial y^2} \\ \gamma_{xy} &= \tfrac{\partial u}{\partial y} + \tfrac{\partial v}{\partial x} = -2z\tfrac{\partial^2 w}{\partial x \partial y} \end{aligned} \tag{4.7}$$

and the stresses by Hooke's law

$$\begin{aligned} \sigma_x &= -\tfrac{Ez}{1-\mu^2}\left(\tfrac{\partial^2 w}{\partial x^2} + \mu\tfrac{\partial^2 w}{\partial y^2}\right) \\ \sigma_y &= -\tfrac{Ez}{1-\mu^2}\left(\tfrac{\partial^2 w}{\partial y^2} + \mu\tfrac{\partial^2 w}{\partial x^2}\right) \\ \tau_{xy} &= -\tfrac{Ez}{1+\mu}\tfrac{\partial^2 w}{\partial x \partial y} \end{aligned} \tag{4.8}$$

The bending and torsion moments are obtained by integration of Eq. 4.8,

$$M_x = \int_{-h/2}^{h/2} z\sigma_x dz = -\frac{Eh^3}{12\left(1-\mu^2\right)}\left(\frac{\partial^2 w}{\partial x^2} + \mu\frac{\partial^2 w}{\partial y^2}\right) \tag{4.9}$$

and with D, the stiffness of the plate,

$$\begin{aligned} M_x &= \textstyle\int_{-h/2}^{h/2} z\sigma_x dz = -D\left(\tfrac{\partial^2 w}{\partial x^2} + \mu\tfrac{\partial^2 w}{\partial y^2}\right) \\ M_y &= \textstyle\int_{-h/2}^{h/2} z\sigma_y dz = -D\left(\tfrac{\partial^2 w}{\partial y^2} + \mu\tfrac{\partial^2 w}{\partial x^2}\right) \\ M_{xy} &= \textstyle\int_{-h/2}^{h/2} z\tau_{xy} dz = -D(1-\mu)\tfrac{\partial^2 w}{\partial x \partial y} \\ M_{yx} &= \textstyle\int_{-h/2}^{h/2} z\tau_{yx} dz = -M_{xy} = D(1-\mu)\tfrac{\partial^2 w}{\partial x \partial y} \end{aligned} \tag{4.10}$$

The moments can also be expressed as a function of the radii of curvature

$$M_x = D\left(\frac{1}{R_x} + \mu\frac{1}{R_y}\right) \quad M_y = D\left(\mu\frac{1}{R_x} + \frac{1}{R_y}\right) \tag{4.11}$$

Equilibrium

Consider an elementary parallelepiped of dimension dx, dy, h in Fig 4.3. Equilibrium of

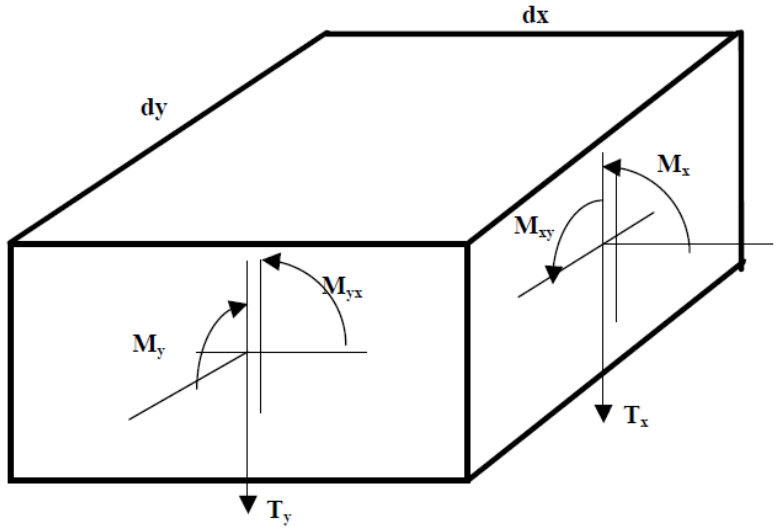

Figure 4.3: An elementary parallelepiped from a plate

the moments with regard to the x-axis.

$$\frac{\partial M_{xy}}{\partial x} - \frac{\partial M_y}{\partial y} + T_y = 0 \tag{4.12}$$

Equilibrium of the moments with regard to the y-axis.

$$-\frac{\partial M_{yx}}{\partial y} - \frac{\partial M_x}{\partial x} + T_x = 0 \tag{4.13}$$

Equilibrium of the vertical forces with regard to the z-axis

$$\frac{\partial T_x}{\partial x} + \frac{\partial T_y}{\partial y} + p - q = 0 \tag{4.14}$$

$$\begin{aligned} T_x &= -D\frac{\partial}{\partial x}\left(\frac{\partial^2 w}{\partial x^2}+\frac{\partial^2 w}{\partial y^2}\right) \\ T_y &= -D\frac{\partial}{\partial y}\left(\frac{\partial^2 w}{\partial x^2}+\frac{\partial^2 w}{\partial y^2}\right) \end{aligned} \tag{4.15}$$

Replacing the shear forces in Eq. 4.14 by their values in Eq. 4.15, one obtains the equilibrium or continuity equation for a thin slab subjected to pure bending

$$\frac{\partial^4 w}{\partial x^4}+2\frac{\partial^4 w}{\partial x^2 \partial y^2}+\frac{\partial^4 w}{\partial y^4}=\frac{p-q}{D} \tag{4.16}$$

After considering the force balance from the Pasternak foundation where the force varies with the square of the first displacement derivative, the following equilibrium equation can be arrived at

$$\frac{\partial^4 w}{\partial x^4}+2\frac{\partial^4 w}{\partial x^2 \partial y^2}+\frac{\partial^4 w}{\partial y^4}=\frac{p-q+G(\frac{\partial^2 w}{\partial x^2}+\frac{\partial^2 w}{\partial^2})}{D} \tag{4.17}$$

4.4 Physics at the joints and Joint conditions

The edge of a slab is joined to another slab, which can be interpreted as a plate's interactions against the other plate's edge interaction on a macro level. This jointed slab, modelled as two semi-indite plates next to each other is useful to obtain equations describing the behaviour due to a pressure load perpendicular to the centre-line. The center-line of the slab is the mean line. The equations for force and displacement are all formed around the mean line.

The physical behaviour of the edge to edge interaction would act as a continuous medium, if there was no edge or joint. But since s joint is a discontinuity in the domain, equations capturing the transfer of primary and secondary kinematic unknowns from loaded slab to unloaded slab need to be written to achieve a closed-form solution.

4.4.1 Deflection transfer

The deflection at the joint for the unloaded slab is assumed to be a fraction of the deflection at the edge of the loaded slab. This deflection ratio assumption is made given the load

position can be anywhere on the loaded slab. Deflection ratio is not constant for varying positions of the load, but the sensitivity is not too high compared to the other system parameters.

4.4.2 Moment

Under an ideal behaviour, the moment at the edge of the slabs is zero as it's an edge with no transfer of moments. Therefore in the formulation, the moments are equated to zero at the edge of the plate.

4.4.3 Shear balance

The shear forces are not zero at the edge. The shear forces are transferred from the loaded slab to the unloaded slab at the edge. This behaviour of transfer of shear under the effect of a pressure load on the loaded slab is used in a relationship by equating the shear forces at the joint.

4.4.4 Assumptions

This problem is assumed as a static case and the temperature effects on slabs material expansion or contraction given the temperature at the time of pressure load is not included in the development of the solution. In order to solve the system, a single jointed edge formed of two semi-infinite half plates is assumed. Here a summary of the assumptions for the system is listed.

1. Linear elastic framework
2. No thermal effects
3. A quasi-static problem
4. Small strains
5. Plain strain

6. Load transfer in y direction is constant

4.5 Fourier representations

A function $f(x)$ is represented in Figure 4.4. This function can be expressed as a Fourier

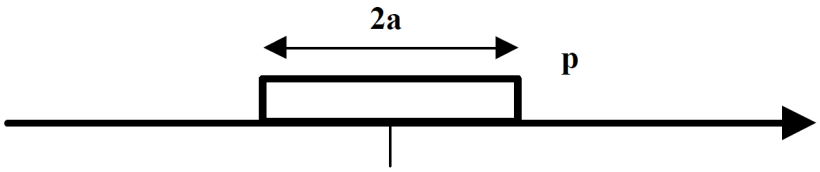

Figure 4.4: Example of a Fourier Integral

series

$$\begin{aligned} f(x) &= \int_0^\infty A(\alpha)\cos(\alpha x)d\alpha \\ A(\alpha) &= \tfrac{1}{\pi}\int_{-a}^{a} p\cos(\alpha u)du = \tfrac{2p\sin(\alpha a)}{\alpha\pi} \\ f(x) &= \tfrac{2p}{\pi}\int_0^\infty \tfrac{\cos(\alpha x)\sin(\alpha a)}{\alpha}d\alpha \end{aligned} \tag{4.18}$$

4.5.1 Load and deflection

The load is expressed as a double Fourier's integral by including the x and y direction,

$$p = \frac{4p}{\pi^2}\int_0^\infty\int_0^\infty \frac{\cos(xt/l)\sin(at/l)\cos(sy/l)\sin(sb/l)}{ts}dsdt \tag{4.19}$$

A similar equation should express the deflection for the system to provide a solution,

$$w = \int_0^\infty\int_0^\infty C(s,t)\frac{\cos(xt/l)\sin(at/l)\cos(ys/l)\sin(bs/l)}{ts}dsdt \tag{4.20}$$

4.6 Formulation

To predict the response of a jointed concrete pavement, a static 3D semi-analytical solution is developed. This forward model aims to be a sufficiently good approximation to real rigid pavements while being fast to calculate, e.g., in comparison with more numerically intensive approaches like finite element modelling. Figure 4.5 presents a schematic of the

model. The origin of the coordinate system is at the position of the load and x is the driving direction, y is the transverse direction and z is the vertical direction. The formulation is based on two semi-infinite jointed concrete slabs resting on a Pasternak foundation with subgrade reaction k and independent spring modulus G. The load transfer efficiency δ in Equation 4.21 is the ratio of the vertical deflection on the unloaded (w_{UL}) and loaded (w_L) slab right next to the joint at $x = c$.

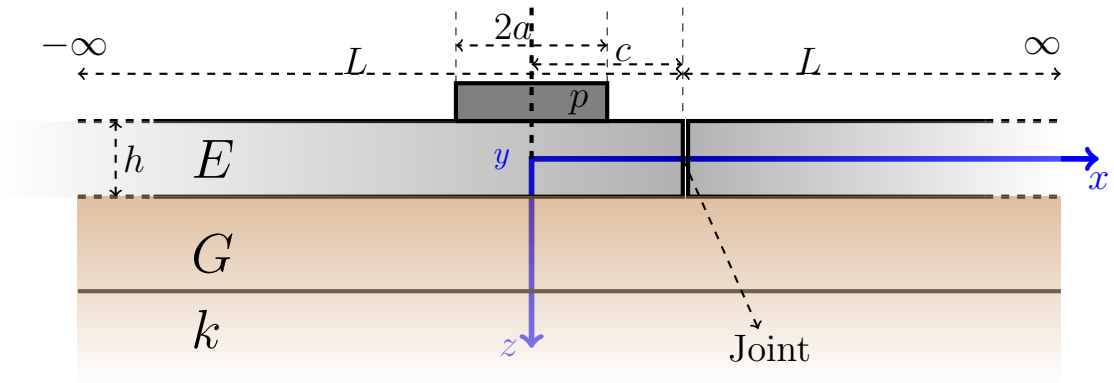

Figure 4.5: Coordinate system for the problem formulation

$$\delta = \frac{w_{UL}}{w_L} \tag{4.21}$$

This formulation has a vertical load of pressure p with a rectangular contact area $2a$ by $2b$ at a distance c from the joint. The slab is of thickness h with Young's Modulus E. The model is derived from the equilibrium equations describing the system. The boundary conditions imply zero vertical displacements at infinity in both x and y directions. The load pressure is assumed uniform and shear loads are not included in the model. The solution method is presented in [89], so the numerically challenging implementation is done here.

The equilibrium equation with independent variable, which is vertical deflection w, can be written as in Equation 4.22, where D is the flexural rigidity of the slab. The relation between the radius of relative stiffness l and the flexural rigidity is expressed in Equation 4.24.

$$\left(\frac{\partial^2}{\partial x^2}+\frac{\partial^2}{\partial y^2}\right)\left(\frac{\partial^2 w}{\partial x^2}+\frac{\partial^2 w}{\partial y^2}\right)-\frac{G}{D}\left(\frac{\partial^2 w}{\partial x^2}+\frac{\partial^2 w}{\partial y^2}\right)+\frac{kw}{D}=\frac{p}{D} \tag{4.22}$$

$$D=\frac{Eh^3}{12\left(1-v^2\right)} \tag{4.23}$$

$$\frac{G}{D}=\frac{2g}{l^2} \text{ and } \frac{k}{D}=\frac{1}{l^4} \tag{4.24}$$

To solve Equation 4.22, both the load and deflection are expressed as double Fourier integrals, which is shown in Equation 4.26 for deflection. The ratio of the deflections on either side of the joint is given by the definition of the load transfer efficiency in Equation 4.21. On each side of the joint, the solution is expressed as a linear combination of a particular solution w to the inhomogeneous equation as in Equation 4.25.

$$w_L=w+A(s)w_a+B(s)w_b; \quad w_{UL}=w+C(s)w_c+D(s)w_d \tag{4.25}$$

$$\begin{aligned} w=\frac{p}{\pi k}\frac{1}{\sqrt{1-g^2}}\int_0^\infty \frac{\cos(sy/l)\sin(sb/l)}{s\left(s^4+2gs^2+1\right)} \\ \Big\{e^{-(x-a)\alpha/l}\left[\sqrt{1-g^2}\cos[(x-a)\beta/l]+\left(s^2+g\right)\sin[(x-a)\beta/l]\right] \\ -e^{-(x+a)\alpha/l}\left[\sqrt{1-g^2}\cos[(x+a)\beta/l]+\left(s^2+g\right)\sin[(x+a)\beta/l]\right]\Big\}\,ds \end{aligned} \tag{4.26}$$

The two solutions to the homogeneous equation w_a and w_b for the loaded slab and w_c and w_d for unloaded slab are shown in Equation 4.27.

$$\begin{aligned} w_a &= \tfrac{p}{\pi k}\tfrac{1}{\sqrt{1-g^2}}\textstyle\int_0^\infty[\cos(\beta x/l)]e^{\alpha x/l}\frac{\cos(sy/l)\sin(sb/l)}{s}ds \\ w_b &= \tfrac{p}{\pi k}\tfrac{1}{\sqrt{1-g^2}}\textstyle\int_0^\infty[\sin(\beta x/l)]e^{\alpha x/l}\frac{\cos(sy/l)\sin(sb/l)}{s}ds \\ w_c &= \tfrac{p}{\pi k}\tfrac{1}{\sqrt{1-g^2}}\textstyle\int_0^\infty[\cos(\beta x/l)]e^{-\alpha x/l}\frac{\cos(sy/l)\sin(sb/l)}{s}ds \\ w_d &= \tfrac{p}{\pi k}\tfrac{1}{\sqrt{1-g^2}}\textstyle\int_0^\infty[\sin(\beta x/l)]e^{-\alpha x/l}\frac{\cos(sy/l)\sin(sb/l)}{s}ds \end{aligned} \tag{4.27}$$

Where two new auxiliary parameters have been introduced in Equation 4.28.

$$\begin{aligned}\alpha^2 &= \tfrac{1}{2}\left[\sqrt{\left(s^2+g\right)^2+1-g^2}+\left(s^2+g\right)\right]\\ \beta^2 &= \tfrac{1}{2}\left[\sqrt{\left(s^2+g\right)^2+1-g^2}-\left(s^2+g\right)\right]\end{aligned} \tag{4.28}$$

In the fourth-order partial differential equation, four conditions are required to couple the solution across the discontinuity at the joint. By relating deflections, forces and moments, Equations 4.29-4.32, can be written at the joint at $x = c$ in Figure 4.5. Equation 4.29 relates the deflections between unloaded and loaded slabs. Equation 4.30 and 4.31 are the cancellation of the moment at the edge of the loaded slab and unloaded slab respectively. Equation 4.32 is equality of the shear forces at the joint.

$$\delta\left(w + A(s)w_a + B(s)w_b\right) = w + C(s)w_c + D(s)w_d \tag{4.29}$$

$$\left(\frac{\partial^2}{\partial x^2} + v\frac{\partial^2}{\partial y^2}\right)\left(w + A(s)w_a + B(s)w_b\right) = 0 \tag{4.30}$$

$$\left(\frac{\partial^2}{\partial x^2} + v\frac{\partial^2}{\partial y^2}\right)\left(w + C(s)w_c + D(s)w_d\right) = 0 \tag{4.31}$$

$$\begin{aligned}&\left(\frac{\partial^3}{\partial x^3} + (2-v)\frac{\partial^3}{\partial x\partial y^2} - \frac{2g}{l^2}\right)\left(w + A(s)w_a + B(s)w_b\right)\\ =&\left(\frac{\partial^3}{\partial x^3} + (2-v)\frac{\partial^3}{\partial x\partial y^2} - \frac{2g}{l^2}\right)\left(w + C(s)w_c + D(s)w_d\right)\end{aligned} \tag{4.32}$$

4.7 Implementation of analytical solution

Solving these equations for constants $A(s)$, $B(s)$, $C(s)$ and $D(s)$ will lead to the solution of the problem. These solution expressions are very long, so their short form is presented is in Table 4.1 for different domains. As the system is a fourth order differential equation, the expressions in Table 4.1 are presented in Appendix A for the loaded slabs and in Appendix B for the unloaded slabs. In [89], the conditions and equations are presented but not solved. The idea is to have an analytical solution for all (x, y) near the joint when the joint is parallel to y axis.

By using powerful scientific tools such as Mathematica for analysing the equations and solving the system of these equations with the joint conditions allows an expression to be generated for all the constants $A(s)$, $B(s)$, $C(s)$ and $D(s)$. Once the constants generated it is possible to implement this solution by using these constants. In Table 4.1, the solution expressions for different positions of the whole domain are listed for one load position. To cover the whole domain, an additional set of equations w_b, w_b,w_b and w_b is required and expressed in Equations, 4.26, 4.33 and 4.34.

Table 4.1: Expressions for 3D deflection response

Position	**Bounds**	**Solution**
before the load on loaded slab	$-\infty < x < -a, \forall y$	$w_{bf}(x,y) + Aw_a(x,y) + Bw_b(x,y)$
under the load on the loaded slab	$-a < x < a, \forall y$	$w_u(x,y) + Aw_a(x,y) + Bw_b(x,y)$
after the load and before the joint on the loaded slab	$a < x < c, \forall y$	$w(x,y) + Aw_a(x,y) + Bw_b(x,y)$
fter the joint on the unloaded slab	$c < x < \infty, \forall y$	$w(x,y) + Cw_c(x,y) + Dw_d(x,y)$

$$
\begin{aligned}
w_u = \frac{p}{\pi k}\frac{1}{\sqrt{1-g^2}}\int_0^\infty \frac{\cos(sy/l)\sin(sb/l)}{s\left(s^4+2s^2g+1\right)} \\
\Big\{2 - e^{-(a-x)\alpha/l}\left[\sqrt{1-g^2}\cos[(a-x)\beta/l] + \left(s^2+g\right)\sin[(a-x)\beta/l]\right] \\
-e^{-(x+a)\alpha/l}\left[\sqrt{1-g^2}\cos[(x+a)\beta/l] + \left(s^2+g\right)\sin[(x+a)\beta/l]\right]\Big\}
\end{aligned} \tag{4.33}
$$

$$
\begin{aligned}
w_{bf} = \frac{p}{\pi k}\frac{1}{\sqrt{1-g^2}}\int_0^\infty \frac{\cos(sy/l)\sin(sb/l)}{s\left(s^4+2gs^2+1\right)} \\
\Big\{e^{(x+a)\alpha/l}\left[\sqrt{1-g^2}\cos[(x+a)\beta/l] - \left(s^2+g\right)\sin[(x+a)\beta/l]\right] \\
-e^{(x-a)\alpha/l}\left[\sqrt{1-g^2}\cos[(x-a)\beta/l] - \left(s^2+g\right)\sin[(x-a)\beta/l]\right]\Big\}\, ds
\end{aligned} \tag{4.34}
$$

Solutions are finally obtained by implementing as functions in MATLAB, such that all the parameters can be varied. The solutions of the differential equations are long expressions but fast to calculate. Now a forward semi-analytical model for two semi-infinite jointed slabs has finally been implemented. This model serves our purpose as the load positions are typically close to the load. This is especially true when using deflectometers using sensors/lasers aligned close to the loading plane. These constants are used in the original

expression to get the response. A typical response looks like in Figure 4.6.

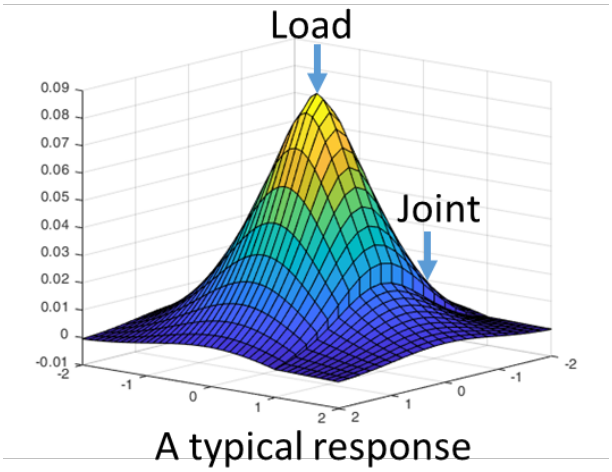

Figure 4.6: A typical 3D deflection response

4.7.1 Advantages

It is an apt model as it solves the problem with all the parameters as variables. It is fast as the solution has been generated analytically. The computation requires only one integration for one point in the domain. The load is a realistic pressure load. The foundation model is also advanced as it can tackle lean concrete below the slabs which acts as a shear layer over the soil. The solution seems to be sensible for distances up to l from the load position. The assumption that deflection ratio is constant for all load position does not matter as results from FEM solution from EverFE program show that it does not vary much.

4.8 Summary

A method to model the system has been established. A validation of this solution is required in order to establish its accuracy. This will help to understand its limitations and usages when applied for analysing experimental data. As per the objectives, in the next chapters, the method will be validated.

Chapter 5

Numerical Validation

For numerical validation, the aim is to find out whether the implemented analytical solution is satisfactory in comparison to the standard forward models. These models could be numerical models that exist and have been peer-critiqued. One of the open-source computer programs based on the Finite Element Method solution of jointed rigid pavement has been selected for comparison here.

5.1 FEM solution

The numerical FEM modelling technique, has been applied to the rigid pavement in an open-source program 'EverFE'. The program can be utilized to simulate pavement loads to calculate deflections, stresses and strains in slabs as shown in Fig. 5.2. For numerical validation, a comparison is required. Therefore, a set of parameters is first selected, then this set of the parameter is modelled by the FEM program and the 3D analytical model for comparison. Conclusions can be then arrived at.

5.1.1 EverFE program

EverFE is a 3D finite element program to simulate the response of jointed plain concrete pavement systems to loads of varying types such as axle loading, multi-axle loading and other effects. The program was developed up to the year 2004 and has an application-specific graphical user interface sequentially collecting all the inputs required for the

program to run shown in Fig. 5.1. The solution after all the input is displayed in Fig. 5.2. The results are available in separate text files as well.

Beginning with a series of developments [25] by using specific finite elements for modelling dowels for FEM, in [21] a 3D FEM program was developed. It allowed to model and solve the multiple slab configuration with different types of joints. Aggregate interlock was also included in this tool. To validate these developments, experimental verification of load transfer modelling was done and EverFE predicted the pavement response[23].

With [19], parametric studies were done to understand the effect of the foundation type and properties of the concrete slab's response. Likewise, joint load transfer's relationship to the foundation properties was explored. The use of an equivalent dense liquid foundation modulus in mechanistic rigid pavement analysis in the presence of stiff base layers is not advocated. With the use of a two-parameter subgrade model included in the previous chapter in the semi-analytical model, reassures the selection of the analytical formulation for this research.

With [24], load transfer using dowelled joints was examined using 3D finite element analysis along with two different types of foundation i.e. Asphalt-treated base and a dense liquid foundation. With [22], additional features modelling multiple slabs with dowel misalignment by accounting non-linear horizontal shear stress transfer between slabs and foundation were included. Additionally, computing advances for a fast solution of inverting matrices [20], such as a multigrid pre-conditioner for the unstructured non-linear problem were developed. With these sequential developments, this program offers an advanced and reliable prediction of response that can help design rigid pavements and predict their behaviour.

5.2 Analytical solution

Joint parameters for the analytical model and FEM program are different. The deflection ratio of the joints is not an input for the FEM program. But for an analytical solution, a ratio of deflection at the joint is needed as input. Hence, to calculate this value, the results are first arrived at by using a parameter set, then the deflections from the FEM

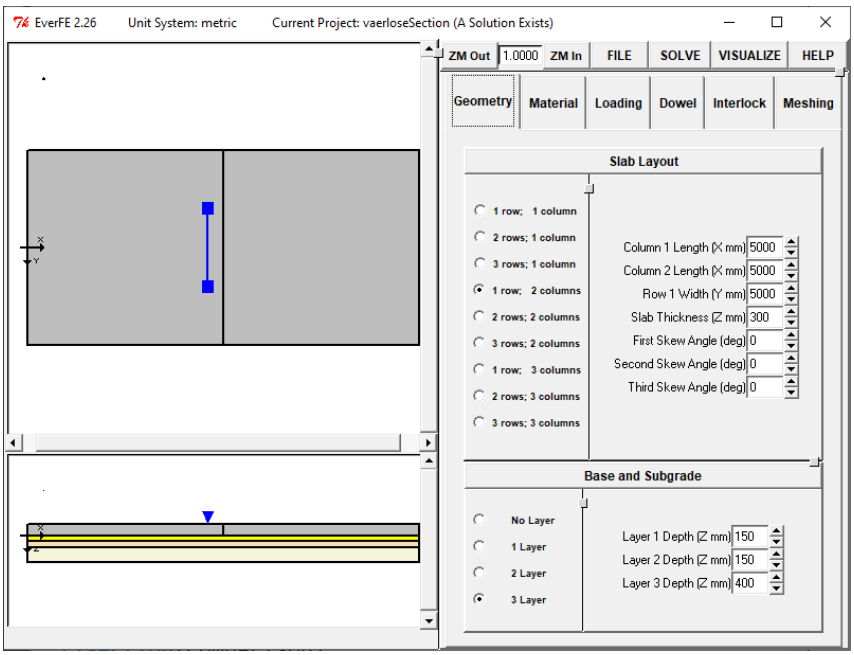

Figure 5.1: Finite Element based software EverFE

solution are used to compute the deflection ratio at the joint. This is then employed as an input in the analytical model for better comparability.

Two sets of comparisons were done. At first, different joint stiffness parameters were utilized in the FEM program to arrive at deflection ratios varying from 0 to 100. In this comparison, the remainder of the parameters were kept constant. In the second set, the joint stiffness was constant for FEM simulations, resulting in deflection ratios to being reasonably similar, and the other parameters were varied one by one, such as modulus of the slab, pressure load and so forth.

The parameters used for comparison in both sets is shown in Table 5.1. These parameters have been kept the same for the first set of comparisons while varying joint stiffness. For the second comparison one of these parameters was changed for both FEM and analytical models and those parameters are presented in comparison plots.

Table 5.1: Values of parameters for comparison

Young's Modulus	Load dimension	Winkler's constant	Distance from the joint	Thickness of the slab	Pressure Load
E[MPa]	axb[mm^2]	k[MPa/mm]	c [mm]	h [mm]	P [MPa]
30000,33000	100x100	0.05, 0.1	500, 1000	300	0.7, 1.4

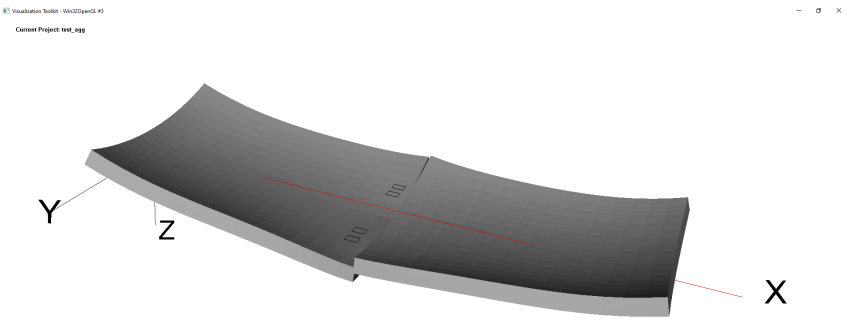

Figure 5.2: A vertical displacement solution in EverFE

5.3 Comparison

Here a comparison of the 3D-semi-analytical solution of semi-infinite jointed slabs to a FEM solution for the same set of material parameters, pressure loads and slab thickness is performed. The problem domain for the analytical model is $[-\infty, c] \cup [c, \infty]$ in the x direction and it continues infinitely in y and $-y$ directions. But for the FEM model, the slab size is fixed and taken as $5m$ x $5m$ joined with another slab of the same size. Therefore, in comparison results are shown for $10m$ (on the x axis) encompassing two slabs because the analytical model is accurate when the load position is not excessively far from the joints. The pressure load is vertical and positive in the z downward direction and the contact patch is of dimension $2aX2b$, where $2a$ is the total width in the x direction and $2b$ is the width in the y direction loaded symmetrically across the origin respectively. For the FEM program, the load patch also has rectangular dimensions. The subgrade parameter is the only Winkler parameter here for comparison even though the FEM program allows for multiple layers to be modelled, but for a comparison case, simplification of the foundation is used for consistency of outcomes.

The deflection of the pavement due to the deformation of the slabs in the vertical direction is discontinuous at the joints and is generated under the same pressure load applied over a rectangular area near to the joint at a distance c. This is one of the eight parameters required in the analytical model. The comparison of deflections is plotted across the

loading plane ($y = 0$) and is presented in Figure 5.3. It can be noticed that the response from both the techniques is similar, except under the load, for the different load transfer efficiencies. It is not similar under the load because of the numerical methods used to calculate the FEM solution. To further check these results, the value of deflection has also been verified by using Westergaard's solution for interior load and it matches the 3D-semi analytical response closer than the FEM solution under the load.

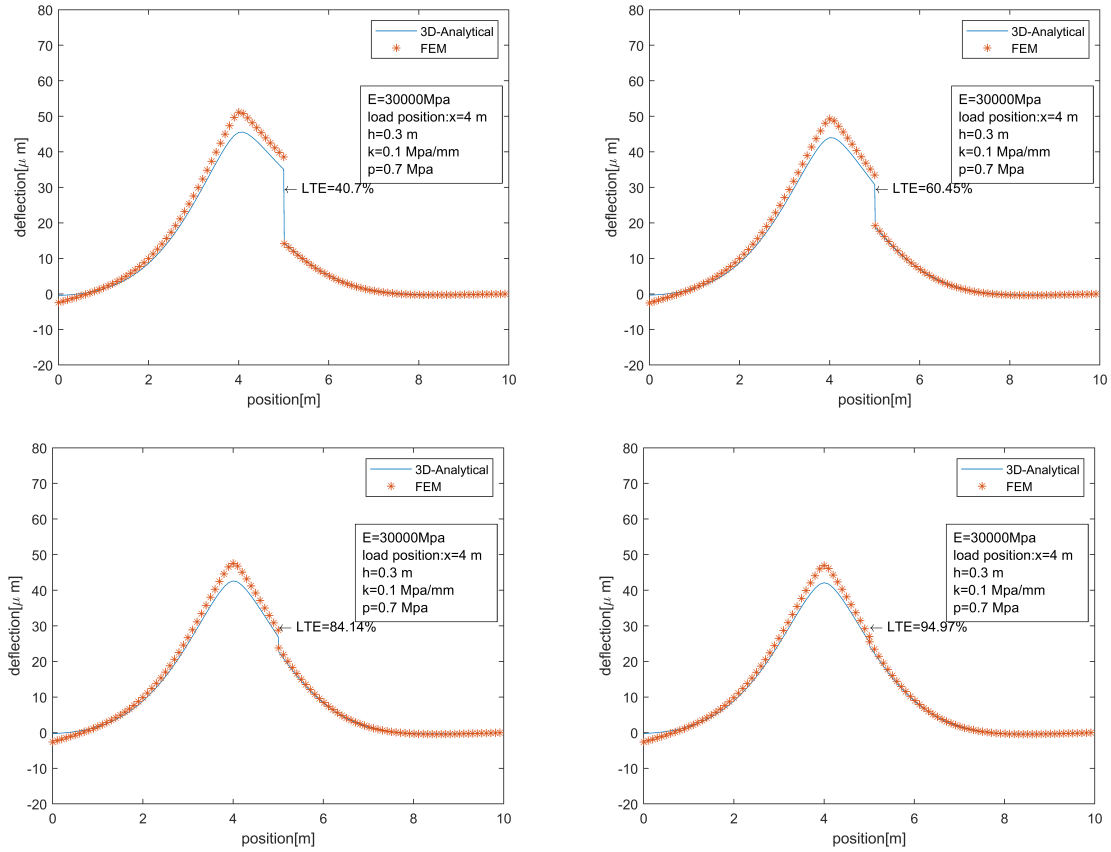

Figure 5.3: Analytical vs EverFE (Different LTE%, parameters fixed)

Further comparisons were performed by changing one parameter at a time in both the FEM program and 3D semi-analytical program. The results are presented in Fig. 5.4. The analytical model employs a set of parameters and reveals a good comparison to the FEM solution when one of these parameters is varied. In Fig. 5.4, parameters such as Modulus of slabs, Winkler subgrade, load and thickness of the slab are changed one by one. It means that the model is similar in terms of foundation and material aspects. This provides trust and versatility to the model. It can be used in back-calculation in appropriate settings.

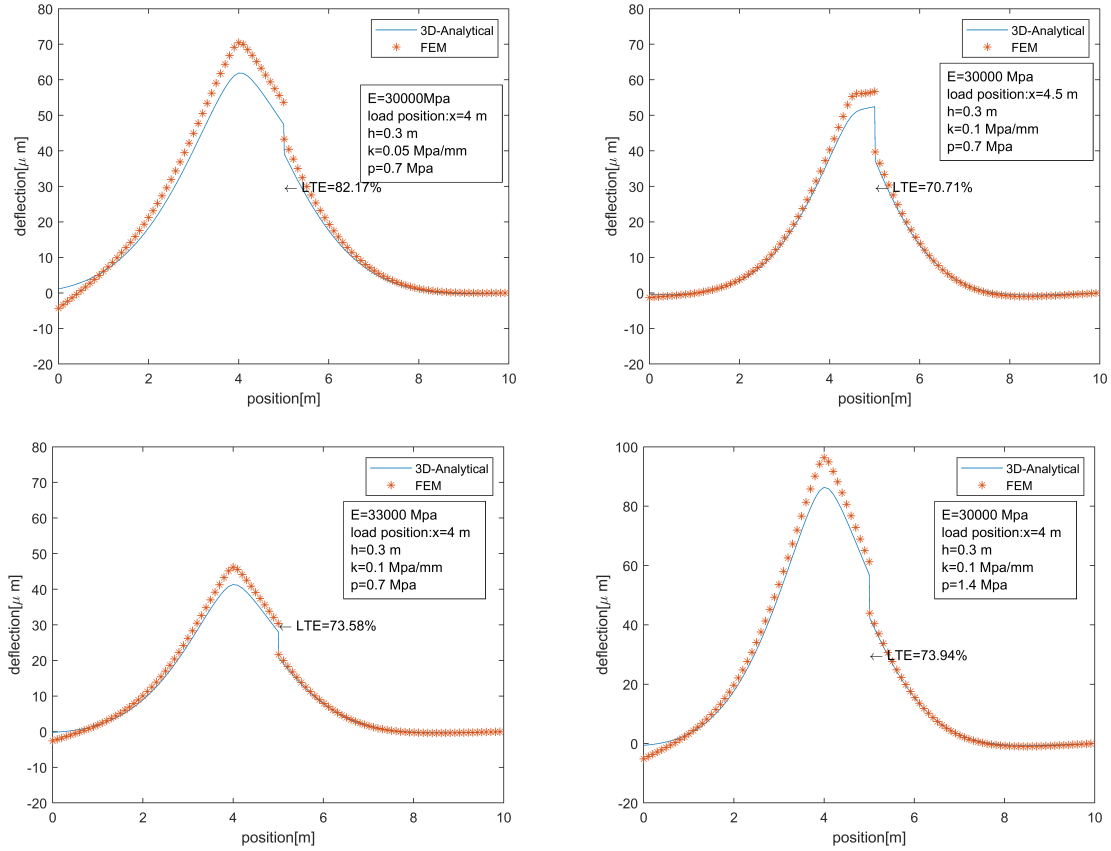

Figure 5.4: Comparison of 3D semi-analytical solution and FEM solution

It can be reasoned that the deflection response of slabs is close as the strong form of higher-order differential equation formed from the equilibrium equation that is solved in these models should be the same. As is well known, FEM solves the weak form of the equilibrium equation and with high mesh density both the solutions yield the same results. Therefore, the analytical model predicts/simulates deflections in the same manner as the FEM solution does except under the load. The explanation is that under the load, the FEM discretization of the domain influences the solution, whereas, in the analytic solution, there is no discretization of the domain.

5.4 Summary

The development of this model has been done for several reasons. FEM is slow and cannot be utilized for continuous evaluation in a network-level back-calculation. It is unsuitable for optimization purposes where there is a need to compare the measured

and predicted data from the model. The analytical model allows for faster calculation time as it is computationally inexpensive. Another benefit from this model is that the deflection response can be made available at any predetermined point, whereas for FEM calculations, the problem is solved for all positions (all Gaussian points of finite elements) in the domain, even if the usage needs response at just one position, for example at the position of measurements. Additionally, model parameters such as slab dimensions, cross-section of the pavement with details of subgrade layers need to be known for FEM calculations. But for an analytical model, no such details are required for slabs; only one geometrical parameter, the distance of the load position to the joint, is needed. Parameters such as the slab size and cross-section layers and their dimensions are not needed.

This first validation against a peer-reviewed open-source software EverFE is very encouraging. But the validation of the model also requires experimental validation. Though in, turn it can be argued that the FEM program has been validated experimentally, as mentioned in literature review. But in this chapter the comparison is done via a single soil foundation parameter, which may not be realistic. Therefore, experimental validation is presented in the succeeding chapter. After which, the next steps would be a comparison of the experimental data from the nondestructive deflection testing devices such as the FWD, simplified laser beam experiments and then RWD. This will give further understanding of the model, the challenges involved in the back-calculation can be understood, and the strategies to tackle these challenges can be projected.

Chapter 6

Experimental Validation

In the previous chapter, the first component of the second research objective was achieved. The second component of the research objective is to validate the analytical model implementation experimentally. In this chapter, an independent experimental validation is presented where the steps of setting up experiments and gathering data from measurements have been done independently.

A research collaboration with the Direction Generale d'Aviation Civile (STAC), Bonneuil-sur-Marne, France, was carried out with the broader set of objectives to explore the utilization of the analytical model for joint efficiency. From the database at STAC, the deflection measurements from an experiment that was conducted as a part of their study using a Heavy weight deflectometer (HWD) on instrumented rigid pavements have been utilized here for this validation. Measurements across a joint, when the load is near to an edge of the slab, were conducted. Deflection values were measured at positions of geophones.

6.1 Test site - STAC

In Fig. 6.1, a panoramic view of the instrumented rigid pavement facility at STAC is shown. Out of all the slabs, that can be seen in Fig. 6.1, a particular set of rigid pavements has been instrumented. The details of instrumentation are available in [10], where the slab can be measured along diagonals and across the edges for vertical and horizontal

Figure 6.1: Panoramic view of Instrumented Rigid pavement test site at STAC

movements at a depth inside the slab. Extensometers are used to instrument the rigid pavement. The deflection data from an experiment was gathered from the measurement database at STAC. The experiment was performed on instrumented rigid slabs. Its layout in top view is shown in Fig. 6.2 and 6.3. As shown in these schematics, the experiment

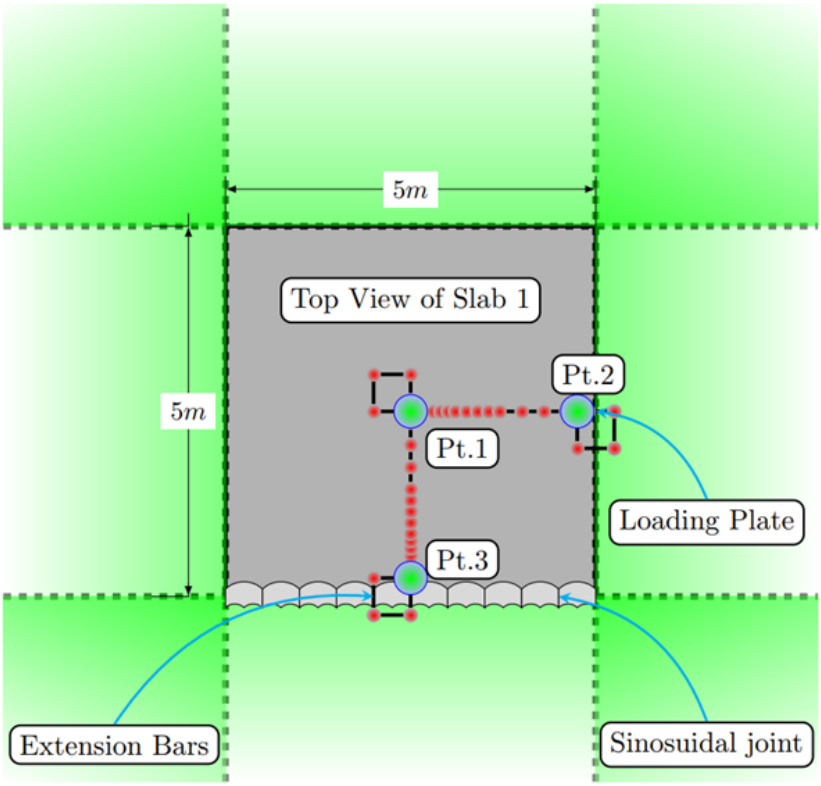

Figure 6.2: The schematic of the measurement setup - Slab 1

was performed with three HWD drops with two sets of different loads for position Pt.1, Pt.2 and Pt.3 on slab 1 and Pt.9, Pt.10 and Pt. 11 on slab 2, respectively. Only those points near the edge were selected as the aim is to validate the model's response across

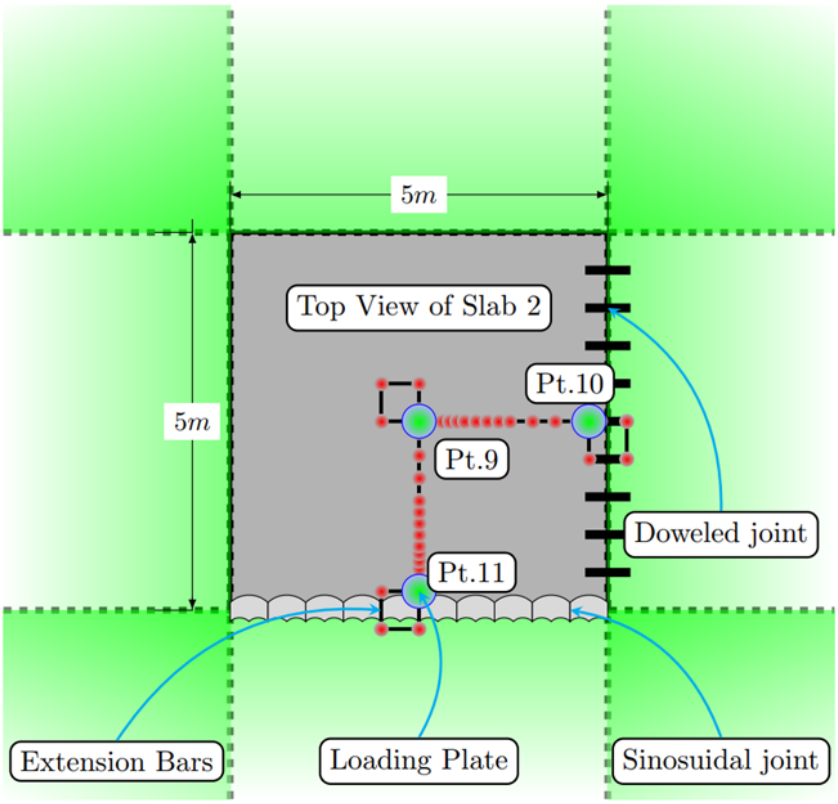

Figure 6.3: The schematic of the measurement setup - Slab 2

the joints in this chapter. These points come from two slabs, which are structurally different at their edges. The slabs are jointed to neighbouring slabs by straight, dowelled and sinusoidal joint mechanisms. These jointed edges of the slabs were loaded by HWD with a custom additional arrangement of geophones. These geophones were mounted on a customized extension bar. The dimensions of the extension bar are 48 *cm* X 50 *cm* which is a rectangular frame attached to the main frame and mounts additional geophones. This special arrangement provides data out of the plane of load and geophone and is used to do corner and load transfer testing. These details have been labelled in Fig. 6.2 and Fig. 6.3. The manufacturer of the HWD used to conduct measurements was **SWECO-Primax**. Comparative results from a test carried out at STAC in 2016 is presented in [10]. The experimental observations of deflections are shown in Fig. 6.4, for three loading cases. For back-calculation purposes, the FEM model was developed at STAC for their study, to account for the dynamic nature of the impact loads from an HWD. This FEM model simulated all the different positions of loads. The results are shown in Fig. 6.5. It can be observed that the FEM model models corner deflections better than other cases. For other

loading cases, FEM deflections and experimental measurement comparisons are further compared to the corner case of loading. The main aim of their study was focused on the slab centre deflections but not edge deflections. However, the deflection measurements were available for all the cases including the edge-loading case. This data is useful for the experimental validation of the analytical model and is used for comparison in this chapter.

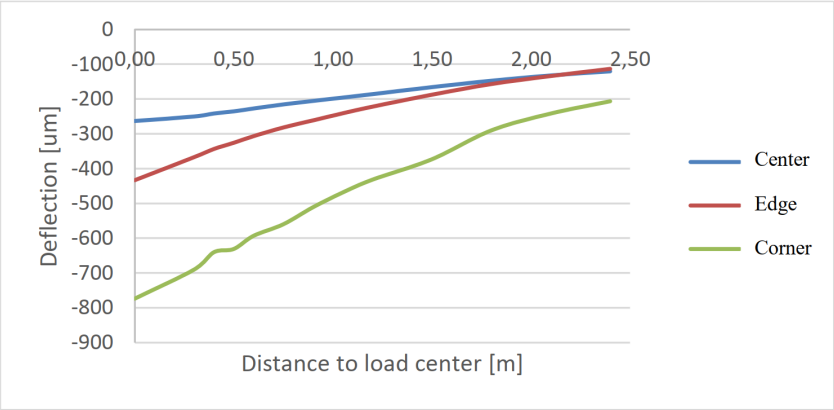

Figure 6.4: Measured peak deflections (y-axis) for corner, edge and center loading from the research in [10]

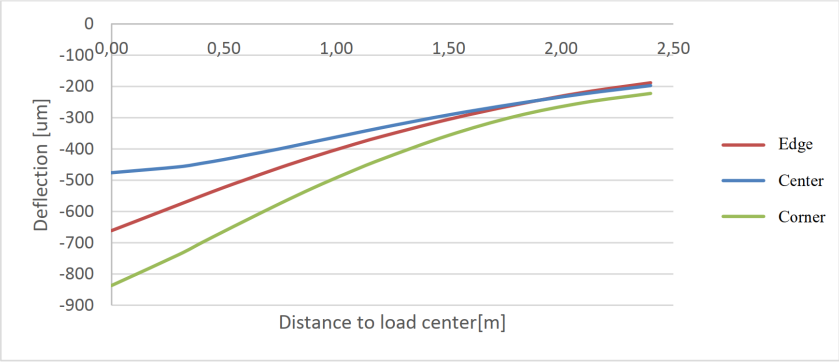

Figure 6.5: Calculated peak deflections (y-axis) for corner, edge and center loading from the research in [10]

6.2 Comparison of measurements to the Analytical model

To do a comparison by using the same set as the experimental data vs the 3D analytical model, correct model parameters are required to predict the deflections. Material and structural parameters were provided from the STAC instrumented test database. Among all the parameters that were required for the model, foundation details, the value of subgrade reaction k and subgrade shear modulus G, are unknown. These values need to be calculated. For this purpose, the FEM model [10] calculates stress under the load and the deflections at the bottom of the slab. This was possible by the research collaboration as their FEM solution provided results for all the elements through the cross-section geometries and at any depth. Thus, deflection and stress obtained from the FEM solution is used to calculate the k value. Now, these structural parameters and the loading conditions are used in the model.

S.No	Parameter	Value
1	Youngs Modulus of Slabs (E)	30000 MPa
2	Thickness of the slabs (h)	0.3 m
3	Load plate area (a)	0.1590 m^2
4	HWD load (F)	148 kN, 296 kN
5	Subgrade Reaction (k)	0.035 MPa/mm

Table 6.1: List of Model Parameters and their values used for comparison

Accounting for the fact that foundation and subgrade thicknesses are slightly different, a contribution of this factor needs to be taken into account for better validation. The cross-section of rigid pavements in the French design method has lean concrete below the slabs, which acts as an elastic foundation. In Fig. 6.6 the cross-section of the rigid pavement at the experimental site is shown in detail. To adjust for the lean concrete layer, in the 3D analytical model, which models a two-parameter Pasternak foundation, the analytical model can take account of the elastic foundation by tuning the shear parameter. It is important to carefully use the two parameter effect shown in Fig. 6.7(b) as opposed to the Winkler foundation shown in Fig. 6.7(a). Thus, the value of G, which is the shear

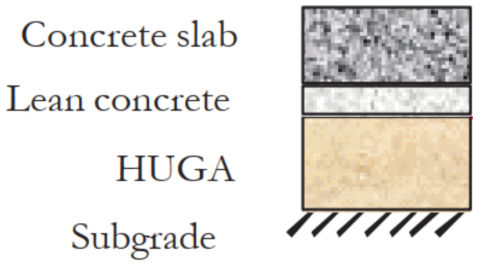

Figure 6.6: Cross-section of a rigid pavement test section by French Design method (HUGA- Humidified Untreated Graded Aggregate)

value for each independent Winkler spring is the parameter that is optimized to arrive at the deflections. Keeping these points in mind, the comparisons of vertical deflection are

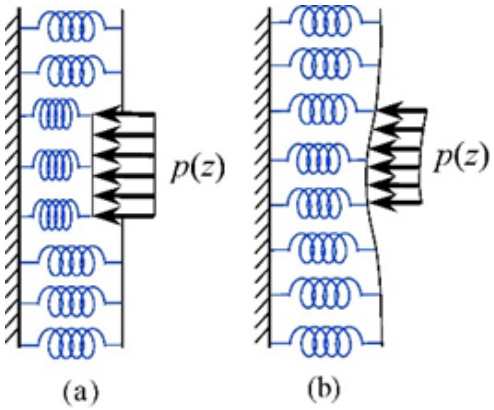

Figure 6.7: The two-parameter Pasternak Foundation

arrived at and shown in Fig. 6.8.

In these comparisons, two sets of plots are presented. On the left in Fig. 6.8 is the straight edge as a joint in slab 1. In this plot, the experimental observations are circle dots. There are two sets of measurement data with two different loads, one of which is exactly double the other. But the values of measured deflection are not exactly double, so in essence non-linear behaviour of the slab is observable. Since the 3D analytical model is linear the model predicts exactly half deflection values for comparison. Here the higher load value is chosen to be compared with the experiment. To arrive at the comparison, the parameter values that have been used are shown in Table 6.1. These parameters are obtained from the database. A similar comparison is done for the plot on the right in Fig. 6.8, which includes a sinusoidal jointed edge.

Similarly, for slab 2, the results are shown in Fig. 6.9. The difference to note here is

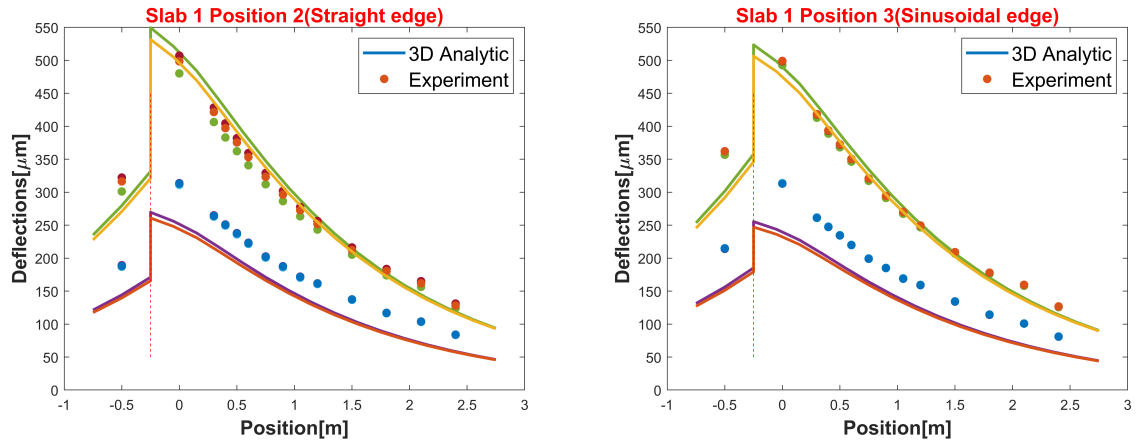

Figure 6.8: Experimental vs. 3D analytical Model deflections for Slab 1

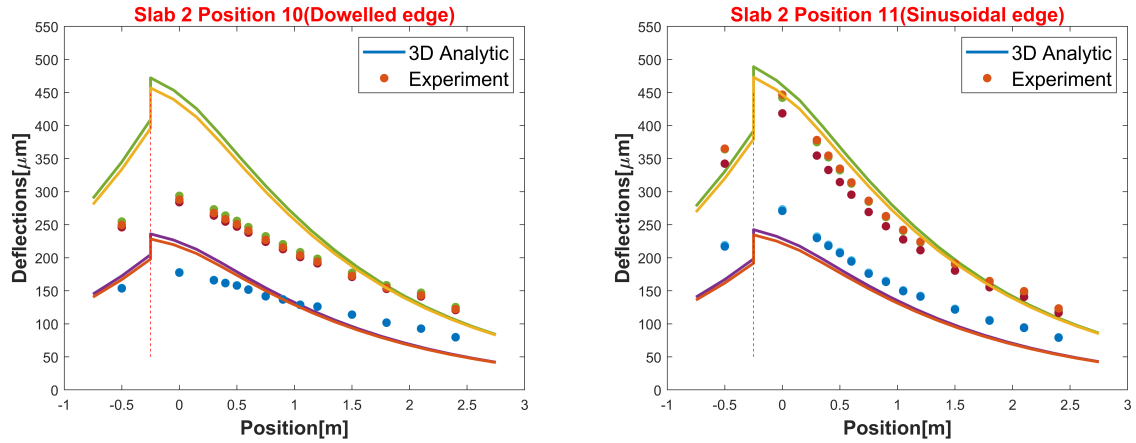

Figure 6.9: Experimental vs. 3D analytical Model deflections for Slab 2

that the comparison of the model vs. experiment for the dowelled edge is poor. In the analytical model, the dowels' physical behaviour leading to transfer of moments is not included. It is observed that the dowel reduces the curling effect at the edge and acts as a better load transfer mechanism. Note that the load transfer efficiency parameter in the comparison is calculated from the two closest points on each side of the joint which are 25 cm distant from the joint. But in the model's formulation, the load transfer efficiency is defined by the points on both sides of the edge at almost zero distance. This difference in the comparison can be further resolved to arrive at even better model and experiment comparisons by using interpolation of the experimental data to the edge positions.

Comparing this to the study [10] at STAC for the edge loading, it is evident that the 3D analytical model can predict deflections more precisely and accurately for the edge case. Therefore, it can be concluded that the model is reliable. With the mechanical model

ready, the second objective of the research on continuous deflections of rigid pavement is achieved. This model can be applied to calculate joint efficiency based on deflections. That will then suggest the condition of joints. With the trust in the model to predict/simulate vertical deflections, a set of experiments needs to be designed to test different load types and placement of measurement sensors for continuous evaluation.

6.3 Summary

This chapter ends with a reasonable justification of the analytical models implementation's experimental validation. It establishes its ability to predict the deflections. It shows that joints relying on aggregate interlock can be predicted better compared to dowelled joints in the case of jointed plain concrete pavements. Having this experimental validation has built some level of confidence in its ability to be used for the measurement data analysis that will be exercised in the latter part of this research. Even though the loading experiments are not static but dynamic, while the intention is to be used for moving loads which are not dynamic but more static, this should not lessen the merits of the model. As in the previous chapter, numerical validation was performed comparing the outcomes to a FEM program that has been experimentally verified in the days of its development. This FEM software is the FAA software and not the STAC FEM (For back-calculation purposes, an FEM model was developed at STAC for their study in [10]). The second objective of the research has been achieved with experimental validation.

Going forward in the next chapter, steps are taken toward the third objective of this research. Consequently, experiments are performed to analyse the measurements outside the 'load plane'. 'Load plane' means that a plane that is passing through the centre of load patch/contact area and is coplanar with the direction of gravity and parallel to the longer part of the beam that mounts geophone or lasers. Hence, from the beginning of this research, an emphasis on exploring a 3D model has been the motivation to measure outside of the load plane. It has been the case because, in case of continuous evaluation, it is challenging to measure under the rolling wheel where it meets the pavement. Additionally, sensors cannot be placed on the wheel plane, but are offset from this plane. Therefore,

in the next chapter, a series of experiments with geophones outside of the load plane, a custom reference beam setup mounted with laser sensors, and then finally a test with the RWD are presented.

Chapter 7

Experimentation

The motivation for this study has been the continuous evaluation of rigid pavement, where the focus has been set around the joint efficiency measurements. Generally in continuous evaluation, the sensors are at an offset from the 'load plane' with current technology. For this reason studies investigating joint efficiency with loads at on offset from the load plane, should be conducted. Therefore, the next step is to set up test experiments where the load is outside of the sensor/geophone/gocator plane across joints.

In the previous chapter validation was based on dynamic FWD loads; therefore, to begin with, the first step is to set up a customized FWD test. A customized FWD test means that, the beam that mounts the geophones will be taken off the FWD trailer and put on the ground across the joint. This beam will be resting on the ground as opposed to the normal FWD tests where the beam lifts off from ground after each drop. The aim is to simulate a continuous moving load. Additionally, the beam is outside of the plane of the load plate of the FWD. With these changes, FWD loads and the geophone configurations will be similar to an RWD geometrical setting, where the geophone frame is outside of the impulsive loading plane and the measurements are collected at the positions where the line lasers are placed on the measuring beam in an RWD. This test will provide an insight into possible joint efficiency measurement with FWD and a comparison to the prediction model.

Additional standard experiments where the deflection joint efficiency is measured will also be conducted. These standard experiments will serve in comparison to customized

experiments and to the model as it requires LTE as an input. By knowing LTE incorrect interpretation from customized experiments is avoided and insight into setting up correct analysis of custom measurements will be developed. This will also help to reveal the changes required in additional experiments that will be presented in this chapter, thus developing the research.

This chapter starts with a brief introduction of the measurement site and its history. Followed by the customized FWD tests, reference beam experiments and finally a reference beam with RWD experiment.

7.1 Measurement site- Værløse Flyvstation

Figure 7.1: Apron area selected at Værløse Flyvstation

The runways at Værløse were built in 1934 to start operations the same year, and then in 1953, the first concrete runway was established to fulfil NATO requirements. It was 2450 meters in length and 45 meters wide. The strength was designed to withstand the load of the heaviest NATO aircraft at that time. In 1981 an enlargement was made to a length of 2800 meters and width to 50 meters. At the same time all taxiways and the large parking platform 'apron' in front of the 2 hangars, north of the runway, were established with the

same strength as the runway.

In the beginning, the strength of runways was measured as per Load Classification Number (LCN), later changed to Pavement Classification Number (PCN). All aircraft have a ACN number, so the pilot looking at the airfield data-sheet can see if he can land at a specific place. The reason for using concrete at military airbases is the fact that aircraft using afterburners melt an asphalt surface.

Before the airbase finally closed in 2006, it was checked if the surface could take sizeable airliners in connection with VIP visits from the USA. All aircraft were accepted. When finally closing, it was investigated if all the concrete could be removed to bring things back to nature. It appeared to be an unrealistic task due to costs, getting rid of tons of concrete, and the fact that many pipelines for drinking water supply are located underground.

The apron area at the Værløse flyvstation is at the north the runway and is highlighted with a box in Fig.7.1. The apron area is situated next to hangars and parked military aircraft when it was in operation; it is shown in Fig.7.2. At the ground level, it appears as in Fig. 7.3. In this figure, the jointed plain concrete slabs, which have not been under operation for the last 15 years, can be observed.

Figure 7.2: Satellite view of Apron area at Værløse Flyvstation (The blue line is the row of slabs, which has been used for testing in this research)

By courtesy of the Danish Ministry of Defence's Property Agency (Forsvarsministeriets Ejendomsstyrelse), the technical design details of the apron area with the cross-section details of the thickness of layers were obtained. The top view of the apron is shown in

Figure 7.3: Ground view of Apron area Værløse Flyvstation

Fig.7.4. The cross-section details are shown in Fig.7.5.

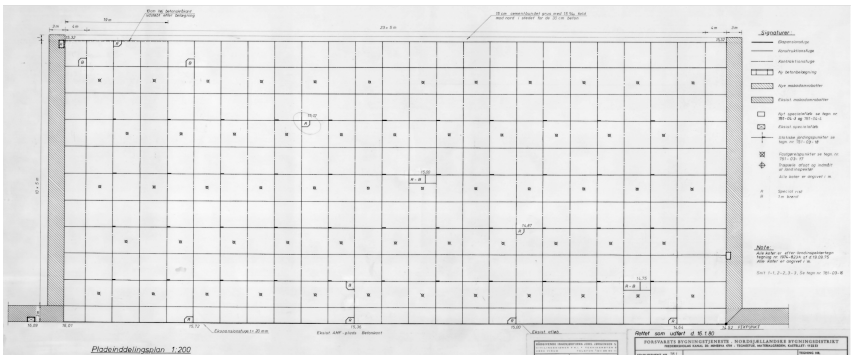

Figure 7.4: Technical drawing of the Apron pavement construction (Obtained via Forsvarsministeriets Ejendomsstyrelse)

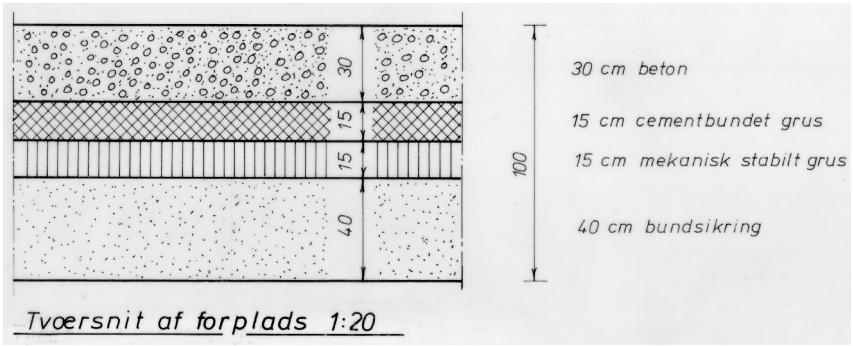

Figure 7.5: Technical drawing of the pavement cross section details(Obtained via Forsvarsministeriets Ejendomsstyrelse)

By using these details, a more accurate forward modelling of the test site and thus better experimentation was planned and is presented in the proceeding sections in this chapter.

7.2 FWD - offset load and geophone experiment

The experimentation was carried out with a customized FWD setup. This experiment was set up to test the viability of the idea of measuring the deflections out of the plane of the dropped weight, to begin with. Then the model was used to compare measured deflections and joint efficiency. Continuous measuring devices measure response outside of the load plane because, in such technologies, sensors are close to the moving load, not exactly below the loaded wheel.

7.2.1 Objective

The aims of this experiment are as follows:

1. Understand the separation of the load plane and measurement plane
2. To model and observe impulse load response and joint efficiency with a static model
3. To understand the non-linearity of concrete pavement response

7.2.2 Test setup

The test is carried out in two sub parts. The first is a standard LTE measurement using extension bars. The second is the customized FWD test.
For the first part, to measure LTE, a rear extension bar is used, which is attached to the geophone-holding frame. It is shown in Fig. 7.6. As concrete slabs can bear high loads so, to have a significant response from the joints and measure load transfer, dropped weights and drop height are increased by changing load configurations on the FWD. This test is conducted for the same joints where the second part of this experiment will be done to set up the baseline LTE measurement.
A schematic of the setup for the second part of the experiment is shown in Fig. 7.7, where the grey circle represents the FWD load plate and the small red circle represents the geophone positions. The top view of this test setup is shown. The distance of offset and the relative positions of the geophones from the joint are labelled.

Figure 7.6: Standard FWD Load transfer measurement test using geophones mounted on rear extension bars

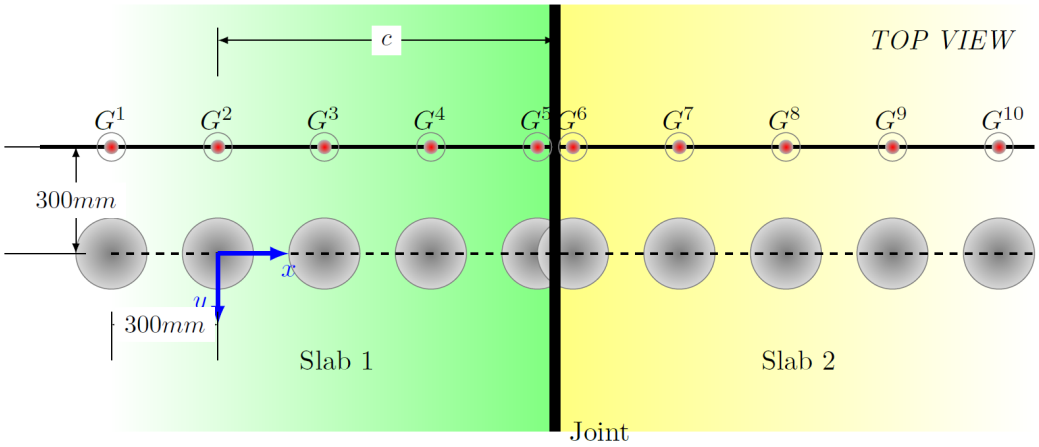

Figure 7.7: FWD load plate drop positions relative to the Geophones (G^i)

To implement the offset of geophones, the mounting frame was required to be removed from the FWD frame. Then, all the wired connections from geophones to the data collection system were required to be extended. All the individual geophone mounting brackets were repositioned to the distances marked in Fig. 7.7. After these changes, a custom script in the data collection program saved the measured data with this custom test setup. On the test site, the offset distance was marked and for each load drop, the vehicle with FWD frame was moved carefully to prevent breaking and tearing of the wires. The setup is shown in Fig. 7.8.

In situ measurements required attention to the cable and wiring for all the geophones. Since the load drop generated pavement vibrations, a weight was placed on top of the frame to avoid errors and noise in the geophone measurements. After the setup was

Figure 7.8: Placement of the frame with Geophones across the joint

finalized, 10 FWD load drops for all positions corresponding to G^1 to G^{10} were measured. Using this setup and implementing it at the test site, an FWD load plate drop for a point G^6 is shown in Fig. 7.9. The distance between G^5 and G^6 is 100 mm compared to the standard 300 mm to have the FWD load plate on both sides of the joint. In Fig. 7.9, it can be seen that load is on both the slabs.

Measurements

At first, the rear extension standard load transfer test was performed. The first set of measurements shows the load transfer values of the sites in Fig. 7.10. The drops were conducted by a set of different weights and are labelled. It can be seen that the load transfer values (LTE) are different for each dropped weight category. Thus, it shows that the deflection based LTE measurements are sensitive to load and especially to impulse load. There is an increase in load transfer of 20% when the load is doubled. Two drops for two different weights are done to confirm the repeatability and linearity of the measurements. These deflection-based load transfer values will guide in the model comparisons against measurements from the offset load test.

After the standard load transfer test, the offset load test was performed and the results

Figure 7.9: FWD load plate drop during the experiment next to Geophones

from this test are shown in Fig. 7.11. In this plot, all the deflection values measured by the geophones placed in front of the load have been shown for 10 drops at a single test site. The vertical blue line indicates the position of the joint. It can be observed that the behaviours on the two sides of the joint are not symmetrical even though the properties of the slabs are identical. They do not provide the same response. It can be inferred that due to differences in subgrade and non-linearity of the structure, such asymmetric behaviour is observed.

7.2.3 Results

After these measurements, all the measured deflections from these tests will be compared to the model. To do a comparison, first, a set of parameters needs to be known. From the measurement data, the parameters such as load and distance to the joint are known. The measured load transfer is known from the first part of the experiment. The rest of the parameters are assumed. Once these parameter values are decided, the model can generate the field of deflections and then a comparison is made. The results are shown in Fig. 7.12.

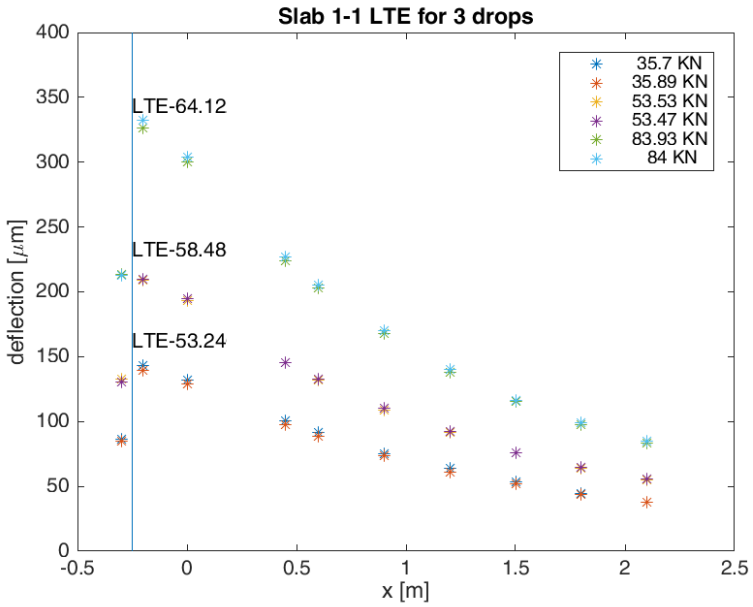

Figure 7.10: Measured Deflections by FWD Rear extension for Load transfer efficiency (LTE)

Such a comparison is possible with a 3D model because it is possible to simulate deflections outside of the load plane. Moreover, it was mentioned earlier that points G^5 and G^6 are $100mm$ apart, thus the load plate being $300mm$ in diameter there is an overlap of the load over the joints. A load placed next to G^5 will load both slabs simultaneously. So, by a superposition of two cases as the analytical model is linear a prediction can be calculated and is shown in Fig. 7.12 at the center. Parameters used are $E = 38000MPa$, $h = 260mm$, $k = 0.05MPamm$ and $LTE = 0.98$.

This comparison is then extended to all the Geophones G^1 to G^{10}. Data for all the 10 drops for different load positions are shown. For these positions, the model can also generate a field of deflections on both sides of the joint, therefore a comparison of all the drops is done and is shown in Fig. 7.13. Each peak on the y axis for one curve in this comparison corresponds to the position of the load on the x axis. For these 10 positions G^1 to G^{10} , 10 deflection curves for measurements and the other 10 from the model are shown. In Fig. 7.13, the distance of the fit at the farther positions of the drops is not as good as near the joint at $x = 0m$, for the same set of parameters for all drops. The parameters used are $E = 34000MPa$, $h = 260mm$, $k = 0.04MPamm$ and $LTE = 0.9$.

To understand the quality of the comparison for farther positions of the load from the

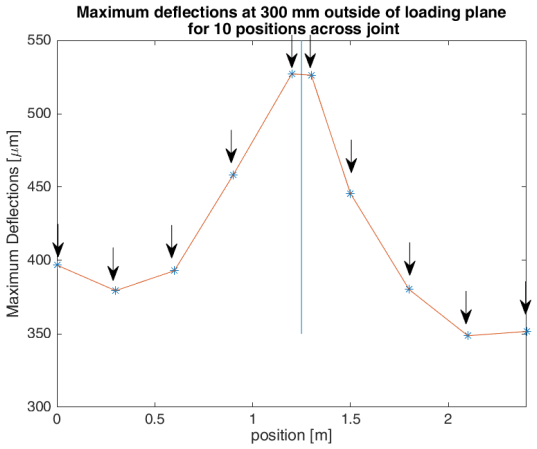

Figure 7.11: Center deflections for all ten drops

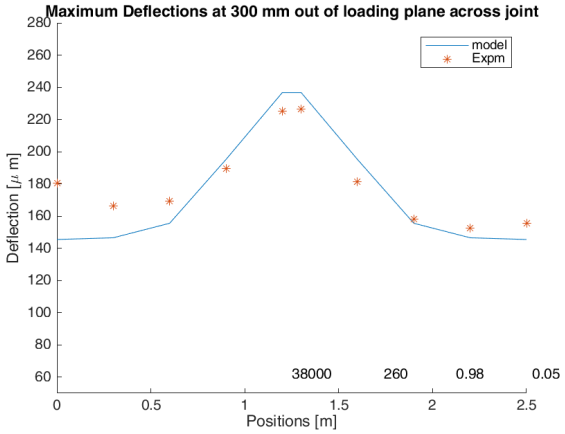

Figure 7.12: Fitting of modelled and the experimentally measured centre deflections

joint, normalized centre deflections can be plotted against normalized force values for all drops. This influence is shown in Fig. 7.15 for all the load positions. For farther load positions and a higher load value, it is clear that the measurements are non-linear. Thus, it would not be possible to do a consistent comparison with the model for all the load positions keeping the model input parameters fixed. This shows the non-linear behaviour of the slab deflections when the load position relative to the joint and its value is changed. Additionally, the static nature of the model prevents from achieving an exact comparison as the dropped weights are dynamic loads.

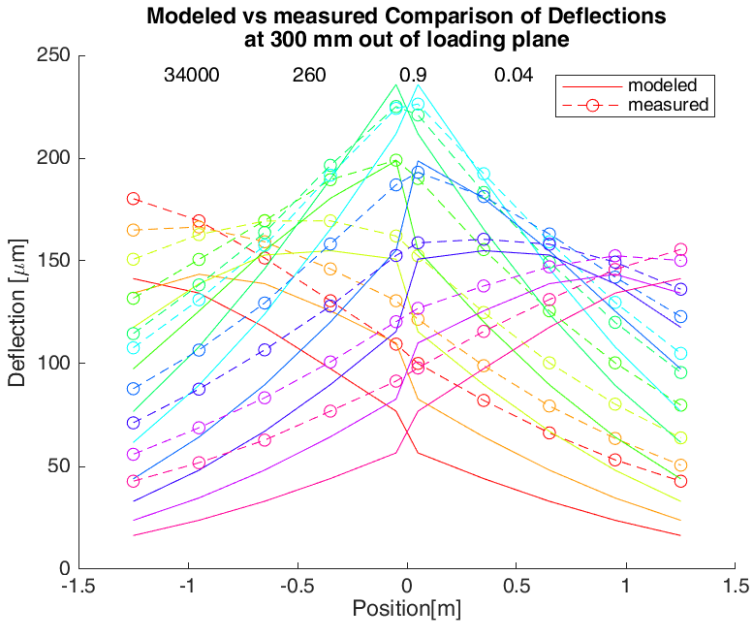

Figure 7.13: Fitting of full deflection bowls from 10 geophones for all ten drops

7.3 Reference beam mounted with laser experiment

From the previous experiment, the comparison of model and experiment with an impulse load proved to be challenging using a static model. Therefore, if parameters are not known load transfer efficiency can't be measured. Additionally, the non-linearity of pavement response is visible as the applied load is dynamic(caused by inertia effects) in nature.

After the previous experiment, it was concluded that a static experiment should be conducted. Thus, a reference beam experiment was planned where the load is assumed static as it is a slowly rolling wheel. The load comes from the Dynatest RWD equipment. This RWD equipment internally mounts high precision line laser sensors. These same sensors were used on the reference beam experiment presented here.

The next step is to use a long rigid beam mounted with Camera-based distance measuring sensors(gocators) to capture the deflections at fixed positions along center of the slabs across the slabs/either side of the joints. The edge is crossed by the moving load perpendicular to the jointed edge, while measurements are recorded as the wheel is moving. In fig. 7.16, a representation of this setup in top view and front view is shown.

Then for these load positions, the model can predict the response of the pavement as all model input parameters are known except joint efficiency, modulus of slab and foun-

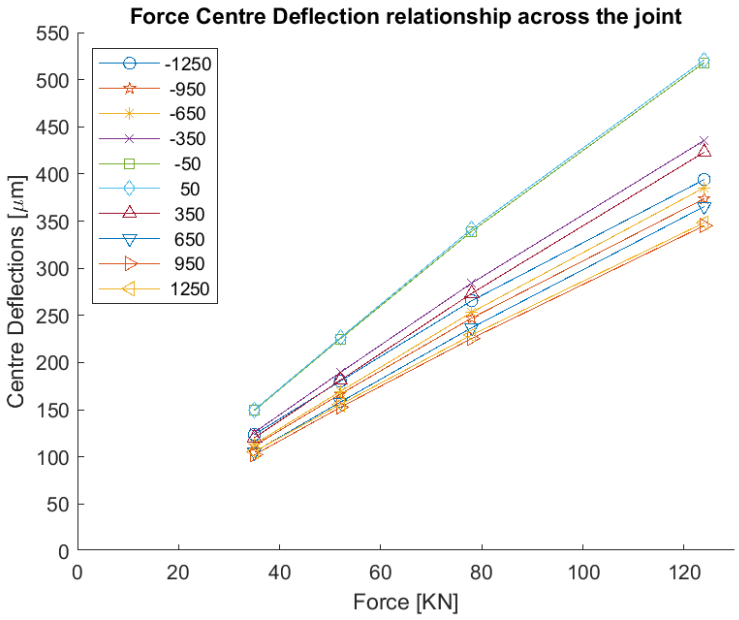

Figure 7.14: Centre Deflections of rigid pavement vs. increasing force for different distances to the joint(mm)

dation stiffness. Modulus and foundation stiffness are assumed from the cross-section details. Then, by utilizing the measurements from the experiment, a way to measure joint efficiency is expected to be arrived at.

This test should help understand the process and methodology to use continuous measurements under the influence of a rolling wheel load. These continuous measurements and this experimental development should also provide a quantity to measure load transfer. It is expected that this quantity is based on deflections. This step should also help the development of the steps in post-processing of the measured data. This step is focussed on measuring joint efficiency and will rely on the use of the model in tandem with the measurements. Therefore, the model will also be tested for predicted deflections concerning the sensitivity of input parameters.

7.3.1 Objective

1. To arrive at a process to measure joint efficiency (LTE) from line laser sensors.

2. Discover the model input parameters which influence the deflections.

3. Use this measured response and understand its relationship to load transfer efficiency

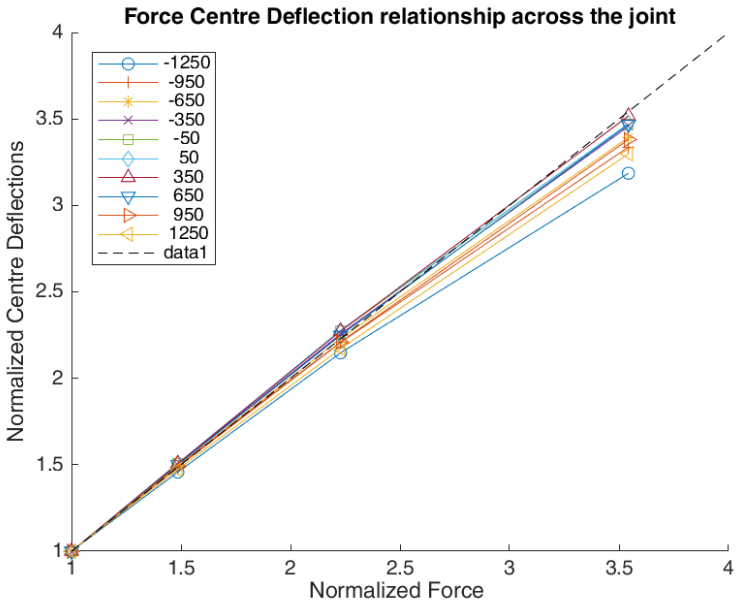

Figure 7.15: Non-linear Deflections of rigid pavement vs. the normalized force measurements.

7.3.2 Experimental setup

The measurement system comprises the lasers, odometer (encoder), a reference beam, an Ethernet switch, a power supply, a moving load and a recording application.

To measure the edge deflection response of jointed slabs under the influence of a moving wheel load, a beam mounted with distance lasers is set up. This beam is placed across the joints in the centre of two jointed slabs. The beam is mounted with 7 distance lasers such that the middle laser is placed above the joint formed by both the slabs. It is a symmetrical setup across the joint. The beam is 6m in length and mounted on two supports, one at each end. The beam has a rectangular cross-section with channels for mounting brackets (for laser housing) and supports.

The load is from the RWD's moving wheel which carries 5 tons. The loaded wheel is a part of a trailer which has an independent suspension in the rear axle. The trailer is attached to a truck and driven at a slow and controlled speed for the experiment. The other axles are the truck axles which are at least 6 meters away and therefore ignored. Their influence is not significant at that distance. Initially, the trailer is moved to a far

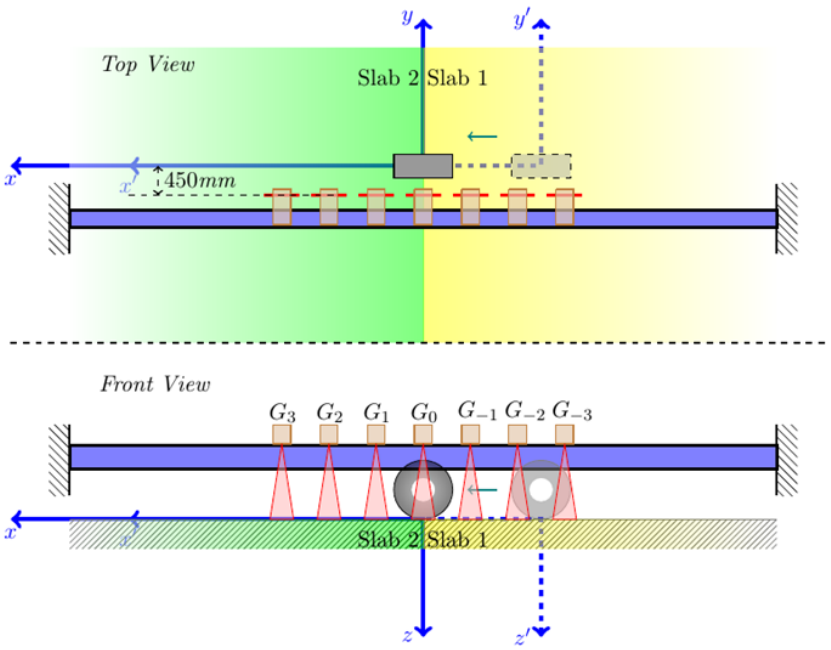

Figure 7.16: Schematic of the Fixed beam reference Experiment

location from the joint. During the experiment, the load is moved parallel to the beam. The idea is to get as close as possible to the beam in the longitudinal direction to receive a good signal.

An accurate odometer device, which measures the moving position of the wheel load at all times is used. This device is known as an 'encoder' and is attached to the moving wheel. The signal from the encoder comes from a cable attached to it. This cable is connected to the whole measurement system. The output from all sensors is saved via a recording application and is linked in time to all the laser measurements.

The distance laser is a camera-based laser which measures the distance perpendicularly below its base across a line profile. The base of the laser is parallel to the beam top surface when mounted. In this orientation, the profile that is being scanned by laser is parallel to the beam's length. The laser has two slots/openings facing the ground when mounted, one for the light source and the other for the camera to read the reflected signal. The width of the beam is chosen such that the laser's camera and the light source does not interfere with each other. The height of the beam's supports is such that, when the beam is mounted, the lasers on the beam are in their measuring range as per specifications. Laser specifications are listed in Table 7.1. Scan rate is the maximum rate at which the

Sl. No.	Specification	Value
1	Scan rate	5000 Hz
2	Clearance Distance	190 mm
3	Measurement range	210 mm
4	Data points/profile	1280
5	Repeatability Z	1.2 μm
6	Weight	0.94 kg
7	Field of view(near and far)	96 mm,194 mm
8	Resolution Z(near and far)	10μm,40μm

Table 7.1: Laser Specifications used in the experiment

lasers can measure. Clearance distance, Measurement range and Field of view are shown in Fig. 7.17. The lasers are placed inside a housing bracket which is then fixed to the

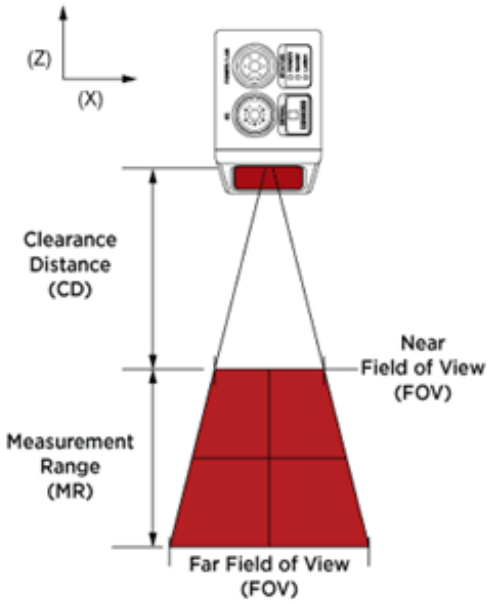

Figure 7.17: Coordinate system of the laser measurement system

top of the beam. To power these lasers, transfer data and control their properties as Input/output operations, a single cable that connects to an Ethernet switch and a Laser Master is used.

Measurement at Værløse Airport

To begin with, the site with joints was selected after visual inspection. After inspection of selected slabs forming the joint, the reference beam setup is placed across it symmetrically. The distance of the beam is measured from parallel edges of the slabs to make sure that

the beam is in the centre. All the connections to lasers and Ethernet switches are made, and the laptop is checked for measurement readiness with a custom recording application. Then, coloured markings(spray paints) on the slabs at incremental distances parallel to the laser signal are made to assist the person driving the truck for visual guidance.

After all the verifications, the measurement starts. The truck is moved to 4 slabs distance away from the joint under consideration with its front axle on the edge of the 4th slab. With a slow and constant driving speed around 10 km/h, the truck is carefully driven to avoid vibrations and maintain parallel distance to the lasers, when it arrives close to the beam. Throughout the measurement, attention is paid to the encoder cable coming from the rear side of the trailer. After the loaded wheel axle of the trailer carrying the 5 tons has passed in front of beam and onto another slab, measurement is stopped, and the collected data is saved. This process is repeated for several joints at the site. Repetitions of this experiment are done for the same site, to check the consistency of results. In Fig. 7.18 and 7.19, snapshots of moving load(RWD device), crossing the beam have been shown.

Figure 7.18: Side view of the setup during experiment

After the experiment is finished, the processing of the measurements needs to be set up. Raw measurements are processed carefully. Measured data from lasers is in its own geometrical coordinate system. This data is converted to height. Laser mounting

position on the beam and moving load position relative to the selected joint are accounted for during processing. Measurements from lasers at the beginning of each experiment are subtracted from the whole signal to get deflections under the influence the load. Deflections capture also the effect when the load is near the support. There are 3 axles of the truck-trailer setup and measurements include deflections from all these axles as each of them passes in front of the lasers one by one. Measurements from lasers are high-frequency and with 1000 points (pixels) over a 160mm line width in space. To obtain a processed measurement signal without losing useful information, manual averaging of data is done. The signal after averaging allows identifying the influence of each axle in the measurements. The segment of a signal containing the deflection from the 5-ton loaded wheel is separated and can be compared to the modelled deflections across the joint.

Figure 7.19: Mounted lasers measuring during the experiment

7.3.3 Modelled Deflections for the experiment

The 3D semi-analytical model predicts the deflection field over the jointed slabs for one position of the load. During this measurement, the moving wheel generates deflections all over the slabs against time, so multiple realizations of the model with incremental load positions are considered. This model can predict multiple static cases to arrive at a continuous deflection profile. This generates a series of deflection responses to form a

signal which can be compared to the measurements. The part of the measurement that contains the joint is modelled. To account for the influence of sinking of the beam's end support, a linear combination of deflections from cases when the load is in front of the beam's support and near the edge is also implemented. The sinking happens because the slab deflects down when the load is in front of the support, resulting in sinking of the beam. In the end, the deflection at the edges of the slab containing the joint is modelled for cases when the wheel simultaneously loads both the slabs, after which the modelled deflection is ready for the comparison.

7.3.4 Results

Deflections from the tested site are presented in Fig. 7.20. This site was measured three times for repetition. In plots, the x axis represents the position of the load and the y axis represents deflections measured by the laser(G^0) over the joint in microns. The joint is approximately positioned at $x = 0m$ for all test runs. The deflection measured just left of the joint position is marked as 'Modeled Approaching site' and to the right it is marked as 'Modeled Leaving site'. In plots, selected load positions range from $-8m$ to $8m$ which includes the effect of the loaded wheel. Measured deflections range approximately over -100 microns to 50 microns. The symmetric peaks in the deflection signal at $x = -4m$ and $4m$ appear due to the contribution from the load crossing the other joint and then approaching the beam's support. This shows the joint can detect the load's influence even when it is far from the joint. Deflection values at the joint of the slab as a function of the load position are ultimately measured.

Information about the moduli, subgrade and load transfer is unknown. However by assuming a set of realistic values for these parameters, the model can generate deflections. No rotation effect of slab is included, as this is not a part of the slab model. This set of parameters is kept constant for the repetitions while comparing modelled deflections to measurements for the same site. A comparison of the measured signal to the modelled signal shows the match of the peaks in Fig. 7.20(a). Modelled deflections to the left and right of the joint match the trend in the measured data. Sinusoidal noise could be due to

oval shapes of contact patch of the tyre on slabs.

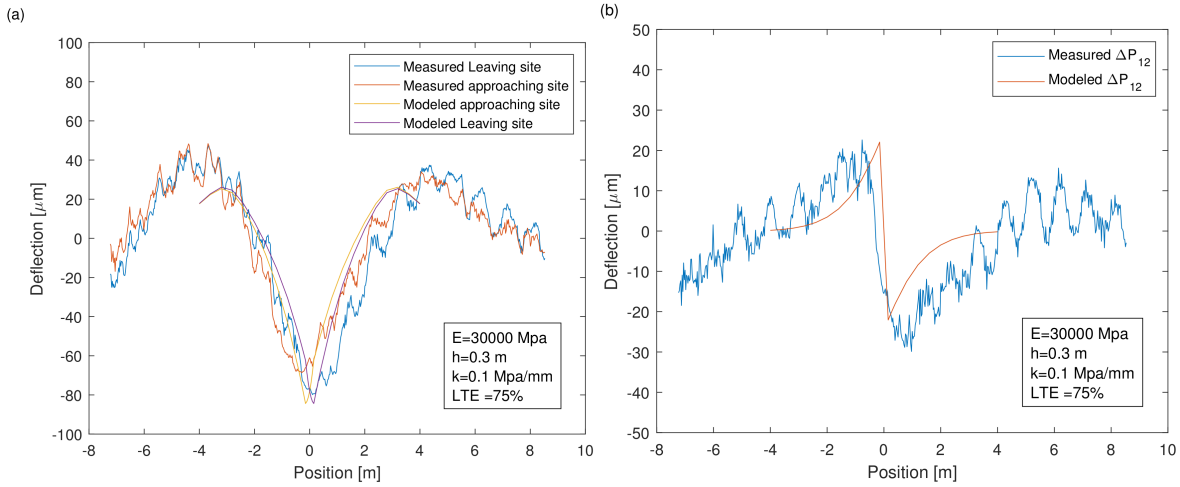

Figure 7.20: Comparison of (a) modelled vs. measured deflections (b) modelled vs measured deflection difference

This comparison provides insight into how the deflections behave as a function of load position when the measurement is focused on the joint, the deflection values are captured from both sides of the joint, including noise in the measurements. Such behaviour could be due to many reasons; thus, the difference in deflection signals marked as 'Modelled Approaching side' and 'Modelled leaving side' is compared to the model for a better understanding. It is observed that the profile matches the modelled deflection difference better as small vibrations are cancelled in this difference and the shape is more like the one predicted by the model. Modelled deflection difference is the difference of measurements from approaching side and leaving side separated by the joint. It is shown in Fig. 7.20(b). This comparison demonstrates that the model can predict the response due to a moving load close to the joint. Given some structural information on the pavement, results indicate that this model can be used to back-calculate the properties of the slabs from the measurements and eventually the load transfer capability of the slabs.

This experiment also demonstrates the capability of the measurement system and associated sensors to capture deflection in the order of microns without embedding the sensors inside the structure. It's a simple demonstration of nondestructive evaluation by a slow-moving load. A more advanced measurement system based on the setup used in this study forms the Dynatest Rolling Wheel Deflectometer technology platform, which will

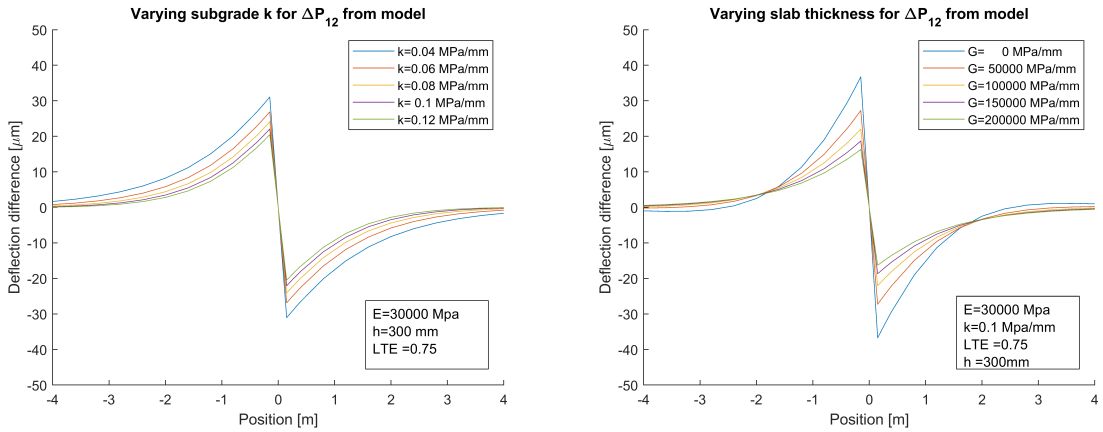

Figure 7.21: Variation of deflection difference across the joint for different (a) Subgrade stiffness k (b) Subgrade shear spring G

be the next experiment in this series of experimentation.

7.3.5 Sensitivity of modelled deflection difference to Model parameters

Here, a sensitivity study will use the model to investigate to which degree deflection difference depends on the parameters characterizing the joint. In particular, it is hoped that the deflection difference has a high sensitivity to the load transfer efficiency. In Fig. 7.21(a), deflection differences across the joint increases in magnitude across the slabs as the subgrade reaction k decreases. In Fig. 7.22, deflection difference values are much less sensitive to the change of moduli. These results are from the model only and not from experiments.

In Fig. 7.22 (b), changing slab thickness affects the shape close to the joint in a pronounced way. Lastly, the load transfer parameter is varied, and it has the maximum sensitivity to predicted deflection differences, which can be seen in Fig. 7.23. As expected, the deflection difference has a high and specific dependence on the load transfer and is therefore well suited as a main parameter in a back-calculation process. A higher sensitivity means that, given the measured response is accurate and information about the pavement is known, then other parameters including the load transfer can be calculated with a higher degree of accuracy. This study thus confirms that it is reasonable to measure load transfer using

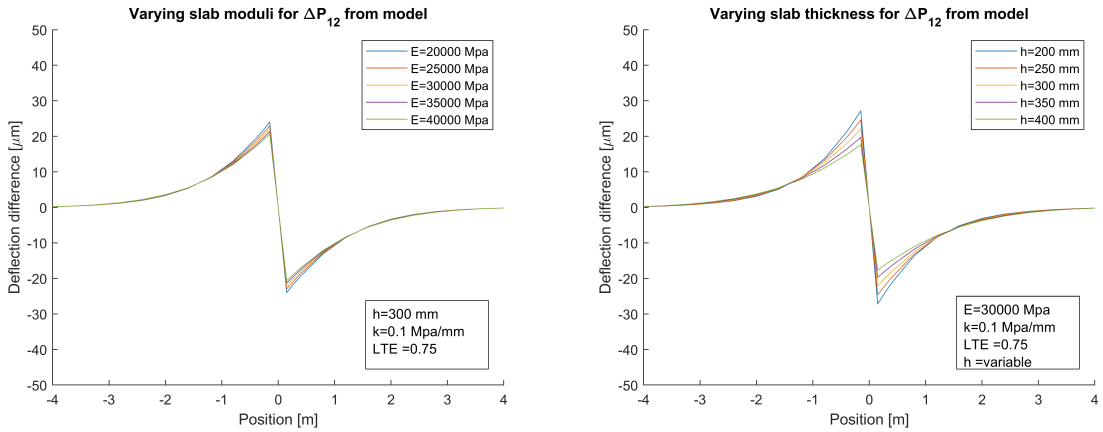

Figure 7.22: Variation of deflection difference across the joint for different (a) Slab Moduli (b) Slab thickness

RWD type equipment with laser technology, as long as it is possible to remove noise in post-processing. For this experiment the measuring system was stationary, therefore it was possible to achieve that.

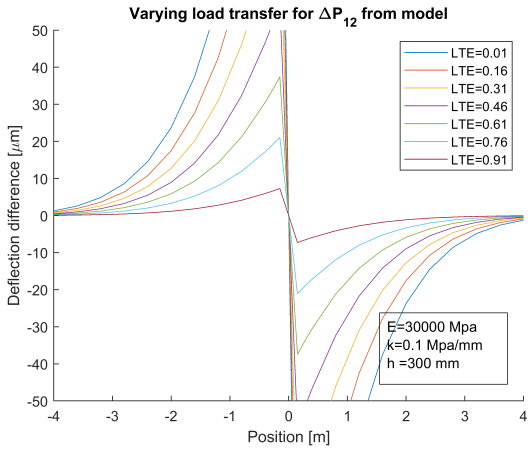

Figure 7.23: Variation of deflection difference across the joint for different LTE

The next experiment was planned with an RWD device manufactured by Dynatest. Before the experiment is presented, detail about the prototype Dynatest RWD based device called Raptor is presented in the next section.

7.4 Rolling Wheel Deflectometer

The Dynatest RAPTOR also called Rapid Pavement Tester or RPT, is a new platform which integrates the RWD technology with other devices like a Laser Crack Measure-

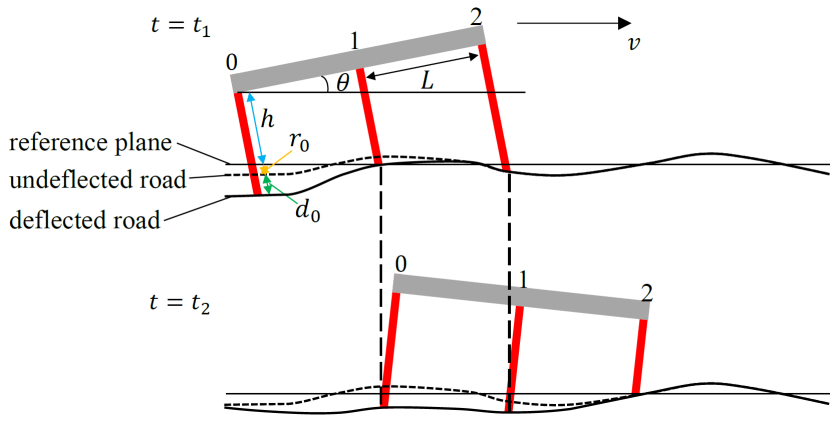

Figure 7.24: sketch of the RPT beam (gray line) with 3 lasers and laser beams (red lines) at times t_1 (top) and t_2 (bottom). Shown is the reference plane (full thin line), the undeflected road (thick dashed line) and the deflected road (thick full line)

ment System (LCMS), to collect both structural and functional data simultaneously. The RAPTOR is a single high-efficiency platform, able to operate at high speed to collect data continuously and without the need for traffic interruption or lane closure. It will provide affordable data at a low cost per km, reducing the amount of money and investments needed for road analysis.

The idea behind the Dynatest rolling wheel deflectometer lies in measuring the curvature but not the curvature differences, where curvature implies a radius of curvature, which is approximately the second derivative of deflection. In fig 7.24, to remove the effect of initial starting measurement position, and surface texture, and to measure the effect of pressure load, second order difference is used.

Using different combinations of high-frequency lasers positioned equidistantly on the horizontal beam perpendicular to the axis of the wheel, measurements of curvature are obtained. These values of curvature are tied to position in space using digital image correlation(DIC). DIC is used to find the same location on the road when two lasers traverse at different time instances over each other on the same patch in the pavement. An image of the traversed patch is compared to the image of another patch in time. Each laser measures the absolute vertical distance in its coordinate system and it spans over a width termed as the tracking window. It is possible to remove pavement texture, beam rotation and translation induced due to dynamic movements due to movement of the vehicle by

subtracting the absolute vertical values coming from other lasers at different instances of time and then by using DIC to give measurements in the form of curvatures. There are several calibrations done on the measurement data. This method which is employed by Dynatest is an improvement over the Harr algorithm, which measured curvature differences. Now to arrive at deflection from curvature, curvatures are integrated twice to obtain the deflection, which is therefore not a raw measurement, which is not the case with the Falling Weight Deflectometer.

The back-calculation method used with the Falling weight deflectometer is still used in Rolling wheel deflectometer calculations. Based on the method and computational cost of back-calculation, one can choose to average the measurements in space from the Rolling wheel deflectometer in the back-calculation.

7.4.1 Trailer description

The RAPTOR is a custom-made trailer which can be towed with a standard truck. The trailer is $9.5m$ long, $2.5m$ wide, and it has an adjustable height from 3.15 to $3.35m$. Due to these small dimensions, it can easily be towed inside city areas or narrow roads. This allows the Dynatest RAPTOR to test on almost every road since it is the smallest Rolling Weight Deflectometer to date. The trailer has two independent single wheels which make the loading process easier. This process is supported by the hydraulic system that modifies the height of the trailer. A ballast frame raises the weight applied by the single rear axle from 6 up to 10 tons (100 kN); by using different amounts of the ballast it can easily be modified depending on the testing purposes. Due to the independent wheels, the ballast can be loaded without any external device. Looking at Figure 7.25 and 7.26 is possible to see the ballast loaded in the middle of the rear axle, and the rails to load it into the trailer. A single operator can drive the trailer backwards at its lower height and the ballast will slide into rails placed in the middle of the trailer between the wheels. Then, with the ballast still standing on the ground, the hydraulic system will lift the trailer and the ballast.

The two independent wheels have an advanced suspension system, which reduces the

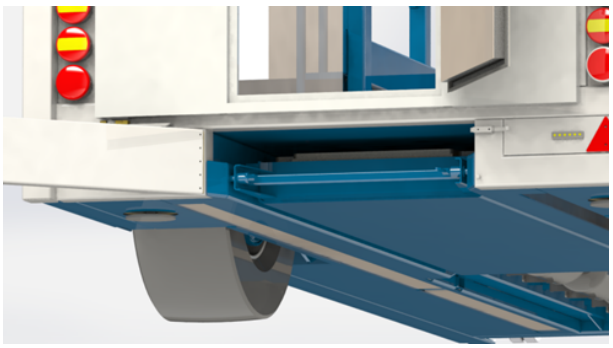

Figure 7.25: Drawing of the load ballast placed on special rails on the lower part of the trailer

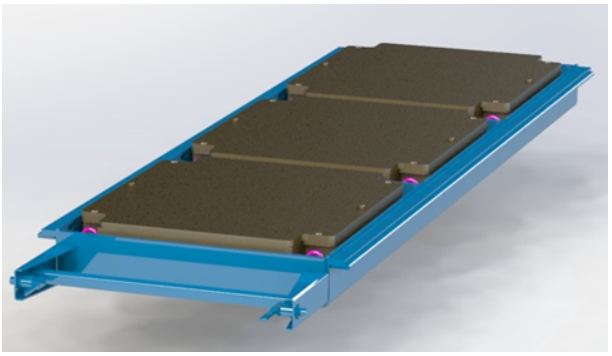

Figure 7.26: Drawing of the load ballast placed on special rails

bouncing of the trailer while it's towed on a rough road. A drawing of the suspension system and an accurate description is shown below.

Inside the trailer, a climate system maintains a constant temperature. It is important to have the same temperature inside because the beam supporting the laser sensors to be affected by temperature changes and all the lasers are also temperature calibrated.

A door in the rear part allows personnel to go inside to work on the devices for maintenance repairs, calibration or data analysis. Figure 7.27 and 7.28 show the frame and the structure of the RAPTOR trailer. The complete trailer is shown in Figure 7.29.

Figure 7.27: Drawing of the frame of the RAPTOR trailer (Side view)

Figure 7.28: Drawing of the frame of the RAPTOR trailer (Isotropic view from below)

Figure 7.29: Picture of the RAPTOR trailer

7.4.2 Data collection devices

The RAPTOR trailer uses line lasers 2340 from **LMI technologies**. All the technical information and features of these sensors are described in previous sections. There are nine line lasers and 18 available slots on the supporting beam. This allows a high number of different configurations of the sensors, which can be modified to collect data at specific points to increase the accuracy of the measured deflection basin. Since there are many slots available it's easy to add more sensors, which may be unequally spaced. Additionally, the supporting beam is fixed on the frame across the wheel, so on the new RAPTOR trailer it is possible to place line lasers also in the rear part of the deflection basin. All the sensors are powered and connected to a master, which collects the data from each line laser and sends the output to the main computer. Another important improvement is in the beam supporting the line lasers and consequently in its configuration with the load. Dynatest developers have solved the bending problem of the beam in two ways:

- A stiffer beam made by carbon fibre, supported by an aluminium frame.
- A temperature control system, which keeps the beam and the line lasers at a constant temperature to avoid thermal expansion.

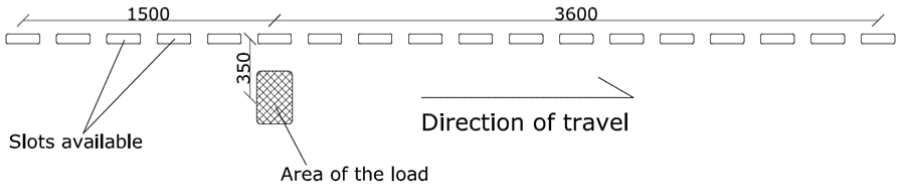

Figure 7.30: Available positions for the Line lasers and relative distance to the closer loading wheel

These two solutions solve the bending problem of the beam. The new configuration of the available slots for the line lasers is shown in Figure 7.30. The slots available for the line lasers are equally spaced at 300 mm, and the beam is closer to one of the footprints of the loading wheels. Consequently, with the new RAPTOR trailer it is possible to collect data closer to the load, which allows a better evaluation of the centre deflection compared to the old prototype. The supporting beam is fixed to one side inside the trailer with a rail system. Usually, it is on the right side of the trailer, but due to the symmetrical components, it can easily be moved to the other side. The line lasers collect a complete scan of the road surface using consecutive lines scanned, approximately 150 mm wide. These scanned lines will form a "virtual image", called virtual because it is not a real picture since pixels represent a distance. They can work with a frequency up to 5000 Hz, depending on the size of the field of view. This new RAPTOR trailer is towed by a standard truck. It will test at higher speed; therefore the distance between two scanned lines will be higher. Unlike the TSD, the Dynatest RAPTOR has no lower speed limit, so it can test at any speed from 2 to 100 km/h. Using the same principle and algorithm developed for the RAPTOR prototype, curvatures are evaluated using the measurements of three laser sensors and a gyroscope. The three sensors considered still have to be equally spaced. The image correlation process is still applied to ensure that the three sensors used to evaluate the curvature are collecting measurements exactly over the same point on the pavement.

The list of devices installed on the beam is completed by:

- 3 accelerometers, capable to measure in three directions
- 2 gyroscopes

- 5 air temperature sensors

The accelerometers keep track of the movements of the trailer, and so of the supporting beam. Accelerometer data corrects the reading from the sensors, removing from the measured deflections the contribution due to movement of the trailer instead of the deflection of the pavement. The gyroscopes provide the inclination data used in the algorithm to calculate the curvature. The air temperature sensors ensure that all the line lasers are measuring at the same temperature. These provide feedback on the performance of the climate system, which should keep a constant temperature inside the trailer, solving the temperature sensitivity problem of the line lasers.

7.4.3 Calibration System

The new RAPTOR trailer is equipped with a specially designed reference surface which can be scanned to calibrate the line lasers. This means that with the new equipment is possible to calibrate the laser sensors on-board within a few minutes, without driving back to the workshop. The reference surface provides a standard calibration which has a zero deflection and never changes, therefore the data collected are not affected by any difference between the calibration methods used on different days.

A rails system allows the beam to be lifted vertically, from the measuring position close to the floor to an upper calibration position. From the upper position, the sensors can scan the reference surface which is stationary while the measurement beam is moved horizontally. There are two sets of vertical rails. One set is placed near the floor, and they are stationary, and used for measurements and transport. The other set is placed near the roof, and they are mounted on a set of horizontal rails for horizontal movement used during calibration. Hydraulic brakes lock the beam in any vertical position. The brakes are normally closed, so if all the power system fails the beam is still locked. The beam cannot move vertically if the brakes are locked, but it can still move horizontally if the beam is positioned on the upper set of vertical rails. Therefore, the beam should typically be set in the measurement position on the lower set of vertical rails for transport.

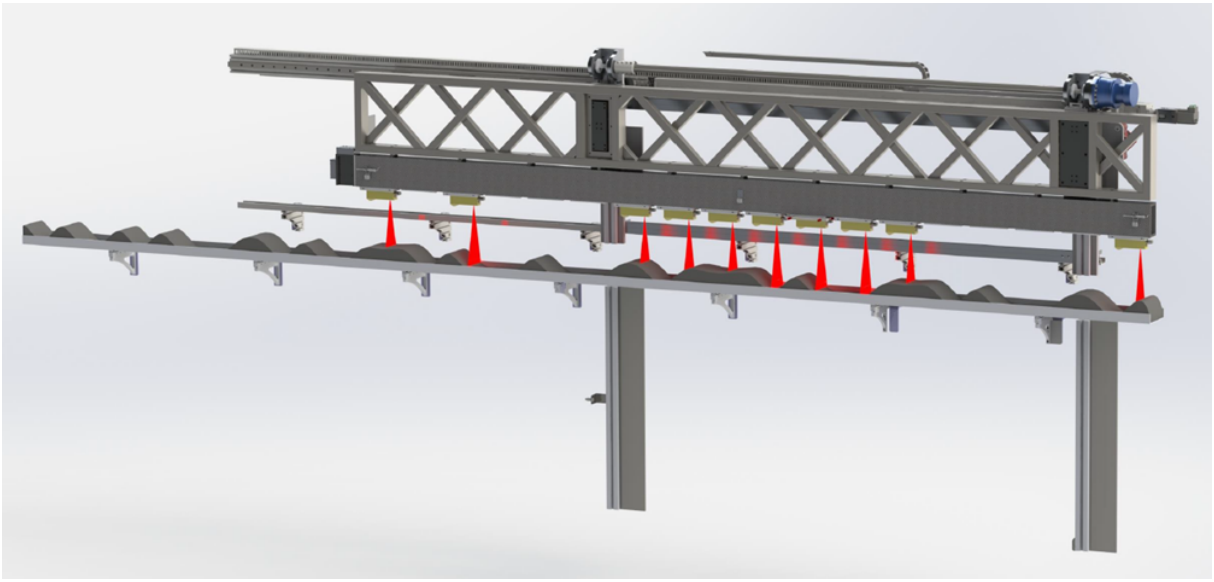

Figure 7.31: Calibration system integrated into the RAPTOR trailer, with vertical and horizontal rails to scan a reference surface with the Line lasers.

Two motors move the beam, one for the horizontal movement and one for vertical. A set of sensors detect the position of the beam, shutting down a motor when the beam reaches certain positions.

The reference surface is a stiff beam with zero deflection supported by the rail system. It is made with a colour which simulates an asphalt concrete pavement. The main purpose of the reference surface is to have a shape which never changes, to calibrate the line lasers always on the same reference. With the rail system, the beam supporting the line lasers is lifted vertically to a predefined position. Suddenly the reference surface is placed below the laser sensors and fixed in that position. The beam supporting the line lasers is moved horizontally so that the sensors can scan the reference surface. Knowing the results which the line lasers should measure on the reference, the data collected during this calibration process modifies the input calibration parameters of each line laser. The main advantage coming from this new way to calibrate the line lasers is its reliability. The surface reference always provides the same surface to perform a calibration process every time it's needed. The calibration can be made in every situation, and it doesn't require any external device. This allows for fast and frequent calibration, which improves both accuracy and consistency in the data. Figure 7.31 gives an overview of the calibration

system.

7.4.4 Using RWD technology for continuous evaluation of JCP pavements

The RAPTOR is intended to be a screening device at present and is designed for use on flexible pavements. From technical specifications, it is clear that the expected accuracy of sensors is lower if compared to the FWD's geophones. The line lasers used on the RAPTOR have an accuracy around 20-25 µm, while the geophones used on the FWD have an accuracy ten times smaller, of 2 µm. Nonetheless, with this research, it is hoped that an increase in sensor accuracy in an RWD device with higher loads on one independent wheel will be possible in the future, in which case a method to analyse such measurements would be ready.

Jointed concrete pavement (JCP) poses a problem for continuous deflection measurement

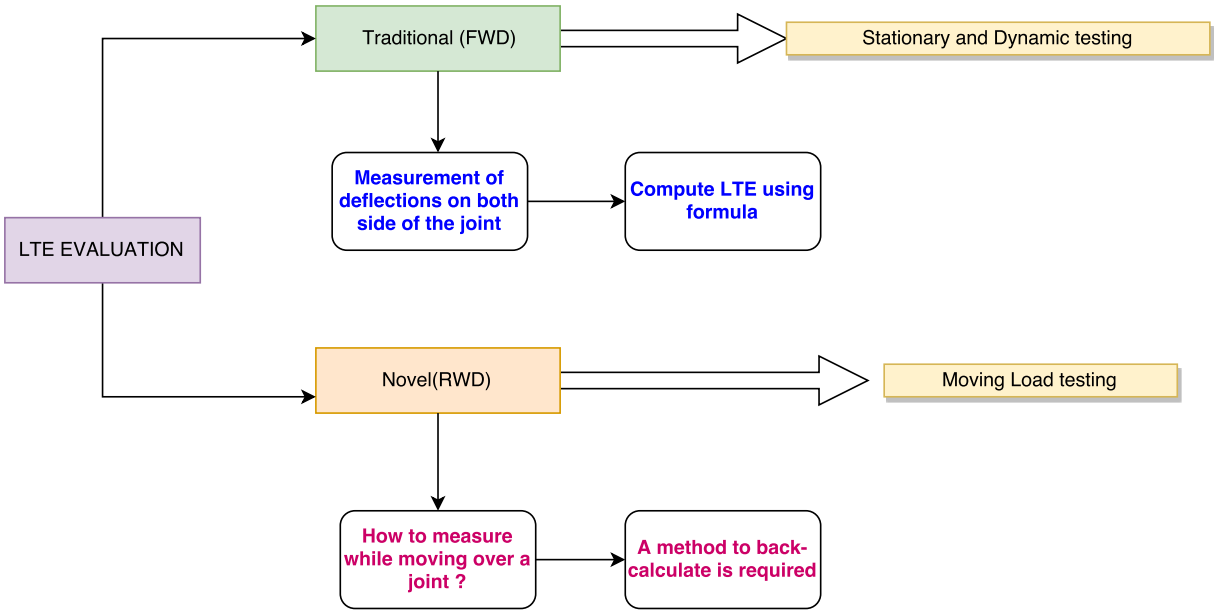

Figure 7.32: LTE evaluation

devices in general because they are stiffer, whereas JCP testing when done with FWD and similar devices is relatively easy. With the advent of continuous deflection measurement devices, there have been several attempts experimentally to present correlation of peaks in deflection to the low load transfer efficiency as measured by the FWD at the same

joints as in [73], [15], [17], [27]. These techniques to measure the load transfer efficiency are defined. With continuous measurement devices, investigation into its applicability requires research. Therefore, in this context, the aim of LTE evaluation is represented in Figure 7.32, where it is hoped that with this research the knowledge and tools required for analysing the data for rigid pavement continuous evaluation are put in place.

7.5 Dynatest Raptor experiment

From the previous experiment with a reference beam, deflection difference can be used to measure joint efficiency, if other parameters are known. LTE has the highest influence when it comes to model input, and so is the ideal candidate to be accurately measured/back-calculated after analysing the measurements. Therefore, it was concluded that if the noise in the measurements is filtered out or removed via data post-processing, for example by arriving at deflection difference from measured deflection, it is possible to measure joint efficiency.

Now for the last experiment in this research with the Dynatest Raptor, it is hoped that the measurements can be analysed in a way to arrive at joint efficiency. Although the equipment is designed for flexible pavements, however it should provide results that will allow precise expectations from future versions of the RAPTOR device to be formulated.

7.5.1 Objective

1. To understand and analyse the raw measurements from the Dynatest Raptor RWD device across joints.

2. Compare these measurements to the previous reference beam experiment.

3. Draw conclusions on the scope of usage of the present Raptor device.

7.5.2 Continuously measured slab sections

When a Raptor RWD trailer starts measurements, it collects a stream of images of the pavement surface below it via lasers. There are 12 such line lasers. An example of this measurement can be seen in the image shown in Fig. 7.33. In this image, dark vertical lines are the joint locations and each row corresponds to measurements as the trailer moves, so in the first row, it can be seen that the Raptor though measuring, is not moving as the details in the first row are repeating. The hieght of the row is equal to the length of line laser projection on the pavement which is around 160 mm. This provides a sense of the data being captured. On the greyscale, darker regions are farther away and lighter regions are closer to the laser.

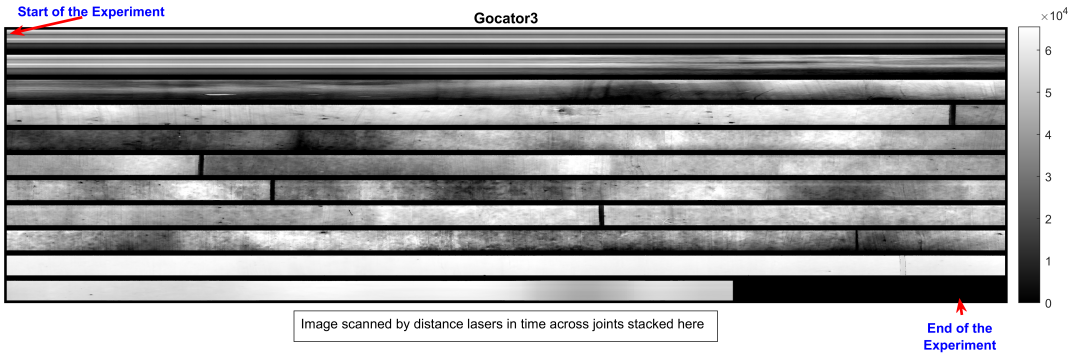

Figure 7.33: Image from a Gocator inside the Dynatest RAPTOR

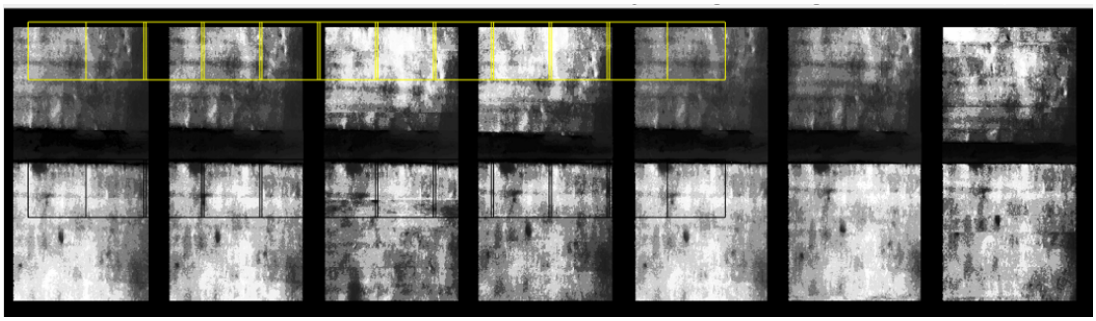

Figure 7.34: A Joint tracked by 7 Raptor gocators (One column contains the measurement of a small patch of before and after including the joint i.e. dark horizontal line)

It is possible to select a ground position outside the device to do repeated measurements and analyse these measurements. For this experiment, joint locations in the measurement data are selected. The joint fortunately here has a distinctive feature that appears as a

dark thick line in sensor image data. Therefore, when a single joint is seen by all the gocators one by one, it can be visualized. In Fig. 7.34, a single joint when seen by all the gocators inside the Raptor trailer is shown. It can be observed that though the joint is the same, the image varies in contrast and has noise. Note that the images are for a short pavement stretch before and after a single joint.

7.5.3 RWD across a joint

At different distances relative to the position of the loaded wheel, there are 12 gocators mounted on the beam inside the Raptor trailer. The image from gocators across the selected joints is converted to a distance value. The image across a single joint can be seen in Fig. 7.34. This greyscale image contains information which can be converted to a distance value, which is composed of three components. These components are height of the beam, deflection of pavement and the texture of the pavement. Out of these components, the deflection of the pavement is needed to calculate the joint efficiency.

As the RWD device passes over the joint the wheels follow a straight line. It can be assumed that the beam does not undergo excessive rigid body motion. In Fig. 7.35, a moving loaded wheel for two time instants t_1 and t_2 is shown. At t_1, the gocator G_2 is just crossing the selected joint and is in front of the joint and after a brief time δt, that is $t_1 + \delta t$, the gocator G_2 is on the unloaded slab. At t_1, the distance of the wheel from the joint is known since the mounting positions of the gocators are predetermined. Similarly, at t_2, the RWD device has advanced by $300mm$ and G_1 is now front of the same joint and at $t_2 + \delta t$, the gocator is on the unloaded side. This movement repeats for all 11 gocators. Therefore, an image patch from a gocator for a small time-frame δt just before and after the joint is considered to give a measure of load transfer.

As stated previously the distance value is composed of 3 components. Now to remove the components that are not desirable, the image patch of the selected joint can be divided into multiple sub-patches to average the data and thus remove the noise. The desirable quantity, which is vertical deflection cannot be calculated from image measurements.

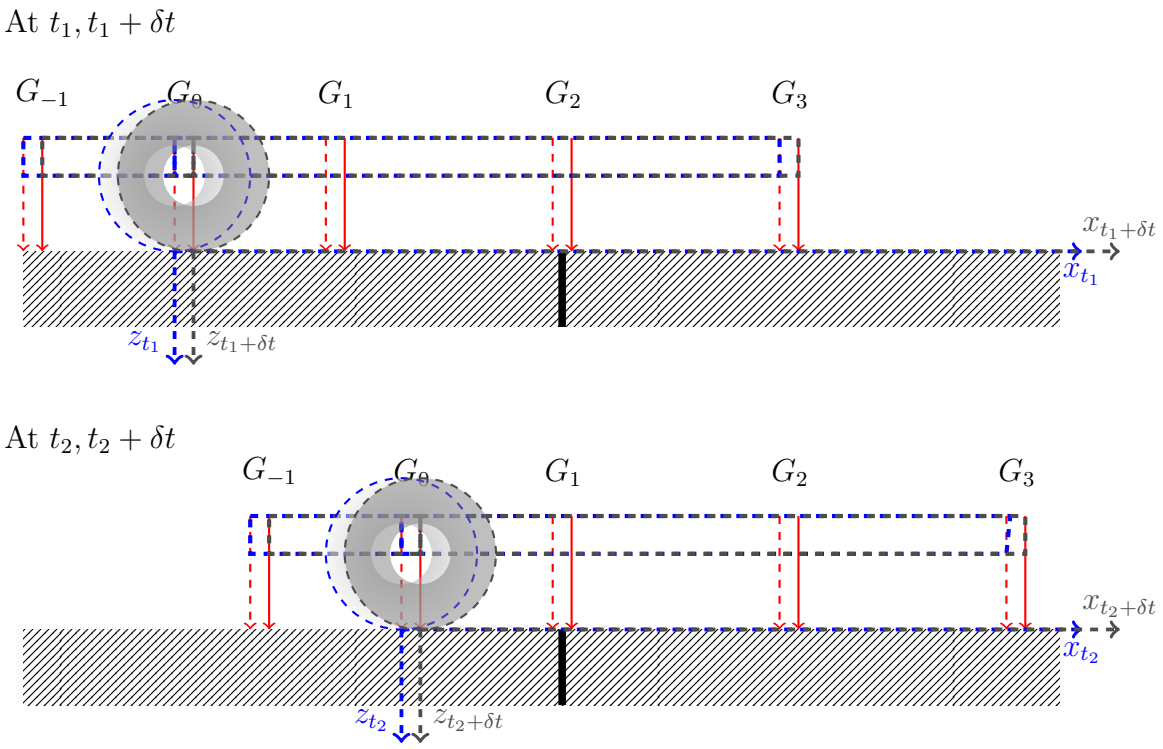

Figure 7.35: Relative positions of gocators with respect to the joint

Instead, a difference between values measured just before and after the joint should provide the deflection difference due to the load approaching the joint. At the same time, the difference would remove two components, the height of the beam and the texture. This continuous wheel load approaching the joint can be modelled to arrive at the deflection difference and then a comparison can be made to arrive at conclusions.

For every single laser, the difference of deflections over a small-time duration (δt), together with its distance to the load counts as a measurement. Therefore using the method for all 12 lasers, out of which three are before the wheel position and eight are in front of the wheel, 11 observations are obtained. These observations are also calculated for three runs for the same joint. For post processing, the measurement from the farthest laser position relative to the wheel position is considered to be the base measurement while plotting measurements close to the joint.

The moduli, thickness, pressure load and dimension of slab size are known from the design archives. Predetermined information such as distance of laser from the joint and the wheel position relative to the joint are inputs to the forward model developed in this study to

generate modelled deflection difference. The step of modelling the deflection value is repeated for all the lasers.

This step of arriving at deflection difference is carried out for all 11 gocators except for the gocator G_0 at the loaded wheel. This is because the wheel load patch will load the joint and both the slabs simultaneously and therefore it is skipped. Observing the measurements, it can be understood that the noise and variation still remain after post processing. These measurements are plotted in Fig. 7.36. Three runs of measured deflection difference are also marked as points for 11 load positions. The wheel load is located at $x = 0mm$ on the x axis. A measured deflection point at x=900mm means that the wheel load is 900 mm away from the joint and the value on the y axis represents the deflection difference measured across the joint at that instant.

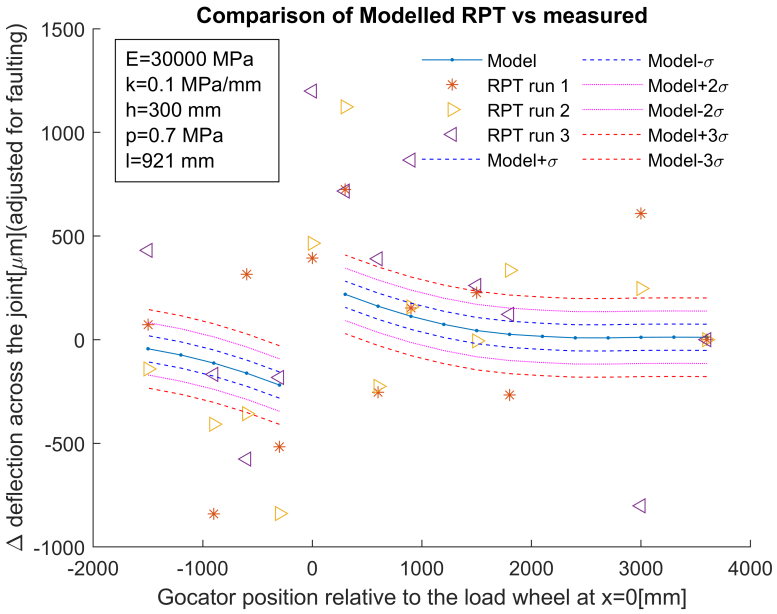

Figure 7.36: Modelled and measured response by 11 Raptor gocators

To do a comparison to the modelled deflection difference, a statistical standard deviation calculation is done. Three pairs of standard deviations at $\pm\sigma$, $\pm 2\sigma$ and $\pm 3\sigma$ provide upper and lower limits to compare to the measured values.

Note that in Fig. 7.36, there are three runs of the RWD measurements for which the comparison is made, the images for which from gocators for these three runs are shown in Fig. 7.37 for δt durations.

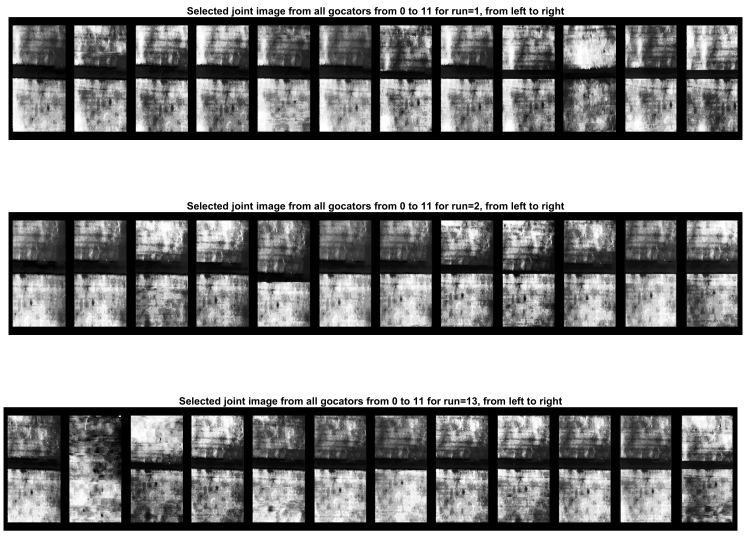

Figure 7.37: Variability in three runs (3 horizontal images) across the same joint, when measured with the Gocators

In the Fig. 7.36, deflection difference measurements lie with in the upper and lower limit of standard deviations for farther lasers and beyond that for lasers closer to the wheel. It is a positive result when the measurement system is moving measuring continuously with a system designed for asphalt pavements. The measurement variation is more for the lasers near the wheel. This could be because of the vibrations of the moving system and other unknown effects.

It is clear from Fig. 7.37, that the variation in the images of the same joint have persistent noise. This image also captures the repeatablity that is shown from This can be explained by the fact the beam might undergo a translation/rigid body motion. Additionally, the measuring range of line lasers changes with the motion of the Raptor device, which affects the lasers' accuracy to measure distances. The load on the wheel is 5 tons which was enough for the reference beam experiment where the laser was sitting stationary on a beam, but in the case of a moving Raptor device with sensors inside on a beam, it goes into motion. If the independent axle wheel load is increased it could be possible to arrive at raw measurements which could be sufficiently large to measure the load transfer efficiency. But this is not possible with the current device as the rear axle can not be loaded more than 10 tons in the present configuration.

While comparing this experiment to the reference beam experiment it should be mentioned

that the orientation of the laser sensors is different. In the reference beam experiment, the laser line was co-linear with other lasers on the beam and the laser in the middle was looking at the joints and edges of both the slabs simultaneously, which helped to measure the load transfer efficiency by using the forward model. But in the case of the Raptor trailer, the laser line is parallel to the joint edge, which creates additional complexity to be worked with. Nevertheless, it is not a significant issue.

Thus, if a higher load is used or a better more accurate laser technology is integrated into future Raptor prototypes, then by using the model developed in this research, joint efficiency can be possible to measure. The roughness of pavement texture can affect the reflected laser light, which can be a source of noise. The reflection of light is better for a darker surface for example asphalt as opposed to concrete(grey).

7.6 Summary

Throughout this chapter, a sequential progression on measuring the joint efficiency with experiments has been presented. The use of dynamic and static wheel load, use of geophones and line laser sensors, setting up of the offset of load plane and measuring plane, the highest sensitivity of deflection difference with respect to load transfer efficiency has been demonstrated. These developments show that using a continuous assessment by load types in devices which apply RWD ideology, it is certainly possible to measure the joint efficiency. The application and precise steps, however, would change from measuring sensor to sensor.

Nevertheless, if RWD based equipment is accurate enough for rigid pavement analysis, the developments in this chapter should allow the measured data to be analysed to arrive at the joint efficiency.

Chapter 8

Summary and Reflections

This research provides a novel implementation of a three-dimensional analytical model that predicts the response of a jointed plain concrete pavement. This implementation focussed on predicting and thus measuring joint efficiency. The validation of this implementation has been presented as a part of this research. Experiments exploring the challenges of continuous evaluation, such as deflection measurements on both unloaded and loaded slabs, the use of a classical deflectometer, separation of measurements and load plane and use of dynamic and static loads have been carried out to develop the understanding of the use of the model. This experimentation highlighted the advantages and demonstrated the scenarios, where measurements such as deflection difference can be used together with a model to measure the joint efficiency. The experimentation was crucial as it has shown the input parameters sensitivity to shown its particular usefulness to measure the load transfer efficiency. In the experiment with the RWD commercial device, the challenges of a moving beam and wheel system were visible, where a basic analysis of the raw measured data, before and after the joint, showed high variability in the deflection difference when compared to the model. This clearly shows the need to remove the noise in the data either by advanced modelling of the measurement system or improving the device capabilities. An ideal RWD device, where either the sensors are more accurate or the wheel is loaded to more than 5 tons on the axle, is needed to advance the experimentation. If such modifications are done then the study in this research can be used to measure the joint efficiency of JCP.

Reflecting on the research carried out, it has been the hypothesis that the RWD commerical equipment developed for flexible pavements would also work on rigid pavements, where there were anticipated challenges. This hypothesis helped the research to develop the required modelling which is exactly relevant for continuous evaluation to measure joint efficiency. Independent collaboration for model validation provided fresh eyes on the model development and thus progressed the research positively. Experiments that were carried out in controlled conditions, on an accessible actual rigid pavement section, helped to research the exact relevant understanding required for the aims of this research to be achieved.

Even though this thesis has concluded with a demonstration of what is possible, this work is a starting point on learning how to use continuous evaluation of rigid pavements for a fast and reliable joint efficiency evaluation. More research and experimental studies if possible in future in collaboration with commercial companies who manufacture RWD based devices should be carried out to further develop this research. The future direction and suggestions are summarized below:

- Experiments at different pavement sites, such as rigid pavement highways with RWD should be conducted at different weather situations.
- The developed model should be used with other RWD technologies such e.g. TSD.
- With further experimentation and different instrumental setups noise in the measurement can be well understood and thus additional research can help to reduce it.
- A heavy version of RWD equipment, where pressure load under a single wheel is more than 5 tons, can help to measure the load transfer easily.
- Use of improved/existing sensor technologies with better accuracy should help to reduce the noise in the measurements.

Bibliography

[1] F. H. A. American Concrete Pavement Association. Concrete pavement rehabilitation: Guide for load transfer restoration. Technical Report FHWA-SA-97-103, FHWA, https://www.fhwa.dot.gov/pavement/pubs/013179.pdf, 1997. 5

[2] J. Arora, S. Nazarian, and V. Tandon. Continuous deflection testing of texas pavements., 2007. 31

[3] A. Baucheron de boissoudy, P. Keryell, and M. Paillard. Mecanique des chaussees appareils d'auscultation- le deflectographe. (129), 1984. 30

[4] J. A. Bay, I. Stokoe, H. Kenneth, and others. Development of a rolling dynamic deflectometer for continuous deflection testing of pavements, 1998. ix, 15, 29, 31

[5] M. Bhatti, I. Molinas-Vega, and J. Stoner. Nonlinear analysis of jointed concrete pavements. 1629:50–57, 1998-01. 23

[6] A. Bohn, P. Ullidtz, R. Stubstad, and A. Sorensen. Danish experiments with the french falling weight deflectometer. volume 1, 1972-09. xi, 28, 29

[7] A. C. Brink. Modeling aggregate interlock load transfer at concrete pavement joints, 2006. 3

[8] L. Bronuela, H. David Lee, S. Ryu, and Y. Ho Cho. Cantilever and pull-out tests and corresponding FEM models of various dowel bars in airport concrete pavement. 83:181–188, 2015-05. 13

[9] M. Broutin. Assessment of flexible airfield pavements using heavy weight deflectometers. development of a FEM dynamical time-domain analysis for the backcalculation of structural properties., 2010. ix, 39

[10] M. Broutin and A. Sadoun. Advanced modelling for rigid pavement assessment using HWD. 14:3572–3581, 2016. xii, 75, 77, 78, 79, 81, 82

[11] A. Bush, J. Hall, JR, and M. Harr. Nondestructive airfield pavement testing using laser technology. In *International Air Transportation Conference*, page 1601, 1983. 34

[12] C. Byrum and D. Ye. Evaluating the effect of concrete slab curling on joint load transfer responses. (2305):43–53, 2012. 43

[13] F. J. V. Cauwelaert, D. R. Alexander, T. D. White, and W. R. Barker. Multilayer elastic program for backcalculating layer moduli in pavement evaluation. In *Nondestructive testing of pavements and backcalculation of moduli*. ASTM International, 1989. 20, 49, 50, 54

[14] C. Channakeshava, F. Barzegar, and G. Z. Voyiadjis. Nonlinear FE analysis of plain concrete pavements with doweled joints. 119(5):763–781, 1993-09. 13, 23

[15] D.-H. Chen. Field experiences with RDD and overlay tester for concrete pavement rehabilitation. 134(1):24–33, 2008. 38, 113

[16] D.-H. Chen, M. Won, and F. Hong. Investigation of settlement of a jointed concrete pavement. *Journal of performance of constructed facilities*, 23(6):440–446, 2009. 9

[17] D. H. Chen, M. Won, and X. Zha. Performance of dowel bar retrofit projects in texas. 22(3):162–170, 2008. 38, 113

[18] B. Colley and H. Humphrey. *Aggregate interlock at joints in concrete pavements*. Portland Cement Association Illinois, 1967. xi, 10, 11

[19] W. Davids. Foundation modeling for jointed concrete pavements. 1730:34–42, 2000-01. 69

[20] W. Davids and J. Mahoney. Experimental verification of rigid pavement joint load transfer modeling with EverFE. 1684:81–89, 1999-01. 10, 69

[21] W. Davids, G. Turkiyyah, and J. Mahoney. EverFE: Rigid pavement three-dimensional finite element analysis tool. 1629:41–49, 1998-01. 21, 50, 69

[22] W. Davids, Z. Wang, G. Turkiyyah, J. Mahoney, and D. Bush. Three-dimensional finite element analysis of jointed plain concrete pavement with EverFE2.2. 1853:92–99, 2003-01. 22, 69

[23] W. G. Davids. Effect of dowel looseness on response of jointed concrete pavements. 126(1):50–57, 2000-01. 13, 69

[24] W. G. Davids. 3d finite element study on load transfer at doweled joints in flat and curled rigid pavements. 1(3):309–323, 2001-07. 13, 21, 69

[25] W. G. Davids and G. M. Turkiyyah. Development of embedded bending member to model dowel action. 123(10):1312–1320, 1997. 69

[26] M. Elseifi, A. M. Abdel-Khalek, and K. Dasari. Implementation of rolling wheel deflectometer (RWD) in PMS and pavement preservation. 2012. ix, 40

[27] M. A. Elseifi, A. M. Abdel-Khalek, K. Gaspard, Z. Zhang, and S. Ismail. Evaluation of continuous deflection testing using the rolling wheel deflectometer in louisiana. 138(4):414–422, 2012-04. ix, 38, 40, 113

[28] M. A. Elseifi, K. Dasari, A. Abdel-Khalek, K. Gaspard, and Z. Zhang. Development of the triangular model for pavement evaluation using the rolling wheel deflectometer. 139(3):313–320, 2012. 37

[29] M. Filonenko-Borodich. A very simple model of an elastic foundation capable of spreading the load. *Sbornik Moskovkovo Elektro Instituta*, (53), 1945. 56

[30] B. F. Friberg. *Method of making embedded bars.* Google Patents, 1938-11. 12

[31] T. Fwa, K. Tan, and S. Li. Closed-form and semi-closed-form algorithms for backcalculation of concrete pavement parameters. In *Nondestructive Testing of Pavements and Backcalculation of Moduli: Third Volume*. ASTM International, 2000. 44

[32] T. F. Fwa and S. Chandrasegaran. Regression model for back-calculation of rigid-pavement properties. 127(4):353–355, 2001-08. 45

[33] T. F. Fwa, X. P. Shi, and S. A. Tan. Use of pasternak foundation model in concrete pavement analysis. 122(4):323–328, 1996. 19, 20

[34] C. R. Gonzalez and W. R. Barker. *Analysis of Airfield Concrete Slabs Connected by Continuous Elastic Joints*, pages 167–180. 20

[35] H. Guo, P. Jr, T. J, and M. B. Snyder. Maximum bearing stress of concrete in doweled portland cement concrete pavements (with discussion and closure). (1388), 1993. 13

[36] H. Guo, R. Larson, and M. Snyder. A nonlinear mechanistic model for dowel looseness in PCC pavements. In *Fifth International Conference on Concrete Pavement Design and RehabilitationPurdue University, School of Civil Engineering; Federal Highway Administration; Portland Cement Association; Transportation Research Board; Indiana Department of Transportation; Federal Aviation Administration; and American Concrete Pavement Association.*, volume 1, 1993. 13

[37] H. Guo, J. A. Sherwood, and M. B. Snyder. Component dowel-bar model for load-transfer systems in PCC pavements. 121(3):289–298, 1995. 13, 24

[38] M. E. Harr and N. Ng-A-Qui. Noncontact nondestructive determination of pavement deflection under moving loads., 1977. 34

[39] M. Hetenyi. Beams on elastic foundation. scientific series, vol. xvi. *Ann Arbor: The University of Michigan Press, University of Michigan Studies*, 1946. 56

[40] G. Hildebrand, S. Rasmussen, and R. Andrés. Development of a laser-based high speed deflectograph. In *Nondestructive testing of pavements and backcalculation of moduli: Third Volume*. ASTM International, 2000. 32

[41] Y. H. Huang and X. Deng. Finite element analysis of jointed concrete pavements. 109(5):689–705, 1983-09. 21

[42] A. M. Ioannides. Dimensional analysis in NDT rigid pavement evaluation. 116(1):23–36, 1990. 43

[43] A. M. Ioannides and G. T. Korovesis. Aggregate interlock: A pure-shear load transfer mechanism. (1286), 1990. 20, 41

[44] A. M. Ioannides, Y.-H. Lee, and M. I. Darter. Control of faulting through joint load transfer design. 1286:49–56, 1990. 13, 41

[45] E. A. Jensen and W. Hansen. Nonlinear aggregate interlock model for concrete pavements. 7(4):261–273, 2006-12. xi, 11, 12

[46] R. Johnson, P. Bondurant, and M. Marvin. A rolling weight deflectometer for quantitative pavement measurements. 1996. xi, 35, 36

[47] R. F. Johnson. Self-compensating rolling weight deflectometer, 1998-05-19. 36

[48] D. Jundhare, K. Khare, and R. Jain. Use of benkelman beams for measuring lte in whitetopping: An alternative tool to fwd test. *Journal of The Institution of Engineers (India): Series A*, 93(3):203–207, 2012. 27

[49] S. W. Katicha, G. W. Flintsch, B. Ferne, and J. Bryce. Limits of agreement method for comparing TSD and FWD measurements. 15(6):532–541, 2014-07-03. 33

[50] A. D. Kerr. A study of a new foundation model. *Acta Mechanica*, 1(2):135–147, 1965. 56

[51] L. Khazanovich, T. McPeak, and S. Tayabji. LTPP rigid pavement FWD deflection analysis and backcalculation procedure. In S. Tayabji and E. Lukanen, editors,

Nondestructive Testing of Pavements and Backcalculation of Moduli: Third Volume, pages 246–246–21. ASTM International, 2000-01-01. 44

[52] J. Kushing, W. Fremont, and E. Sutherland. Design of load transfer joints in concrete pavements. In *Highway Research Board Proceedings*, volume 20, 1941. 13

[53] J. LaCroix. Deflectographe pour l'auscultation rapide des chaussees. (3):191–1, 1963. 30

[54] P. Landouer. French equipment for airfield pavement load evaluation. In *Proceedings of a International Symposium on Bearing Capacity of Roads and Airfields, Volume 1, Trondheim, held June 23-25, 1982.*, 1982. 25

[55] P. Mackiewicz. Analysis of stresses in concrete pavement under a dowel according to its diameter and load transfer efficiency. 42(11):845–853, 2015. xi, 22

[56] P. Mackiewicz. Finite-element analysis of stress concentration around dowel bars in jointed plain concrete pavement. 141(6):06015001, 2015-06. 13, 21

[57] J. F. Madsen. Rolling wheel deflectometer, 2017-08-15. 41

[58] S. S. Madsen. Dynamic modeling of pavements with application to deflection measurements, 2016. 41

[59] S. S. Madsen, S. Krenk, and O. Hededal. Perfectly matched layer (PML) for transient wave propagation in a moving frame of reference. In *4th ECCOMAS Thematic Conference on Computational Methods in Structural Dynamics and Earthquake Engineering*, 2013. 41

[60] S. R. Maitra, K. S. Reddy, and L. S. Ramachandra. Load transfer characteristics of dowel bar system in jointed concrete pavement. 135(11):813–821, 2009-11. 13, 22

[61] S. R. Maitra, K. S. Reddy, and L. S. Ramachandra. Load transfer characteristics of aggregate interlocking in concrete pavement. 136(3):190–195, 2010. 10

[62] Mh. Poor US infrastructure could cost $1.4 trillion in 10 years. 2016-05. 8

[63] V. Muzet, C. Heinkele, Y. Guillard, and J. M. Simonin. Surface deflection measurement using structured light. 2009. 38

[64] S. Nazarian, M. Baker, and K. Crain. Use of seismic pavement analyzer in pavement evaluation. pages 1–8, 1995. 25

[65] T. Nishizawa, T. Fukuda, and S. Matsuno. A refined model of doweled joints for concrete pavement using fem analysis. proceedings , 4th international conference on concrete pavement design and rehabilitation , purdue university, april 18-20, 1989, 1989. 24

[66] T. Nishizawa, M. Koyanagawa, Y. Takeuchi, and M. Kimura. Study on mechanical behavior of dowel bar in transverse joint of concrete pavement. In *Proceedings of the 7th International Conference on Concrete Pavements, Orlando, FL*, 2001. 13

[67] H. J. Oh, S.-M. Kim, W. Chung, Y. H. Lee, and Y. K. Cho. Effect of joint type on rigid airfield pavement behavior. 18(5):1389–1396, 2014-06. 14

[68] J. Paquet. The CEBTP curviameter - a new instrument for measuring highway pavement deflection. 1977. 32

[69] P. Pasternak. On a new method of an elastic foundation by means of two foundation constants. *Gosudarstvennoe Izdatelstvo Literaturi po Stroitelstuve i Arkhitekture*, 1954. 19, 56

[70] E. Reissner. A note on deflections of plates on a viscoelastic foundation. *J. Appl. Mech., ASME*, 25:144–145, 1958. 19, 56

[71] J. W. Rish, A. D. Adcock, C. Y. Tuan, S. L. Baker, H. W. Welker, and R. F. Johnson. Electro-optical approach to pavement deflection management. In *Nondestructive Evaluation of Aging Aircraft, Airports, Aerospace Hardware, and Materials*, volume 2455, pages 363–373. International Society for Optics and Photonics, 1995. 35

[72] F. Scrivner, G. Swift, and W. Moore. A new research tool for measuring pavement deflection. (129), 1966. 27

[73] T. Scullion. Using rolling deflectometer and ground penetrating radar technologies for full coverage testing of jointed concrete pavements, 2006. 113

[74] X. P. Shi, S. A. Tan, and T. F. Fwa. Rectangular thick plate with free edges on pasternak foundation. 120(5):971–988, 1994-05. 19

[75] S. N. Shoukry, M. Fahmy, J. Prucz, and G. William. Validation of 3dfe analysis of rigid pavement dynamic response to moving traffic and nonlinear temperature gradient effects. 7(1):16–24, 2007. ix, 23

[76] S. N. Shoukry, G. William, and M. Riad. Characteristics of concrete contact stresses in doweled transverse joints. 3(2):117–129, 2002-01. 13

[77] S. N. Shoukry, G. W. William, and M. Y. Riad. Evaluation of load transfer efficiency measurement, 2005. 41

[78] L. Shuo, T. F. Fwa, and K. H. Tan. Closed-form back-calculation of rigid-pavement parameters. 122(1):5–11, 1996-01. 43

[79] L. Shuo, T. F. Fwa, and K.-H. Tan. Parameters back-calculation for concrete pavement with two slab layers. 124(6):567–572, 1998-11. 43

[80] J.-M. Simonin, L.-M. Cottineau, V. Muzet, C. Heinkele, and Y. Guillard. Deflection measurement: the need of a continuous and full view approach. In *Bearing capacity of roads, railways and airfields: proceedings of the 8th International Conference on the Bearing Capacity of Roads, Railways and Airfields, Champaign, Illinois, USA, June 29-July 2, 2009*, pages 467–476. CRC Press, 2009. 41

[81] J. M. Simonin, D. Lièvre, S. Rasmussen, and G. Hildebrand. Assessment of the danish high speed deflectograph in france. In *Proc. 7th international conference on the bearing capacity of roads, railways and airfields, Trondheim Norway*, volume 10, 2005. 32

[82] A. Skar and P. N. Poulsen. 3-d cohesive finite element model for application in structural analysis of heavy duty composite pavements. 101:417–431, 2015. 21

[83] R. E. Smith and R. L. Lytton. Operating characteristics and user satisfaction of commercially available NDT equipment. 1007:1–10, 1985. 27

[84] E. B. Spangler and H. J. Schell. Noncontact, nondestructive determination of pavement deflection under a moving load. 1992. 34

[85] D. Steele, J. Hall, R. Stubstad, A. Peekna, and R. Walker. Development of a high-speed rolling wheel deflectometer. In *Pavement Evaluation Conference, 2002, Roanoke, Virginia, USA*, 2002. xi, 36, 37

[86] A. M. Tabatabaie and E. J. Barenberg. Finite-element analysis of jointed or cracked concrete pavements. (671), 1978. 13

[87] W. Uddin, R. M. Hackett, A. Joseph, Z. Pan, and A. B. Crawley. Three-dimensional finite-element analysis of jointed concrete pavement with discontinuities. 1482:26–32, 1995. 21

[88] P. Ullidtz. Triangulation of pavement deflections using more than four sensors, 2013-12-03. 41

[89] F. Van Cauwelaert. *Pavement Design and Evaluation: The Required Mathematics and Applications*. 2004. 63, 65

[90] T. S. Vepa and K. P. George. Deflection response models for cracked rigid pavements. 123(5):377–384, 1997-09. 21

[91] H. Vialletel and others. Le deflectographe flash. (208), 1997. 30

[92] V. Z. Vlasov. Beams, plates and shells on elastic foundation. *Israel Program for Scientific Translation*, 1966. 56

[93] A. Wadkar, Y. Mehta, D. Cleary, E. Guo, L. Musumeci, A. Zapata, and W. Kettleson. Load-transfer efficiencies of rigid airfield pavement joints based on stresses and deflections. 23(8):1171–1180, 2011-08. 42

[94] J. C. Walraven. Fundamental analysis of aggregate interlock. 107(11):2245–2270, 1981. 10, 11

[95] H. Westergaard. Spacing of dowels. In *Highway Research Board Proceedings*, volume 8, 1929. 12

[96] H. Westergaard. New formulas for stress in concrete pavements of airfields. *American Society of Civil Engineers Transactions*, 1948. 19

[97] H. M. WESTERGAARD. Computation of stresses in concrete roads. In *Highway Research Board Proceedings*, volume 5, 1926. 19

[98] H. M. Westergaard. Bearing pressures and cracks. *Trans AIME, J. Appl. Mech.*, 6:49–53, 1939. 19

[99] E. J. Yoder and M. W. Witczak. *Principles of pavement design*. John Wiley & Sons, 1991. 3

[100] X. Yu and X. Wu. Joint load transfer efficiency of rigid pavement considering dynamic effects under a single moving load. In *Information Engineering and Computer Science (ICIECS), 2010 2nd International Conference on*, pages 1–4. IEEE, 2010. 42

[101] Y.-c. Zhang and L.-l. Gao. Joint load-transfer prediction model considering dowel-bar position deviation in rigid pavements. 9(3):20–26, 2015. 14

[102] Z. Zhang, K. Gaspard, and M. A. Elseifi. Evaluating pavement management treatment selection utilising continuous deflection measurements in flexible pavements. 17(5):414–422, 2016-05-27. 24

Appendix A

Analytical solution for loaded slabs

The solution for loaded slab is represented by $w(x,y)+A(s)w_a(x,y)+B(s)w_b(x,y)$, where two constants(not literally but mathematically) out of 4 constants is obtained by solving the system at $x = c\ \forall y$. The solution of the loaded slab is put together in equation A.1. This equation forms the part of the solution on the loaded side forming the joint. This expression is then integrated over s from 0 to ∞ and then over x and y respectively in order to integrate the pressure load dimensions.

$$A(s)w_a(x,y) + B(s)w_b(x,y) = \frac{AA\left(-\frac{BB}{CC} + DD + \frac{EE}{FF}\right)\sin\left(\frac{x\beta}{l}\right)}{GG} + \frac{HH\left(\frac{JJ\left(\frac{K1}{L1} - \frac{K2}{L2}\right)\sec^5\left(\frac{sy}{l}\right)}{MM} + \frac{NN}{LL} - \frac{OO}{PP} - \frac{QQ}{RR}\right)}{SS} \tag{A.1}$$

$$AA = e^{\frac{x\alpha}{l}} p \cos\left(\frac{sy}{l}\right) \sin\left(\frac{bs}{l}\right) \tag{A.2}$$

$$CC = 2.\alpha\beta \cos\left(\frac{c\beta}{l}\right) + \left(1.\nu s^2 - 1.\alpha^2 + 1.\beta^2\right) \sin\left(\frac{c\beta}{l}\right) \tag{A.3}$$

$$GG = d^2 \left(1 - g^2\right)^{0.5} k\pi s \left(s^4 + 2.gs^2 + 1.\right) \alpha\beta^2 \tag{A.4}$$

$$SS = \left(1 - g^2\right)^{0.5} k\pi s \tag{A.5}$$

$$HH = e^{\frac{x\alpha}{l}} p \cos\left(\frac{sy}{l}\right) \cos\left(\frac{x\beta}{l}\right) \sin\left(\frac{bs}{l}\right) \tag{A.6}$$

$$L1 = \left(1. - 1.g^2\right)^{2.5} \tag{A.7}$$

$$L2 = \left(1. - 1.g^2\right)^{2.5} \tag{A.8}$$

$$LL = d\left(0.5s^4 + 1.gs^2 + 0.5\right) \tag{A.9}$$

$$PP = d\left(s^4 + 2.gs^2 + 1.\right) \alpha\beta \tag{A.10}$$

$$RR = d\left(s^4 + 2.gs^2 + 1.\right) \alpha\beta \left(\left(-1.\nu s^2 + 1.\alpha^2 - 1.\beta^2\right) \sin\left(\frac{c\beta}{l}\right) - 2.\alpha\beta \cos\left(\frac{c\beta}{l}\right)\right) \tag{A.11}$$

$$BB = -0.5de^{\frac{-1.a\alpha-4.c\alpha}{l}}\beta\sin\left(\frac{c\beta}{l}\right)\left(\left(1.\nu s^2-1.\alpha^2+1.\beta^2\right)\cos\left(\frac{c\beta}{l}\right)\right.$$
$$\left.+2.\alpha\beta\sin\left(\frac{c\beta}{l}\right)\right)\left(1.e^{\frac{2.a\alpha+2.c\alpha}{l}}\nu\sin\left(\frac{(c-1.a)\beta}{l}\right)s^4-1.e^{\frac{2.c\alpha}{l}}\nu\sin\left(\frac{(a+c)\beta}{l}\right)s^4\right.$$
$$-1.e^{\frac{2.(a+c)\alpha}{l}}\alpha^2\sin\left(\frac{(c-1.a)\beta}{l}\right)s^2+1.e^{\frac{2.(a+c)\alpha}{l}}\beta^2\sin\left(\frac{(c-1.a)\beta}{l}\right)s^2$$
$$+1.e^{\frac{2.a\alpha+2.c\alpha}{l}}g\nu\sin\left(\frac{(c-1.a)\beta}{l}\right)s^2+1.e^{\frac{2.c\alpha}{l}}\alpha^2\sin\left(\frac{(a+c)\beta}{l}\right)s^2$$
$$-1.e^{\frac{2.c\alpha}{l}}\beta^2\sin\left(\frac{(a+c)\beta}{l}\right)s^2-1.e^{\frac{2.c\alpha}{l}}g\nu\sin\left(\frac{(a+c)\beta}{l}\right)s^2$$
$$+\left(1.e^{\frac{2.a\alpha+2.c\alpha}{l}}\sqrt{1.-1.g^2}\nu s^2\right.$$
$$\left.+e^{\frac{2.(a+c)\alpha}{l}}\left(2.\alpha\beta s^2-1.\sqrt{1.-1.g^2}\alpha^2+1.\sqrt{1.-1.g^2}\beta^2+2.g\alpha\beta\right)\right)\cos\left(\frac{(c-1.a)\beta}{l}\right)$$
$$+e^{\frac{2.c\alpha}{l}}\left(-1.\sqrt{1.-1.g^2}\nu s^2-2.\alpha\beta s^2+1.\sqrt{1.-1.g^2}\alpha^2-1.\sqrt{1.-1.g^2}\beta^2\right.$$
$$\left.-2.g\alpha\beta\right)\cos\left(\frac{(a+c)\beta}{l}\right)-1.e^{\frac{2.(a+c)\alpha}{l}}g\alpha^2\sin\left(\frac{(c-1.a)\beta}{l}\right)$$
$$+1.e^{\frac{2.(a+c)\alpha}{l}}g\beta^2\sin\left(\frac{(c-1.a)\beta}{l}\right)-2.e^{\frac{2.(a+c)\alpha}{l}}\sqrt{1.-1.g^2}\alpha\beta\sin\left(\frac{(c-1.a)\beta}{l}\right)$$
$$+1.e^{\frac{2.c\alpha}{l}}g\alpha^2\sin\left(\frac{(a+c)\beta}{l}\right)-1.e^{\frac{2.c\alpha}{l}}g\beta^2\sin\left(\frac{(a+c)\beta}{l}\right)$$
$$\left.+2.e^{\frac{2.c\alpha}{l}}\sqrt{1.-1.g^2}\alpha\beta\sin\left(\frac{(a+c)\beta}{l}\right)\right) \tag{A.12}$$

$$DD = 0.5de^{-\frac{2c\alpha}{l}}\beta\left(1.e^{-\frac{1.a\alpha}{l}}\left(\left(-1.\nu s^2+1.\alpha^2-1.\beta^2\right)\cos\left(\frac{c\beta}{l}\right)\right.\right. \tag{A.13}$$
$$\left.\left.-2.\alpha\beta\sin\left(\frac{c\beta}{l}\right)\right)\left(1.de^{\frac{2.a\alpha}{l}}\sin\left(\frac{(c-1.a)\beta}{l}\right)s^2-1.e^{\frac{2.a\alpha}{l}}\sin\left(\frac{(c-1.a)\beta}{l}\right)s^2\right.$$
$$-1.d\sin\left(\frac{(a+c)\beta}{l}\right)s^2+1.\sin\left(\frac{(a+c)\beta}{l}\right)s^2$$
$$+1.(1.d-1.)e^{\frac{2.a\alpha}{l}}\sqrt{1.-1.g^2}\cos\left(\frac{(c-1.a)\beta}{l}\right)$$
$$-1.(1.d-1.)\sqrt{1.-1.g^2}\cos\left(\frac{(a+c)\beta}{l}\right)+1.de^{\frac{2.a\alpha}{l}}g\sin\left(\frac{(c-1.a)\beta}{l}\right)$$
$$\left.-1.e^{\frac{2.a\alpha}{l}}g\sin\left(\frac{(c-1.a)\beta}{l}\right)-1.dg\sin\left(\frac{(a+c)\beta}{l}\right)+1.g\sin\left(\frac{(a+c)\beta}{l}\right)\right)$$
$$+1.de^{\frac{c\alpha}{l}}\cos\left(\frac{c\beta}{l}\right)\left(1.e^{\frac{(a-1.c)\alpha}{l}}\nu\left(\sqrt{1.-1.g^2}\cos\left(\frac{(c-1.a)\beta}{l}\right)+\left(s^2+g\right)\sin\left(\frac{(c-1.a)\beta}{l}\right)\right)s^2\right.$$
$$-1.e^{-\frac{1.(a+c)\alpha}{l}}\nu\left(\sqrt{1.-1.g^2}\cos\left(\frac{(a+c)\beta}{l}\right)+\left(s^2+g\right)\sin\left(\frac{(a+c)\beta}{l}\right)\right)s^2$$
$$-1.e^{-\frac{2.c\alpha}{l}}\left(e^{\frac{(a+c)\alpha}{l}}\left(\sqrt{1.-1.g^2}\alpha^2-2.\left(s^2+g\right)\beta\alpha-1.\sqrt{1.-1.g^2}\beta^2\right)\cos\left(\frac{(c-1.a)\beta}{l}\right)-1.e^{\frac{(c-1.a)\alpha}{l}}\left(\sqrt{}\right.\right.$$

$$EE = de^{-\frac{3.c\alpha}{l}}\beta\sec\left(\frac{c\beta}{l}\right)\left(\left(1.\nu s^2 - 1.\alpha^2 + 1.\beta^2\right)\cos\left(\frac{c\beta}{l}\right)\right. \tag{A.14}$$

$$\left. + 2.\alpha\beta\sin\left(\frac{c\beta}{l}\right)\right)\left(0.020532e^{\frac{-1.a\alpha-1.c\alpha}{l}}\left(2.\alpha\beta\cos\left(\frac{c\beta}{l}\right)\right.\right.$$

$$\left.\left.+\left(1.\nu s^2 - 1.\alpha^2 + 1.\beta^2\right)\sin\left(\frac{c\beta}{l}\right)\right)\left(1.e^{\frac{2.c\alpha}{l}}\alpha\left(\alpha\left((\nu - 2.)s^2 + \alpha^2 - 3.\beta^2 - 2.g\right)\cos\left(\frac{c\beta}{l}\right) + \beta\left((2. - 1.\nu)s^2\right.\right.\right.\right.$$

$$\left.\left.\left.\left. - 1.5\left((0.333333\nu - 0.666667)s^2 + 1.\alpha^2 - 0.333333\beta^2 - 0.666667g\right)\left(e^{\frac{2.c\alpha}{l}}\alpha\beta\sin\left(\frac{c\beta}{l}\right)\left(-2.de^{\frac{2.a\alpha}{l}}\sin\left(\right.\right.\right.\right.\right.\right.\right.$$

$$\left.\left.\left.\left.\left.\left.\left. - 0.020532e^{\frac{2.c\alpha}{l}}\left(-3.\left((0.333333\nu - 0.666667)s^2 + 1.\alpha^2 - 0.333333\beta^2 - 0.666667g\right)\sin\left(\frac{c\beta}{l}\right)\left(\left(0.5\nu s^2 -\right.\right.\right.\right.\right.\right.\right.\right.$$

$$\left.\left.\left.\left.\left.\left.\left. - 1.\alpha\left(d\beta\left((2. - 1.\nu)s^2 - 3.\alpha^2 + 1.\beta^2 + 2.g\right)\cos^2\left(\frac{c\beta}{l}\right) + \beta\left((2. - 1.\nu)s^2 - 3.\alpha^2 + 1.\beta^2 + 2.g\right)\sin^2\left(\frac{c\beta}{l}\right) + \right.\right.\right.\right.\right.\right.\right.\right.$$

$$\left.\left.\left.\left.\left.\left.\left. - 1.e^{-\frac{1.(a+c)\alpha}{l}}\nu\left(\sqrt{1. - 1.g^2}\cos\left(\frac{(a+c)\beta}{l}\right) + \left(s^2 + g\right)\sin\left(\frac{(a+c)\beta}{l}\right)\right)s^2\right.\right.\right.\right.\right.\right.\right.$$

$$\left.\left.\left.\left.\left.\left.\left. - 1.e^{-\frac{2.c\alpha}{l}}\left(e^{\frac{(a+c)\alpha}{l}}\left(\sqrt{1. - 1.g^2}\alpha^2 - 2.\left(s^2 + g\right)\beta\alpha - 1.\sqrt{1. - 1.g^2}\beta^2\right)\cos\left(\frac{(c - 1.a)\beta}{l}\right) - 1.e^{\frac{(c-1.a)\alpha}{l}}\left(\sqrt{\right.\right.\right.\right.\right.\right.\right.\right.$$

$$FF = \left(\left(-1.\nu s^2 + 1.\alpha^2 - 1.\beta^2\right)\sin\left(\frac{c\beta}{l}\right) - 2.\alpha\beta\cos\left(\frac{c\beta}{l}\right)\right)\left(-0.020532d\nu^2 s^4\right.$$

$$- 0.020532\nu^2 s^4 + 0.0410639d\nu s^4 + 0.0410639\nu s^4 + 0.0410639d\alpha^2 s^2$$

$$- 0.0821279d\nu\alpha^2 s^2 - 0.0821279\nu\alpha^2 s^2 + 0.0410639\alpha^2 s^2 + 0.0410639d\beta^2 s^2$$

$$+ 0.0410639\beta^2 s^2 + 0.0410639dg\nu s^2 + 0.0410639g\nu s^2$$

$$+ 1.1397529869543831\text{*^-18}\nu\alpha\beta\sin\left(\frac{2c\beta}{l}\right)s^2$$

$$+ 5.698764934771916\text{*^-19}\nu\alpha\beta\sin\left(\frac{4c\beta}{l}\right)s^2 + 0.020532d\alpha^4 + 0.020532\alpha^4$$

$$+ 0.020532d\beta^4 + 0.020532\beta^4 + 0.0410639dg\alpha^2 + 0.0410639g\alpha^2 + 0.0410639d\alpha^2\beta^2$$

$$+ 0.0410639\alpha^2\beta^2 + 0.0410639dg\beta^2 + 0.0410639g\beta^2$$

$$+ 5.204170427930421\text{*^-18}\alpha^4\cos\left(\frac{2c\beta}{l}\right)$$

$$+ \alpha^2\left((8.673617379884035\text{*^-19}d - 1.3010426069826053\text{*^-18})\alpha^2\right.$$

$$\left.+ (1.734723475976807\text{*^-18}d + 5.204170427930421\text{*^-18})\beta^2\right)\cos\left(\frac{4c\beta}{l}\right)$$

$$- 2.2795059739087663\text{*^-18}\alpha\beta^3\sin\left(\frac{2c\beta}{l}\right)$$

$$\left. - 1.1397529869543831\text{*^-18}\alpha\beta^3\sin\left(\frac{4c\beta}{l}\right)\right) \tag{A.15}$$

$$JJ = 0.5e^{-\frac{3.c\alpha}{l}}\left(1. - 1.g^2\right)^{2.5}\csc^5\left(\frac{bs}{l}\right)\sec^3\left(\frac{c\beta}{l}\right)\left(-1.\nu\sin\left(\frac{2c\beta}{l}\right)s^2 + 2.\alpha\beta\right.$$
$$+ 2.\alpha\beta\cos\left(\frac{2c\beta}{l}\right) + 5.551115123125783^{*\wedge}\text{-}17\alpha\beta\cos\left(\frac{4c\beta}{l}\right) + 1.\alpha^2\sin\left(\frac{2c\beta}{l}\right)$$
$$\left. - 1.\beta^2\sin\left(\frac{2c\beta}{l}\right)\right) \tag{A.16}$$

$$MM = d^2p^5\left(s^4 + 2.gs^2 + 1.\right)\alpha\beta^2\left(-0.020532d\nu^2s^4 - 0.020532\nu^2s^4 + 0.0410639d\nu s^4\right.$$
$$+ 0.0410639\nu s^4 + 0.0410639d\alpha^2s^2 - 0.0821279d\nu\alpha^2s^2 - 0.0821279\nu\alpha^2s^2$$
$$+ 0.0410639\alpha^2s^2 + 0.0410639d\beta^2s^2 + 0.0410639\beta^2s^2 + 0.0410639dg\nu s^2$$
$$+ 0.0410639g\nu s^2 + 1.1397529869543831^{*\wedge}\text{-}18\nu\alpha\beta\sin\left(\frac{2c\beta}{l}\right)s^2$$
$$+ 5.698764934771916^{*\wedge}\text{-}19\nu\alpha\beta\sin\left(\frac{4c\beta}{l}\right)s^2 + 0.020532d\alpha^4 + 0.020532\alpha^4$$
$$+ 0.020532d\beta^4 + 0.020532\beta^4 + 0.0410639dg\alpha^2 + 0.0410639g\alpha^2 + 0.0410639d\alpha^2\beta^2$$
$$+ 0.0410639\alpha^2\beta^2 + 0.0410639dg\beta^2 + 0.0410639g\beta^2$$
$$+ 5.204170427930421^{*\wedge}\text{-}18\alpha^4\cos\left(\frac{2c\beta}{l}\right)$$
$$+ \alpha^2\left((8.673617379884035^{*\wedge}\text{-}19d - 1.3010426069826053^{*\wedge}\text{-}18)\alpha^2\right.$$
$$\left. + (1.734723475976807^{*\wedge}\text{-}18d + 5.204170427930421^{*\wedge}\text{-}18)\beta^2\right)\cos\left(\frac{4c\beta}{l}\right)$$
$$- 2.2795059739087663^{*\wedge}\text{-}18\alpha\beta^3\sin\left(\frac{2c\beta}{l}\right)$$
$$\left. - 1.1397529869543831^{*\wedge}\text{-}18\alpha\beta^3\sin\left(\frac{4c\beta}{l}\right)\right)\left(\left(-1.\nu s^2 + 1.\alpha^2 - 1.\beta^2\right)\tan\left(\frac{c\beta}{l}\right)\right.$$
$$\left. - 2.\alpha\beta\right) \tag{A.17}$$

$$K1 = 0.020532de^{\frac{-1.a\alpha-1.c\alpha}{l}}p^5\beta\cos^5\left(\frac{sy}{l}\right)\sin^5\left(\frac{bs}{l}\right)\left(2.\alpha\beta\cos\left(\frac{c\beta}{l}\right)+\left(1.\nu s^2\right.\right. \tag{A.18}$$
$$\left.-1.\alpha^2+1.\beta^2\right)\sin\left(\frac{c\beta}{l}\right)\Bigg)\left(1.e^{\frac{2.c\alpha}{l}}\alpha\left(\alpha\left((\nu-2.)s^2+\alpha^2-3.\beta^2-2.g\right)\cos\left(\frac{c\beta}{l}\right)\right.\right.$$
$$\left.+\beta\left((2.\ -1.\nu)s^2-3.\alpha^2+\beta^2+2.g\right)\sin\left(\frac{c\beta}{l}\right)\right)\left(1.de^{\frac{2.a\alpha}{l}}\sin\left(\frac{(c-1.a)\beta}{l}\right)s^2\right.$$
$$-1.e^{\frac{2.a\alpha}{l}}\sin\left(\frac{(c-1.a)\beta}{l}\right)s^2-1.d\sin\left(\frac{(a+c)\beta}{l}\right)s^2+1.\sin\left(\frac{(a+c)\beta}{l}\right)s^2$$
$$+1.(1.d-1.)e^{\frac{2.a\alpha}{l}}\sqrt{1.\ -1.g^2}\cos\left(\frac{(c-1.a)\beta}{l}\right)$$
$$-1.(1.d-1.)\sqrt{1.\ -1.g^2}\cos\left(\frac{(a+c)\beta}{l}\right)+1.de^{\frac{2.a\alpha}{l}}g\sin\left(\frac{(c-1.a)\beta}{l}\right)$$
$$\left.-1.e^{\frac{2.a\alpha}{l}}g\sin\left(\frac{(c-1.a)\beta}{l}\right)-1.dg\sin\left(\frac{(a+c)\beta}{l}\right)+1.g\sin\left(\frac{(a+c)\beta}{l}\right)\right)$$
$$-1.5\left((0.333333\nu-0.666667)s^2+1.\alpha^2-0.333333\beta^2\right.$$
$$\left.-0.666667g\right)\left(e^{\frac{2.c\alpha}{l}}\alpha\beta\sin\left(\frac{c\beta}{l}\right)\left(-2.de^{\frac{2.a\alpha}{l}}\sin\left(\frac{(c-1.a)\beta}{l}\right)s^2+2.e^{\frac{2.a\alpha}{l}}\sin\left(\frac{(c-1.a)\beta}{l}\right)s^2+2.d\sin\right.\right.$$
$$\left.+\cos\left(\frac{c\beta}{l}\right)\left(1.e^{\frac{2.a\alpha+2.c\alpha}{l}}\nu\sin\left(\frac{(c-1.a)\beta}{l}\right)s^4-1.e^{\frac{2.c\alpha}{l}}\nu\sin\left(\frac{(a+c)\beta}{l}\right)s^4-1.de^{\frac{2.(a+c)\alpha}{l}}\alpha^2\sin\left(\frac{(c-1.\right.\right.\right.$$
$$\left.\left.\left.l\right.\right.\right.$$

$$K2 \tag{A.19}$$
$$= 0.020532de^{\frac{2.c\alpha}{l}}p^5\beta\cos^5\left(\frac{sy}{l}\right)\sin^5\left(\frac{bs}{l}\right)\left(-3.\left((0.333333\nu-0.666667)s^2+1.\alpha^2\right.\right.$$
$$\left.-0.333333\beta^2-0.666667g\right)\sin\left(\frac{c\beta}{l}\right)\left(\left(0.5\nu s^2-0.5\alpha^2+0.5\beta^2\right)\cos\left(\frac{c\beta}{l}\right)\right.$$
$$\left.+1.\alpha\beta\sin\left(\frac{c\beta}{l}\right)\right)-1.\alpha\left(d\beta\left((2.\ -1.\nu)s^2-3.\alpha^2+1.\beta^2+2.g\right)\cos^2\left(\frac{c\beta}{l}\right)\right.$$
$$\left.+\beta\left((2.\ -1.\nu)s^2-3.\alpha^2+1.\beta^2+2.g\right)\sin^2\left(\frac{c\beta}{l}\right)\right.$$
$$\left.+\alpha\left((0.5\nu d-1.d+0.5\nu-1.)s^2+0.5d\alpha^2+0.5\alpha^2-1.5d\beta^2-1.5\beta^2+(-1.d-1.)g\right)\sin\left(\frac{2c\beta}{l}\right)\right)\Bigg)\left(1.e^{\frac{(a-1.c}{l}}\right.$$
$$\left.+\left(s^2+g\right)\sin\left(\frac{(c-1.a)\beta}{l}\right)\right)s^2$$
$$-1.e^{-\frac{1.(a+c)\alpha}{l}}\nu\left(\sqrt{1.\ -1.g^2}\cos\left(\frac{(a+c)\beta}{l}\right)+\left(s^2+g\right)\sin\left(\frac{(a+c)\beta}{l}\right)\right)s^2$$
$$-1.e^{-\frac{2.c\alpha}{l}}\left(e^{\frac{(a+c)\alpha}{l}}\left(\sqrt{1.\ -1.g^2}\alpha^2-2.\left(s^2+g\right)\beta\alpha-1.\sqrt{1.\ -1.g^2}\beta^2\right)\cos\left(\frac{(c-1.a)\beta}{l}\right)\right.$$
$$-1.e^{\frac{(c-1.a)\alpha}{l}}\left(\sqrt{1.\ -1.g^2}\alpha^2-2.\left(s^2+g\right)\beta\alpha-1.\sqrt{1.\ -1.g^2}\beta^2\right)\cos\left(\frac{(a+c)\beta}{l}\right)$$
$$+\left(\left(\alpha^2-1.\beta^2\right)s^2+2.\sqrt{1.\ -1.g^2}\alpha\beta+g\left(\alpha^2-1.\beta^2\right)\right)\left(e^{\frac{(a+c)\alpha}{l}}\sin\left(\frac{(c-1.a)\beta}{l}\right)-1.e^{\frac{(c-1.a)\alpha}{l}}\sin\left(\frac{(a+c)\right.\right.$$
$$\left.\left.l\right.\right.$$

$$NN = 0.5e^{\frac{-1.a\alpha-2.c\alpha}{l}} \sec\left(\frac{c\beta}{l}\right)\left(-1.de^{\frac{2.a\alpha}{l}} \sin\left(\frac{(c-1.a)\beta}{l}\right)s^2\right.$$
$$+ 1.e^{\frac{2.a\alpha}{l}} \sin\left(\frac{(c-1.a)\beta}{l}\right)s^2 + 1.d\sin\left(\frac{(a+c)\beta}{l}\right)s^2 - 1.\sin\left(\frac{(a+c)\beta}{l}\right)s^2$$
$$- 1.(1.d-1.)e^{\frac{2.a\alpha}{l}}\sqrt{1.-1.g^2}\cos\left(\frac{(c-1.a)\beta}{l}\right)$$
$$+ 1.(1.d-1.)\sqrt{1.-1.g^2}\cos\left(\frac{(a+c)\beta}{l}\right) - 1.de^{\frac{2.a\alpha}{l}}g\sin\left(\frac{(c-1.a)\beta}{l}\right)$$
$$\left.+ 1.e^{\frac{2.a\alpha}{l}}g\sin\left(\frac{(c-1.a)\beta}{l}\right) + 1.dg\sin\left(\frac{(a+c)\beta}{l}\right) - 1.g\sin\left(\frac{(a+c)\beta}{l}\right)\right) \tag{A.20}$$

$$OO = 0.5e^{-\frac{2c\alpha}{l}}\left(1.e^{-\frac{1.a\alpha}{l}}\left(\left(-1.\nu s^2 + 1.\alpha^2 - 1.\beta^2\right)\cos\left(\frac{c\beta}{l}\right)\right.\right. \tag{A.21}$$
$$\left.\left.- 2.\alpha\beta\sin\left(\frac{c\beta}{l}\right)\right)\left(1.de^{\frac{2.a\alpha}{l}}\sin\left(\frac{(c-1.a)\beta}{l}\right)s^2 - 1.e^{\frac{2.a\alpha}{l}}\sin\left(\frac{(c-1.a)\beta}{l}\right)s^2\right.$$
$$- 1.d\sin\left(\frac{(a+c)\beta}{l}\right)s^2 + 1.\sin\left(\frac{(a+c)\beta}{l}\right)s^2$$
$$+ 1.(1.d-1.)e^{\frac{2.a\alpha}{l}}\sqrt{1.-1.g^2}\cos\left(\frac{(c-1.a)\beta}{l}\right)$$
$$- 1.(1.d-1.)\sqrt{1.-1.g^2}\cos\left(\frac{(a+c)\beta}{l}\right) + 1.de^{\frac{2.a\alpha}{l}}g\sin\left(\frac{(c-1.a)\beta}{l}\right)$$
$$\left.- 1.e^{\frac{2.a\alpha}{l}}g\sin\left(\frac{(c-1.a)\beta}{l}\right) - 1.dg\sin\left(\frac{(a+c)\beta}{l}\right) + 1.g\sin\left(\frac{(a+c)\beta}{l}\right)\right)$$
$$+1.de^{\frac{c\alpha}{l}}\cos\left(\frac{c\beta}{l}\right)\left(1.e^{\frac{(a-1.c)\alpha}{l}}\nu\left(\sqrt{1.-1.g^2}\cos\left(\frac{(c-1.a)\beta}{l}\right)+\left(s^2+g\right)\sin\left(\frac{(c-1.a)\beta}{l}\right)\right)s^2\right.$$
$$- 1.e^{-\frac{1.(a+c)\alpha}{l}}\nu\left(\sqrt{1.-1.g^2}\cos\left(\frac{(a+c)\beta}{l}\right) + \left(s^2+g\right)\sin\left(\frac{(a+c)\beta}{l}\right)\right)s^2$$
$$-1.e^{-\frac{2.c\alpha}{l}}\left(e^{\frac{(a+c)\alpha}{l}}\left(\sqrt{1.-1.g^2}\alpha^2 - 2.\left(s^2+g\right)\beta\alpha - 1.\sqrt{1.-1.g^2}\beta^2\right)\cos\left(\frac{(c-1.a)\beta}{l}\right) - 1.e^{\frac{(c-1.a)\alpha}{l}}\left(\sqrt{}\right.\right.$$

$$QQ = 0.5e^{\frac{-1.a\alpha-4.c\alpha}{l}} \sin\left(\frac{c\beta}{l}\right)\left(-1.e^{\frac{2.a\alpha+2.c\alpha}{l}}\nu\sin\left(\frac{(c-1.a)\beta}{l}\right)s^4 + 1.e^{\frac{2.c\alpha}{l}}\nu\sin\left(\frac{(a+c)\beta}{l}\right)s^4 + 1.e^{\frac{2.(a+c)\alpha}{l}}\alpha^2\sin\left(\frac{(c-1.a)\beta}{l}\right)s^2 - 1.e^{\frac{2.(a+c)\alpha}{l}}\beta^2\sin\left(\frac{(c-1.a)\beta}{l}\right)s^2 - 1.e^{\frac{2.a\alpha+2.c\alpha}{l}}g\nu\sin\left(\frac{(c-1.a)\beta}{l}\right)s^2 - 1.e^{\frac{2.c\alpha}{l}}\alpha^2\sin\left(\frac{(a+c)\beta}{l}\right)s^2 + 1.e^{\frac{2.c\alpha}{l}}\beta^2\sin\left(\frac{(a+c)\beta}{l}\right)s^2 + 1.e^{\frac{2.c\alpha}{l}}g\nu\sin\left(\frac{(a+c)\beta}{l}\right)s^2 + \left(e^{\frac{2.(a+c)\alpha}{l}}\left(-2.\alpha\beta s^2 + 1.\sqrt{1.-1.g^2}\alpha^2 - 1.\sqrt{1.-1.g^2}\beta^2 - 2.g\alpha\beta\right) - 1.e^{\frac{2.a\alpha+2.c\alpha}{l}}\sqrt{1.-1.g^2}\nu s^2\right)\cos\left(\frac{(c-1.a)\beta}{l}\right) + e^{\frac{2.c\alpha}{l}}\left(1.\sqrt{1.-1.g^2}\nu s^2 + 2.\alpha\beta s^2 - 1.\sqrt{1.-1.g^2}\alpha^2 + 1.\sqrt{1.-1.g^2}\beta^2 + 2.g\alpha\beta\right)\cos\left(\frac{(a+c)\beta}{l}\right) + 1.e^{\frac{2.(a+c)\alpha}{l}}g\alpha^2\sin\left(\frac{(c-1.a)\beta}{l}\right) - 1.e^{\frac{2.(a+c)\alpha}{l}}g\beta^2\sin\left(\frac{(c-1.a)\beta}{l}\right) + 2.e^{\frac{2.(a+c)\alpha}{l}}\sqrt{1.-1.g^2}\alpha\beta\sin\left(\frac{(c-1.a)\beta}{l}\right) - 1.e^{\frac{2.c\alpha}{l}}g\alpha^2\sin\left(\frac{(a+c)\beta}{l}\right) + 1.e^{\frac{2.c\alpha}{l}}g\beta^2\sin\left(\frac{(a+c)\beta}{l}\right) - 2.e^{\frac{2.c\alpha}{l}}\sqrt{1.-1.g^2}\alpha\beta\sin\left(\frac{(a+c)\beta}{l}\right)\right)\left(2.\alpha\beta\cos\left(\frac{c\beta}{l}\right) + \sin\left(\frac{c\beta}{l}\right)\left(-1.\nu s^2 + 1.\alpha^2 - 1.\beta^2 + 2.2204460492503136^{*\wedge}\text{-}16\alpha\beta\tan\left(\frac{c\beta}{l}\right)\right)\right) \tag{A.22}$$

Appendix B

Analytical solution for unloaded slab next to a loaded slab

The solution for unloaded slab is represented by $w(x,y) + C(s)w_c(x,y) + D(s)w_d(x,y)$, where two constants(not literally but mathematically) out of 4 constants is obtained by solving the system at $x = c\ \forall y$. The solution of the unloaded slab is put together in equation B.1. This equation forms the part of the solution on the unloaded slab forming the joint. This expression is then integrated over s from 0 to ∞ and then over x and y respectively in order to integrate the pressure load dimensions.

$$\boxed{C(s)w_c(x,y) + D(s)w_d(x,y) = -\frac{N1}{D1} + \frac{e^{-\frac{x\alpha}{l}} p \cos\left(\frac{sy}{l}\right) \sin\left(\frac{bs}{l}\right)}{\left(1-g^2\right)^{0.5} k\pi s} (N2) \sin\left(\frac{x\beta}{l}\right) + N3} \tag{B.1}$$

$$N1 = A1\left(B1\left((C1)\left((C1)\left(-(DD1)(DD2)\right) - 1.(E1-E2)(FF - 1.(G1)(G2+G3))\right)\right.\right.$$
$$\left.\left. - 1.\left((G4)\left(\frac{H1(H2)}{H3} + H4\right) - 1.(J123)\left(\frac{J4(J5)}{J6} - \frac{J7}{J8}\right)\right)\left(K1 + K2 + \frac{K3}{K4}\right)\right)\right) \tag{B.2}$$

$$\boxed{N2 = \frac{N21}{D21} - \frac{1.(-Q1+Q2+Q3)}{Q4}} \tag{B.3}$$

$$Q1 = \frac{0.31831 e^{\frac{(a-1.c)\alpha}{l}} \nu ps \cos\left(\frac{sy}{l}\right) \sin\left(\frac{bs}{l}\right)\left(\sqrt{1. - 1.g^2}\cos\left(\frac{(c-1.a)\beta}{l}\right) + (s^2+g)\sin\left(\frac{(c-1.a)\beta}{l}\right)\right)}{\left(1. - 1.g^2\right)^{0.5} kl^2\left(s^4 + 2.gs^2 + 1.\right)} \tag{B.4}$$

$$Q2 = \frac{0.31831 e^{-\frac{1.(a+c)\alpha}{l}} \nu p s \cos\left(\frac{sy}{l}\right) \sin\left(\frac{bs}{l}\right) \left(\sqrt{1.-1.g^2}\cos\left(\frac{(a+c)\beta}{l}\right) + (s^2+g)\sin\left(\frac{(a+c)\beta}{l}\right)\right)}{(1.-1.g^2)^{0.5} k l^2 \left(s^4+2.gs^2+1.\right)} \tag{B.5}$$

$$\begin{aligned} Q3 = \frac{0.31831 e^{-\frac{2.c\alpha}{l}} p \cos\left(\frac{sy}{l}\right) \sin\left(\frac{bs}{l}\right)}{(1.-1.g^2)^{0.5} k l^2 s \left(s^4+2.gs^2+1.\right)} \Bigg(& e^{\frac{(a+c)\alpha}{l}} \left(\sqrt{1.-1.g^2}\alpha^2 - 2.\left(s^2+g\right)\beta\alpha \right. \\ & \left. - 1.\sqrt{1.-1.g^2}\beta^2\right)\cos\left(\frac{(c-1.a)\beta}{l}\right) \\ & - 1. e^{\frac{(c-1.a)\alpha}{l}} \left(\sqrt{1.-1.g^2}\alpha^2 - 2.\left(s^2+g\right)\beta\alpha - 1.\sqrt{1.-1.g^2}\beta^2\right)\cos\left(\frac{(a+c)\beta}{l}\right) \\ & + \left(\left(\alpha^2-1.\beta^2\right)s^2 + 2.\sqrt{1.-1.g^2}\alpha\beta + g\left(\alpha^2-1.\beta^2\right)\right)\left(e^{\frac{(a+c)\alpha}{l}}\sin\left(\frac{(c-1.a)\beta}{l}\right)\right. \\ & \left. - 1. e^{\frac{(c-1.a)\alpha}{l}}\sin\left(\frac{(a+c)\beta}{l}\right)\right)\Bigg) \end{aligned} \tag{B.6}$$

$$\begin{aligned} N21 = P1 \Bigg(& (P2)\Bigg((P3)\left(-1.(P4)(P5+P6)\right) \\ & - 1.(P7-P8)\left(\frac{P9\,(P10)}{(1.-1.g^2)^{0.5} ks} - 1.(P12)(P13+P14)\right)\Bigg) \\ & - 1.\left((P15)(P16+P17) - 1.(P18)(P19-P20)\right)(P21+P22+P23)\Bigg) \end{aligned} \tag{B.7}$$

$$\begin{aligned} P1 = 1.\Bigg(& -1.\nu p \cos\left(\frac{sy}{l}\right)\cos\left(\frac{c\beta}{l}\right)\sin\left(\frac{bs}{l}\right)s^2 + 1.p\alpha^2\cos\left(\frac{sy}{l}\right)\cos\left(\frac{c\beta}{l}\right)\sin\left(\frac{bs}{l}\right) \\ & - 1.p\beta^2\cos\left(\frac{sy}{l}\right)\cos\left(\frac{c\beta}{l}\right)\sin\left(\frac{bs}{l}\right) + 2.p\alpha\beta\cos\left(\frac{sy}{l}\right)\sin\left(\frac{bs}{l}\right)\sin\left(\frac{c\beta}{l}\right)\Bigg) \end{aligned} \tag{B.8}$$

$$\begin{aligned} P2 = & \frac{0.31831 e^{-\frac{1.c\alpha}{l}} p \cos\left(\frac{sy}{l}\right)\sin\left(\frac{bs}{l}\right)\sin\left(\frac{c\beta}{l}\right)\alpha^2}{(1.-1.g^2)^{0.5} k l^2 s} \\ & - \frac{0.63662 e^{-\frac{1.c\alpha}{l}} p\beta \cos\left(\frac{sy}{l}\right)\cos\left(\frac{c\beta}{l}\right)\sin\left(\frac{bs}{l}\right)\alpha}{(1.-1.g^2)^{0.5} k l^2 s} \\ & - \frac{0.31831 e^{-\frac{1.c\alpha}{l}} p\beta^2 \cos\left(\frac{sy}{l}\right)\sin\left(\frac{bs}{l}\right)\sin\left(\frac{c\beta}{l}\right)}{(1.-1.g^2)^{0.5} k l^2 s} \\ & - \frac{0.31831 e^{-\frac{1.c\alpha}{l}} \nu p s \cos\left(\frac{sy}{l}\right)\sin\left(\frac{bs}{l}\right)\sin\left(\frac{c\beta}{l}\right)}{(1.-1.g^2)^{0.5} k l^2} \end{aligned} \tag{B.9}$$

$$\begin{aligned} P3 = & \frac{0.202642 d e^{\frac{2.c\alpha}{l}} p^2 \alpha\beta \cos^2\left(\frac{sy}{l}\right)\cos^2\left(\frac{c\beta}{l}\right)\sin^2\left(\frac{bs}{l}\right)}{(1.-1.g^2)^{1.} k^2 l^2 s^2} \\ & + \frac{0.202642 d e^{\frac{2.c\alpha}{l}} p^2 \alpha\beta \cos^2\left(\frac{sy}{l}\right)\sin^2\left(\frac{c\beta}{l}\right)\sin^2\left(\frac{bs}{l}\right)}{(1.-1.g^2)^{1.} k^2 l^2 s^2} \end{aligned} \tag{B.10}$$

$$P4 = \frac{e^{\frac{c\alpha}{l}} p\alpha \left((\nu - 2.)s^2 + \alpha^2 - 3.\beta^2 - 2.g\right) \cos\left(\frac{sy}{l}\right) \cos\left(\frac{c\beta}{l}\right) \sin\left(\frac{bs}{l}\right)}{\left(1. - 1.g^2\right)^{0.5} kls} + \frac{e^{\frac{c\alpha}{l}} p\beta \left(-1.(\nu - 2.)s^2 - 3.\alpha^2 + \beta^2 + 2.g\right) \cos\left(\frac{sy}{l}\right) \sin\left(\frac{c\beta}{l}\right) \sin\left(\frac{bs}{l}\right)}{\left(1. - 1.g^2\right)^{0.5} kls} \tag{B.11}$$

$$P5 = \frac{0.31831 e^{-\frac{1.(a+c)\alpha}{l}} p \cos\left(\frac{sy}{l}\right) \sin\left(\frac{bs}{l}\right)}{\left(1. - 1.g^2\right)^{0.5} ks \left(s^4 + 2.gs^2 + 1.\right)} \left(-1.e^{\frac{2.a\alpha}{l}} \sqrt{1. - 1.g^2} \cos\left(\frac{(c - 1.a)\beta}{l}\right) + \sqrt{1. - 1.g^2} \cos\left(\frac{(a + c)\beta}{l}\right) + \left(s^2 + g\right) \left(\sin\left(\frac{(a + c)\beta}{l}\right) - 1.e^{\frac{2.a\alpha}{l}} \sin\left(\frac{(c - 1.a)\beta}{l}\right)\right)\right) \tag{B.12}$$

$$P6 = \frac{0.31831 dp \cos\left(\frac{sy}{l}\right) \sin\left(\frac{bs}{l}\right)}{\left(1. - 1.g^2\right)^{0.5} ks \left(s^4 + 2.gs^2 + 1.\right)} \left(e^{\frac{(a-1.c)\alpha}{l}} \left(\sqrt{1. - 1.g^2} \cos\left(\frac{(c - 1.a)\beta}{l}\right) + \left(s^2 + g\right) \sin\left(\frac{(c - 1.a)\beta}{l}\right)\right) - 1.e^{-\frac{1.(a+c)\alpha}{l}} \left(\sqrt{1. - 1.g^2} \cos\left(\frac{(a + c)\beta}{l}\right) + \left(s^2 + g\right) \sin\left(\frac{(a + c)\beta}{l}\right)\right)\right) \tag{B.13}$$

$$P7 = \frac{0.31831 de^{\frac{c\alpha}{l}} p \cos\left(\frac{sy}{l}\right) \cos\left(\frac{c\beta}{l}\right) \sin\left(\frac{bs}{l}\right)}{\left(1. - 1.g^2\right)^{0.5} ks} \left(-\frac{1.e^{\frac{c\alpha}{l}} p \cos\left(\frac{sy}{l}\right) \cos\left(\frac{c\beta}{l}\right) \sin\left(\frac{bs}{l}\right) \beta^3}{\left(1. - 1.g^2\right)^{0.5} kls} + \frac{3.e^{\frac{c\alpha}{l}} p\alpha^2 \cos\left(\frac{sy}{l}\right) \cos\left(\frac{c\beta}{l}\right) \sin\left(\frac{bs}{l}\right) \beta}{\left(1. - 1.g^2\right)^{0.5} kls} + \frac{e^{\frac{c\alpha}{l}} \nu ps \cos\left(\frac{sy}{l}\right) \cos\left(\frac{c\beta}{l}\right) \sin\left(\frac{bs}{l}\right) \beta}{\left(1. - 1.g^2\right)^{0.5} kl} - \frac{2.e^{\frac{c\alpha}{l}} ps \cos\left(\frac{sy}{l}\right) \cos\left(\frac{c\beta}{l}\right) \sin\left(\frac{bs}{l}\right) \beta}{\left(1. - 1.g^2\right)^{0.5} kl} - \frac{2.e^{\frac{c\alpha}{l}} gp \cos\left(\frac{sy}{l}\right) \cos\left(\frac{c\beta}{l}\right) \sin\left(\frac{bs}{l}\right) \beta}{\left(1. - 1.g^2\right)^{0.5} kls} + \frac{e^{\frac{c\alpha}{l}} p\alpha \left((\nu - 2.)s^2 + \alpha^2 - 3.\beta^2 - 2.g\right) \cos\left(\frac{sy}{l}\right) \sin\left(\frac{bs}{l}\right) \sin\left(\frac{c\beta}{l}\right)}{\left(1. - 1.g^2\right)^{0.5} kls}\right) \tag{B.14}$$

$$P8 = \frac{0.31831 de^{\frac{c\alpha}{l}} p \cos\left(\frac{sy}{l}\right) \sin\left(\frac{bs}{l}\right) \sin\left(\frac{c\beta}{l}\right)}{\left(1. - 1.g^2\right) k^2 s^2 l} \left(e^{\frac{c\alpha}{l}} p\alpha \left((\nu - 2.)s^2 + \alpha^2 - 3.\beta^2 - 2.g\right) \cos\left(\frac{sy}{l}\right) \cos\left(\frac{c\beta}{l}\right) \sin\left(\frac{bs}{l}\right) + e^{\frac{c\alpha}{l}} p\beta \left(-1.(\nu - 2.)s^2 - 3.\alpha^2 + \beta^2 + 2.g\right) \cos\left(\frac{sy}{l}\right) \sin\left(\frac{c\beta}{l}\right) \sin\left(\frac{bs}{l}\right)\right) \tag{B.15}$$

$$P9 = 0.31831 de^{\frac{c\alpha}{l}} p \cos\left(\frac{sy}{l}\right) \cos\left(\frac{c\beta}{l}\right) \sin\left(\frac{bs}{l}\right) \tag{B.16}$$

$$P10 = \tag{B.17}$$
$$-\frac{0.31831e^{\frac{(a-1.c)\alpha}{l}}\nu ps\cos\left(\frac{sy}{l}\right)\sin\left(\frac{bs}{l}\right)\left(\sqrt{1.-1.g^2}\cos\left(\frac{(c-1.a)\beta}{l}\right)+\left(s^2+g\right)\sin\left(\frac{(c-1.a)\beta}{l}\right)\right)}{\left(1.-1.g^2\right)^{0.5}kl^2\left(s^4+2.gs^2+1.\right)}$$
$$+\frac{0.31831e^{-\frac{1.(a+c)\alpha}{l}}\nu ps\cos\left(\frac{sy}{l}\right)\sin\left(\frac{bs}{l}\right)\left(\sqrt{1.-1.g^2}\cos\left(\frac{(a+c)\beta}{l}\right)+\left(s^2+g\right)\sin\left(\frac{(a+c)\beta}{l}\right)\right)}{\left(1.-1.g^2\right)^{0.5}kl^2\left(s^4+2.gs^2+1.\right)}$$
$$+\frac{0.31831e^{-\frac{2.c\alpha}{l}}p\cos\left(\frac{sy}{l}\right)\sin\left(\frac{bs}{l}\right)}{\left(1.-1.g^2\right)^{0.5}kl^2s\left(s^4+2.gs^2+1.\right)}\left(e^{\frac{(a+c)\alpha}{l}}\left(\sqrt{1.-1.g^2}\alpha^2-2.\left(s^2+g\right)\beta\alpha\right.\right.$$
$$\left.-1.\sqrt{1.-1.g^2}\beta^2\right)\cos\left(\frac{(c-1.a)\beta}{l}\right)$$
$$-1.e^{\frac{(c-1.a)\alpha}{l}}\left(\sqrt{1.-1.g^2}\alpha^2-2.\left(s^2+g\right)\beta\alpha-1.\sqrt{1.-1.g^2}\beta^2\right)\cos\left(\frac{(a+c)\beta}{l}\right)$$
$$+\left(\left(\alpha^2-1.\beta^2\right)s^2+2.\sqrt{1.-1.g^2}\alpha\beta\right.$$
$$\left.\left.+g\left(\alpha^2-1.\beta^2\right)\right)\left(e^{\frac{(a+c)\alpha}{l}}\sin\left(\frac{(c-1.a)\beta}{l}\right)-1.e^{\frac{(c-1.a)\alpha}{l}}\sin\left(\frac{(a+c)\beta}{l}\right)\right)\right)$$

$$P12 = \frac{0.31831e^{\frac{c\alpha}{l}}p\cos\left(\frac{sy}{l}\right)\cos\left(\frac{c\beta}{l}\right)\sin\left(\frac{bs}{l}\right)\alpha^2}{\left(1.-1.g^2\right)^{0.5}kl^2s}-\frac{0.63662e^{\frac{c\alpha}{l}}p\beta\cos\left(\frac{sy}{l}\right)\sin\left(\frac{bs}{l}\right)\sin\left(\frac{c\beta}{l}\right)\alpha}{\left(1.-1.g^2\right)^{0.5}kl^2s}$$
$$-\frac{0.31831e^{\frac{c\alpha}{l}}p\beta^2\cos\left(\frac{sy}{l}\right)\cos\left(\frac{c\beta}{l}\right)\sin\left(\frac{bs}{l}\right)}{\left(1.-1.g^2\right)^{0.5}kl^2s}-\frac{0.31831e^{\frac{c\alpha}{l}}\nu ps\cos\left(\frac{sy}{l}\right)\cos\left(\frac{c\beta}{l}\right)\sin\left(\frac{bs}{l}\right)}{\left(1.-1.g^2\right)^{0.5}kl^2} \tag{B.18}$$

$$P13 = \frac{0.31831e^{-\frac{1.(a+c)\alpha}{l}}p\cos\left(\frac{sy}{l}\right)\sin\left(\frac{bs}{l}\right)}{\left(1.-1.g^2\right)^{0.5}ks\left(s^4+2.gs^2+1.\right)}\left(-1.e^{\frac{2.a\alpha}{l}}\sqrt{1.-1.g^2}\cos\left(\frac{(c-1.a)\beta}{l}\right)\right.$$
$$+\sqrt{1.-1.g^2}\cos\left(\frac{(a+c)\beta}{l}\right) \tag{B.19}$$
$$\left.+\left(s^2+g\right)\left(\sin\left(\frac{(a+c)\beta}{l}\right)-1.e^{\frac{2.a\alpha}{l}}\sin\left(\frac{(c-1.a)\beta}{l}\right)\right)\right)$$

$$P14 = \frac{0.31831dp\cos\left(\frac{sy}{l}\right)\sin\left(\frac{bs}{l}\right)}{\left(1.-1.g^2\right)^{0.5}ks\left(s^4+2.gs^2+1.\right)}\left(e^{\frac{(a-1.c)\alpha}{l}}\left(\sqrt{1.-1.g^2}\cos\left(\frac{(c-1.a)\beta}{l}\right)\right.\right.$$
$$\left.+\left(s^2+g\right)\sin\left(\frac{(c-1.a)\beta}{l}\right)\right)$$
$$\left.-1.e^{-\frac{1.(a+c)\alpha}{l}}\left(\sqrt{1.-1.g^2}\cos\left(\frac{(a+c)\beta}{l}\right)+\left(s^2+g\right)\sin\left(\frac{(a+c)\beta}{l}\right)\right)\right) \tag{B.20}$$

$$P15 = \frac{0.202642de^{\frac{2.c\alpha}{l}}p^2\alpha\beta\cos^2\left(\frac{sy}{l}\right)\cos^2\left(\frac{c\beta}{l}\right)\sin^2\left(\frac{bs}{l}\right)}{\left(1.-1.g^2\right)^{1.}k^2l^2s^2}$$
$$+\frac{0.202642de^{\frac{2.c\alpha}{l}}p^2\alpha\beta\cos^2\left(\frac{sy}{l}\right)\sin^2\left(\frac{c\beta}{l}\right)\sin^2\left(\frac{bs}{l}\right)}{\left(1.-1.g^2\right)^{1.}k^2l^2s^2} \tag{B.21}$$

$$P16 = \frac{0.31831 d e^{\frac{c\alpha}{l}} p \cos\left(\frac{sy}{l}\right) \cos\left(\frac{c\beta}{l}\right) \sin\left(\frac{bs}{l}\right)}{\left(1. - 1.g^2\right)^{0.5} ks} \left(\frac{e^{-\frac{1.c\alpha}{l}} p \cos\left(\frac{sy}{l}\right) \cos\left(\frac{c\beta}{l}\right) \sin\left(\frac{bs}{l}\right) \beta^3}{\left(1. - 1.g^2\right)^{0.5} kls} - \frac{3. e^{-\frac{1.c\alpha}{l}} p\alpha^2 \cos\left(\frac{sy}{l}\right) \cos\left(\frac{c\beta}{l}\right) \sin\left(\frac{bs}{l}\right) \beta}{\left(1. - 1.g^2\right)^{0.5} kls} - \frac{1. e^{-\frac{1.c\alpha}{l}} \nu ps \cos\left(\frac{sy}{l}\right) \cos\left(\frac{c\beta}{l}\right) \sin\left(\frac{bs}{l}\right) \beta}{\left(1. - 1.g^2\right)^{0.5} kl} + \frac{2. e^{-\frac{1.c\alpha}{l}} ps \cos\left(\frac{sy}{l}\right) \cos\left(\frac{c\beta}{l}\right) \sin\left(\frac{bs}{l}\right) \beta}{\left(1. - 1.g^2\right)^{0.5} kl} + \frac{2. e^{-\frac{1.c\alpha}{l}} gp \cos\left(\frac{sy}{l}\right) \cos\left(\frac{c\beta}{l}\right) \sin\left(\frac{bs}{l}\right) \beta}{\left(1. - 1.g^2\right)^{0.5} kls} + \frac{e^{-\frac{1.c\alpha}{l}} p\alpha \left((\nu - 2.)s^2 + \alpha^2 - 3.\beta^2 - 2.g\right) \cos\left(\frac{sy}{l}\right) \sin\left(\frac{bs}{l}\right) \sin\left(\frac{c\beta}{l}\right)}{\left(1. - 1.g^2\right)^{0.5} kls} \right) \tag{B.22}$$

$$P17 = \frac{0.31831 e^{-\frac{1.c\alpha}{l}} p \cos\left(\frac{sy}{l}\right) \sin\left(\frac{bs}{l}\right) \sin\left(\frac{c\beta}{l}\right)}{\left(1. - 1.g^2\right) k^2 s^2 l} \left(e^{\frac{c\alpha}{l}} p\alpha \left((\nu - 2.)s^2 + \alpha^2 - 3.\beta^2 - 2.g\right) \cos\left(\frac{sy}{l}\right) \cos\left(\frac{c\beta}{l}\right) \sin\left(\frac{bs}{l}\right) + e^{\frac{c\alpha}{l}} p\beta \left(-1.(\nu - 2.)s^2 - 3.\alpha^2 + \beta^2 + 2.g\right) \cos\left(\frac{sy}{l}\right) \sin\left(\frac{c\beta}{l}\right) \sin\left(\frac{bs}{l}\right) \right) \tag{B.23}$$

$$P18 = \frac{0.31831 e^{-\frac{1.c\alpha}{l}} p \cos\left(\frac{sy}{l}\right) \sin\left(\frac{bs}{l}\right) \sin\left(\frac{c\beta}{l}\right)}{\left(1. - 1.g^2\right)^{0.5} ks} \left(\frac{0.31831 e^{\frac{c\alpha}{l}} p \cos\left(\frac{sy}{l}\right) \cos\left(\frac{c\beta}{l}\right) \sin\left(\frac{bs}{l}\right) \alpha^2}{\left(1. - 1.g^2\right)^{0.5} kl^2 s} - \frac{0.63662 e^{\frac{c\alpha}{l}} p\beta \cos\left(\frac{sy}{l}\right) \sin\left(\frac{bs}{l}\right) \sin\left(\frac{c\beta}{l}\right) \alpha}{\left(1. - 1.g^2\right)^{0.5} kl^2 s} - \frac{0.31831 e^{\frac{c\alpha}{l}} p\beta^2 \cos\left(\frac{sy}{l}\right) \cos\left(\frac{c\beta}{l}\right) \sin\left(\frac{bs}{l}\right)}{\left(1. - 1.g^2\right)^{0.5} kl^2 s} - \frac{0.31831 e^{\frac{c\alpha}{l}} \nu ps \cos\left(\frac{sy}{l}\right) \cos\left(\frac{c\beta}{l}\right) \sin\left(\frac{bs}{l}\right)}{\left(1. - 1.g^2\right)^{0.5} kl^2} \right) \tag{B.24}$$

$$P19 = \frac{0.31831 d e^{\frac{c\alpha}{l}} p \cos\left(\frac{sy}{l}\right) \cos\left(\frac{c\beta}{l}\right) \sin\left(\frac{bs}{l}\right)}{\left(1. - 1.g^2\right)^{0.5} ks} \left(-\frac{1. e^{\frac{c\alpha}{l}} p \cos\left(\frac{sy}{l}\right) \cos\left(\frac{c\beta}{l}\right) \sin\left(\frac{bs}{l}\right) \beta^3}{\left(1. - 1.g^2\right)^{0.5} kls} + \frac{3. e^{\frac{c\alpha}{l}} p\alpha^2 \cos\left(\frac{sy}{l}\right) \cos\left(\frac{c\beta}{l}\right) \sin\left(\frac{bs}{l}\right) \beta}{\left(1. - 1.g^2\right)^{0.5} kls} + \frac{e^{\frac{c\alpha}{l}} \nu ps \cos\left(\frac{sy}{l}\right) \cos\left(\frac{c\beta}{l}\right) \sin\left(\frac{bs}{l}\right) \beta}{\left(1. - 1.g^2\right)^{0.5} kl} - \frac{2. e^{\frac{c\alpha}{l}} ps \cos\left(\frac{sy}{l}\right) \cos\left(\frac{c\beta}{l}\right) \sin\left(\frac{bs}{l}\right) \beta}{\left(1. - 1.g^2\right)^{0.5} kl} - \frac{2. e^{\frac{c\alpha}{l}} gp \cos\left(\frac{sy}{l}\right) \cos\left(\frac{c\beta}{l}\right) \sin\left(\frac{bs}{l}\right) \beta}{\left(1. - 1.g^2\right)^{0.5} kls} + \frac{e^{\frac{c\alpha}{l}} p\alpha \left((\nu - 2.)s^2 + \alpha^2 - 3.\beta^2 - 2.g\right) \cos\left(\frac{sy}{l}\right) \sin\left(\frac{bs}{l}\right) \sin\left(\frac{c\beta}{l}\right)}{\left(1. - 1.g^2\right)^{0.5} kls} \right) \tag{B.25}$$

$$P20 = \frac{0.31831 d e^{\frac{c\alpha}{l}} p \cos\left(\frac{sy}{l}\right) \sin\left(\frac{bs}{l}\right) \sin\left(\frac{c\beta}{l}\right)}{\left(1.-1.g^2\right) k^2 s^2 l} \left(e^{\frac{c\alpha}{l}} p\alpha \left((\nu-2.)s^2+\alpha^2-3.\beta^2 - 2.g\right) \cos\left(\frac{sy}{l}\right) \cos\left(\frac{c\beta}{l}\right) \sin\left(\frac{bs}{l}\right) + e^{\frac{c\alpha}{l}} p\beta \left(-1.(\nu-2.)s^2-3.\alpha^2+\beta^2+2.g\right) \cos\left(\frac{sy}{l}\right) \sin\left(\frac{c\beta}{l}\right) \sin\left(\frac{bs}{l}\right)\right) \tag{B.26}$$

$$P21 = -\frac{0.31831 e^{\frac{(a-1.c)\alpha}{l}} \nu p s \cos\left(\frac{sy}{l}\right) \sin\left(\frac{bs}{l}\right) \left(\sqrt{1.-1.g^2} \cos\left(\frac{(c-1.a)\beta}{l}\right) + \left(s^2+g\right) \sin\left(\frac{(c-1.a)\beta}{l}\right)\right)}{\left(1.-1.g^2\right)^{0.5} k l^2 \left(s^4+2.gs^2+1.\right)} \tag{B.27}$$

$$P22 = \frac{0.31831 e^{-\frac{1.(a+c)\alpha}{l}} \nu p s \cos\left(\frac{sy}{l}\right) \sin\left(\frac{bs}{l}\right) \left(\sqrt{1.-1.g^2} \cos\left(\frac{(a+c)\beta}{l}\right) + \left(s^2+g\right) \sin\left(\frac{(a+c)\beta}{l}\right)\right)}{\left(1.-1.g^2\right)^{0.5} k l^2 \left(s^4+2.gs^2+1.\right)} \tag{B.28}$$

$$P23 = \frac{0.31831 e^{-\frac{2.c\alpha}{l}} p \cos\left(\frac{sy}{l}\right) \sin\left(\frac{bs}{l}\right)}{\left(1.-1.g^2\right)^{0.5} k l^2 s \left(s^4+2.gs^2+1.\right)} \left(e^{\frac{(a+c)\alpha}{l}} \left(\sqrt{1.-1.g^2}\alpha^2 - 2.\left(s^2+g\right)\beta\alpha - 1.\sqrt{1.-1.g^2}\beta^2\right) \cos\left(\frac{(c-1.a)\beta}{l}\right) - 1. e^{\frac{(c-1.a)\alpha}{l}} \left(\sqrt{1.-1.g^2}\alpha^2 - 2.\left(s^2+g\right)\beta\alpha - 1.\sqrt{1.-1.g^2}\beta^2\right) \cos\left(\frac{(a+c)\beta}{l}\right) + \left(\left(\alpha^2-1.\beta^2\right)s^2 + 2.\sqrt{1.-1.g^2}\alpha\beta + g\left(\alpha^2-1.\beta^2\right)\right) \left(e^{\frac{(a+c)\alpha}{l}} \sin\left(\frac{(c-1.a)\beta}{l}\right) - 1. e^{\frac{(c-1.a)\alpha}{l}} \sin\left(\frac{(a+c)\beta}{l}\right)\right)\right) \tag{B.29}$$

$$D21 = (R1)\left((R2)\left((R3)\left(R4+R5\right) - 1.\left(R6\right)\left(R7-R8\right)\right) - 1.\left(R9\right)\left(\left(R10\right)\left(R11+R12\right) - 1.\left(R13\right)\left(R14-R15\right)\right)\right) \tag{B.30}$$

$$R1 = -1.\nu p \cos\left(\frac{sy}{l}\right) \sin\left(\frac{bs}{l}\right) \sin\left(\frac{c\beta}{l}\right) s^2 - 2.p\alpha\beta \cos\left(\frac{sy}{l}\right) \cos\left(\frac{c\beta}{l}\right) \sin\left(\frac{bs}{l}\right) + 1.p\alpha^2 \cos\left(\frac{sy}{l}\right) \sin\left(\frac{bs}{l}\right) \sin\left(\frac{c\beta}{l}\right) - 1.p\beta^2 \cos\left(\frac{sy}{l}\right) \sin\left(\frac{bs}{l}\right) \sin\left(\frac{c\beta}{l}\right) \tag{B.31}$$

$$
\begin{aligned}
R2 = & \frac{0.31831 e^{-\frac{1.c\alpha}{l}} p \cos\left(\frac{sy}{l}\right) \sin\left(\frac{bs}{l}\right) \sin\left(\frac{c\beta}{l}\right) \alpha^2}{\left(1. - 1.g^2\right)^{0.5} kl^2 s} \\
& - \frac{0.63662 e^{-\frac{1.c\alpha}{l}} p\beta \cos\left(\frac{sy}{l}\right) \cos\left(\frac{c\beta}{l}\right) \sin\left(\frac{bs}{l}\right) \alpha}{\left(1. - 1.g^2\right)^{0.5} kl^2 s} \\
& - \frac{0.31831 e^{-\frac{1.c\alpha}{l}} p\beta^2 \cos\left(\frac{sy}{l}\right) \sin\left(\frac{bs}{l}\right) \sin\left(\frac{c\beta}{l}\right)}{\left(1. - 1.g^2\right)^{0.5} kl^2 s} \\
& - \frac{0.31831 e^{-\frac{1.c\alpha}{l}} \nu ps \cos\left(\frac{sy}{l}\right) \sin\left(\frac{bs}{l}\right) \sin\left(\frac{c\beta}{l}\right)}{\left(1. - 1.g^2\right)^{0.5} kl^2}
\end{aligned}
\tag{B.32}
$$

$$
\begin{aligned}
R3 = & \frac{0.202642 de^{\frac{2c\alpha}{l}} p^2 \alpha\beta \cos^2\left(\frac{sy}{l}\right) \cos^2\left(\frac{c\beta}{l}\right) \sin^2\left(\frac{bs}{l}\right)}{\left(1. - 1.g^2\right)^{1.} k^2 l^2 s^2} \\
& + \frac{0.202642 de^{\frac{2c\alpha}{l}} p^2 \alpha\beta \cos^2\left(\frac{sy}{l}\right) \sin^2\left(\frac{c\beta}{l}\right) \sin^2\left(\frac{bs}{l}\right)}{\left(1. - 1.g^2\right)^{1.} k^2 l^2 s^2}
\end{aligned}
\tag{B.33}
$$

$$
\begin{aligned}
R4 = & \frac{0.31831 de^{\frac{c\alpha}{l}} p \cos\left(\frac{sy}{l}\right) \cos\left(\frac{c\beta}{l}\right) \sin\left(\frac{bs}{l}\right)}{\left(1. - 1.g^2\right)^{0.5} ks} \left(\frac{e^{-\frac{1.c\alpha}{l}} p \cos\left(\frac{sy}{l}\right) \cos\left(\frac{c\beta}{l}\right) \sin\left(\frac{bs}{l}\right) \alpha^3}{\left(1. - 1.g^2\right)^{0.5} kls} \right. \\
& - \frac{3. e^{-\frac{1.c\alpha}{l}} p\beta^2 \cos\left(\frac{sy}{l}\right) \cos\left(\frac{c\beta}{l}\right) \sin\left(\frac{bs}{l}\right) \alpha}{\left(1. - 1.g^2\right)^{0.5} kls} + \frac{e^{-\frac{1.c\alpha}{l}} \nu ps \cos\left(\frac{sy}{l}\right) \cos\left(\frac{c\beta}{l}\right) \sin\left(\frac{bs}{l}\right) \alpha}{\left(1. - 1.g^2\right)^{0.5} kl} \\
& - \frac{2. e^{-\frac{1.c\alpha}{l}} ps \cos\left(\frac{sy}{l}\right) \cos\left(\frac{c\beta}{l}\right) \sin\left(\frac{bs}{l}\right) \alpha}{\left(1. - 1.g^2\right)^{0.5} kl} - \frac{2. e^{-\frac{1.c\alpha}{l}} gp \cos\left(\frac{sy}{l}\right) \cos\left(\frac{c\beta}{l}\right) \sin\left(\frac{bs}{l}\right) \alpha}{\left(1. - 1.g^2\right)^{0.5} kls} \\
& \left. - \frac{1. e^{-\frac{1.c\alpha}{l}} p\beta \left(-1.(\nu - 2.)s^2 - 3.\alpha^2 + \beta^2 + 2.g\right) \cos\left(\frac{sy}{l}\right) \sin\left(\frac{bs}{l}\right) \sin\left(\frac{c\beta}{l}\right)}{\left(1. - 1.g^2\right)^{0.5} kls} \right)
\end{aligned}
\tag{B.34}
$$

$$
\begin{aligned}
R5 = & \frac{0.31831 e^{-\frac{1.c\alpha}{l}} p \cos\left(\frac{sy}{l}\right) \cos\left(\frac{c\beta}{l}\right) \sin\left(\frac{bs}{l}\right)}{\left(1. - 1.g^2\right) k^2 s^2 l} \left(e^{\frac{c\alpha}{l}} p\alpha \left((\nu - 2.)s^2 + \alpha^2 - 3.\beta^2 \right.\right. \\
& \left. - 2.g\right) \cos\left(\frac{sy}{l}\right) \cos\left(\frac{c\beta}{l}\right) \sin\left(\frac{bs}{l}\right) \\
& \left. + e^{\frac{c\alpha}{l}} p\beta \left(-1.(\nu - 2.)s^2 - 3.\alpha^2 + \beta^2 + 2.g\right) \cos\left(\frac{sy}{l}\right) \sin\left(\frac{c\beta}{l}\right) \sin\left(\frac{bs}{l}\right) \right)
\end{aligned}
\tag{B.35}
$$

$$
\begin{aligned}
R6 = & \frac{0.31831 e^{-\frac{1.c\alpha}{l}} p \cos\left(\frac{sy}{l}\right) \cos\left(\frac{c\beta}{l}\right) \sin\left(\frac{bs}{l}\right)}{\left(1. - 1.g^2\right)^{0.5} ks} \left(\frac{0.31831 e^{\frac{c\alpha}{l}} p \cos\left(\frac{sy}{l}\right) \cos\left(\frac{c\beta}{l}\right) \sin\left(\frac{bs}{l}\right) \alpha^2}{\left(1. - 1.g^2\right)^{0.5} kl^2 s} \right. \\
& - \frac{0.63662 e^{\frac{c\alpha}{l}} p\beta \cos\left(\frac{sy}{l}\right) \sin\left(\frac{bs}{l}\right) \sin\left(\frac{c\beta}{l}\right) \alpha}{\left(1. - 1.g^2\right)^{0.5} kl^2 s} - \frac{0.31831 e^{\frac{c\alpha}{l}} p\beta^2 \cos\left(\frac{sy}{l}\right) \cos\left(\frac{c\beta}{l}\right) \sin\left(\frac{bs}{l}\right)}{\left(1. - 1.g^2\right)^{0.5} kl^2 s} \\
& \left. - \frac{0.31831 e^{\frac{c\alpha}{l}} \nu ps \cos\left(\frac{sy}{l}\right) \cos\left(\frac{c\beta}{l}\right) \sin\left(\frac{bs}{l}\right)}{\left(1. - 1.g^2\right)^{0.5} kl^2} \right)
\end{aligned}
\tag{B.36}
$$

$$R7 = \frac{0.31831 d e^{\frac{c\alpha}{l}} p \cos\left(\frac{sy}{l}\right) \cos\left(\frac{c\beta}{l}\right) \sin\left(\frac{bs}{l}\right)}{\left(1. - 1.g^2\right)^{0.5} ks} \left(- \frac{1.e^{\frac{c\alpha}{l}} p \cos\left(\frac{sy}{l}\right) \cos\left(\frac{c\beta}{l}\right) \sin\left(\frac{bs}{l}\right) \beta^3}{\left(1. - 1.g^2\right)^{0.5} kls} + \frac{3.e^{\frac{c\alpha}{l}} p\alpha^2 \cos\left(\frac{sy}{l}\right) \cos\left(\frac{c\beta}{l}\right) \sin\left(\frac{bs}{l}\right) \beta}{\left(1. - 1.g^2\right)^{0.5} kls} + \frac{e^{\frac{c\alpha}{l}} \nu ps \cos\left(\frac{sy}{l}\right) \cos\left(\frac{c\beta}{l}\right) \sin\left(\frac{bs}{l}\right) \beta}{\left(1. - 1.g^2\right)^{0.5} kl} - \frac{2.e^{\frac{c\alpha}{l}} ps \cos\left(\frac{sy}{l}\right) \cos\left(\frac{c\beta}{l}\right) \sin\left(\frac{bs}{l}\right) \beta}{\left(1. - 1.g^2\right)^{0.5} kl} - \frac{2.e^{\frac{c\alpha}{l}} gp \cos\left(\frac{sy}{l}\right) \cos\left(\frac{c\beta}{l}\right) \sin\left(\frac{bs}{l}\right) \beta}{\left(1. - 1.g^2\right)^{0.5} kls} + \frac{e^{\frac{c\alpha}{l}} p\alpha \left((\nu - 2.)s^2 + \alpha^2 - 3.\beta^2 - 2.g\right) \cos\left(\frac{sy}{l}\right) \sin\left(\frac{bs}{l}\right) \sin\left(\frac{c\beta}{l}\right)}{\left(1. - 1.g^2\right)^{0.5} kls} \right) \tag{B.37}$$

$$R8 = \frac{0.31831 d e^{\frac{c\alpha}{l}} p \cos\left(\frac{sy}{l}\right) \sin\left(\frac{bs}{l}\right) \sin\left(\frac{c\beta}{l}\right)}{\left(1. - 1.g^2\right) k^2 s^2 l} \left(e^{\frac{c\alpha}{l}} p\alpha \left((\nu - 2.)s^2 + \alpha^2 - 3.\beta^2 - 2.g\right) \cos\left(\frac{sy}{l}\right) \cos\left(\frac{c\beta}{l}\right) \sin\left(\frac{bs}{l}\right) + e^{\frac{c\alpha}{l}} p\beta \left(-1.(\nu - 2.)s^2 - 3.\alpha^2 + \beta^2 + 2.g\right) \cos\left(\frac{sy}{l}\right) \sin\left(\frac{c\beta}{l}\right) \sin\left(\frac{bs}{l}\right) \right) \tag{B.38}$$

$$R9 = \frac{0.31831 e^{-\frac{1.c\alpha}{l}} p \cos\left(\frac{sy}{l}\right) \cos\left(\frac{c\beta}{l}\right) \sin\left(\frac{bs}{l}\right) \alpha^2}{\left(1. - 1.g^2\right)^{0.5} kl^2 s} + \frac{0.63662 e^{-\frac{1.c\alpha}{l}} p\beta \cos\left(\frac{sy}{l}\right) \sin\left(\frac{bs}{l}\right) \sin\left(\frac{c\beta}{l}\right) \alpha}{\left(1. - 1.g^2\right)^{0.5} kl^2 s} - \frac{0.31831 e^{-\frac{1.c\alpha}{l}} p\beta^2 \cos\left(\frac{sy}{l}\right) \cos\left(\frac{c\beta}{l}\right) \sin\left(\frac{bs}{l}\right)}{\left(1. - 1.g^2\right)^{0.5} kl^2 s} - \frac{0.31831 e^{-\frac{1.c\alpha}{l}} \nu ps \cos\left(\frac{sy}{l}\right) \cos\left(\frac{c\beta}{l}\right) \sin\left(\frac{bs}{l}\right)}{\left(1. - 1.g^2\right)^{0.5} kl^2} \tag{B.39}$$

$$R10 = \frac{0.202642 d e^{\frac{2c\alpha}{l}} p^2 \alpha\beta \cos^2\left(\frac{sy}{l}\right) \cos^2\left(\frac{c\beta}{l}\right) \sin^2\left(\frac{bs}{l}\right)}{\left(1. - 1.g^2\right)^{1.} k^2 l^2 s^2} + \frac{0.202642 d e^{\frac{2c\alpha}{l}} p^2 \alpha\beta \cos^2\left(\frac{sy}{l}\right) \sin^2\left(\frac{c\beta}{l}\right) \sin^2\left(\frac{bs}{l}\right)}{\left(1. - 1.g^2\right)^{1.} k^2 l^2 s^2} \tag{B.40}$$

$$R11 = \frac{0.31831 d e^{\frac{c\alpha}{l}} p \cos\left(\frac{sy}{l}\right) \cos\left(\frac{c\beta}{l}\right) \sin\left(\frac{bs}{l}\right)}{\left(1. - 1.g^2\right)^{0.5} ks} \left(\frac{e^{-\frac{1.c\alpha}{l}} p \cos\left(\frac{sy}{l}\right) \cos\left(\frac{c\beta}{l}\right) \sin\left(\frac{bs}{l}\right) \beta^3}{\left(1. - 1.g^2\right)^{0.5} kls} - \frac{3.e^{-\frac{1.c\alpha}{l}} p\alpha^2 \cos\left(\frac{sy}{l}\right) \cos\left(\frac{c\beta}{l}\right) \sin\left(\frac{bs}{l}\right) \beta}{\left(1. - 1.g^2\right)^{0.5} kls} - \frac{1.e^{-\frac{1.c\alpha}{l}} \nu ps \cos\left(\frac{sy}{l}\right) \cos\left(\frac{c\beta}{l}\right) \sin\left(\frac{bs}{l}\right) \beta}{\left(1. - 1.g^2\right)^{0.5} kl} + \frac{2.e^{-\frac{1.c\alpha}{l}} ps \cos\left(\frac{sy}{l}\right) \cos\left(\frac{c\beta}{l}\right) \sin\left(\frac{bs}{l}\right) \beta}{\left(1. - 1.g^2\right)^{0.5} kl} + \frac{2.e^{-\frac{1.c\alpha}{l}} gp \cos\left(\frac{sy}{l}\right) \cos\left(\frac{c\beta}{l}\right) \sin\left(\frac{bs}{l}\right) \beta}{\left(1. - 1.g^2\right)^{0.5} kls} + \frac{e^{-\frac{1.c\alpha}{l}} p\alpha \left((\nu - 2.)s^2 + \alpha^2 - 3.\beta^2 - 2.g\right) \cos\left(\frac{sy}{l}\right) \sin\left(\frac{bs}{l}\right) \sin\left(\frac{c\beta}{l}\right)}{\left(1. - 1.g^2\right)^{0.5} kls} \right) \tag{B.41}$$

$$R12 = \frac{0.31831 e^{-\frac{1.c\alpha}{l}} p \cos\left(\frac{sy}{l}\right) \sin\left(\frac{bs}{l}\right) \sin\left(\frac{c\beta}{l}\right)}{(1. - 1.g^2)\, k^2 s^2 l} \left(e^{\frac{c\alpha}{l}} p\alpha \left((\nu - 2.)s^2 + \alpha^2 - 3.\beta^2 - 2.g\right) \cos\left(\frac{sy}{l}\right) \cos\left(\frac{c\beta}{l}\right) \sin\left(\frac{bs}{l}\right) + e^{\frac{c\alpha}{l}} p\beta \left(-1.(\nu - 2.)s^2 - 3.\alpha^2 + \beta^2 + 2.g\right) \cos\left(\frac{sy}{l}\right) \sin\left(\frac{c\beta}{l}\right) \sin\left(\frac{bs}{l}\right) \right) \tag{B.42}$$

$$R13 = \frac{0.31831 e^{-\frac{1.c\alpha}{l}} p \cos\left(\frac{sy}{l}\right) \sin\left(\frac{bs}{l}\right) \sin\left(\frac{c\beta}{l}\right)}{(1. - 1.g^2)^{0.5}\, ks} \left(\frac{0.31831 e^{\frac{c\alpha}{l}} p \cos\left(\frac{sy}{l}\right) \cos\left(\frac{c\beta}{l}\right) \sin\left(\frac{bs}{l}\right) \alpha^2}{(1. - 1.g^2)^{0.5}\, kl^2 s} - \frac{0.63662 e^{\frac{c\alpha}{l}} p\beta \cos\left(\frac{sy}{l}\right) \sin\left(\frac{bs}{l}\right) \sin\left(\frac{c\beta}{l}\right) \alpha}{(1. - 1.g^2)^{0.5}\, kl^2 s} - \frac{0.31831 e^{\frac{c\alpha}{l}} p\beta^2 \cos\left(\frac{sy}{l}\right) \cos\left(\frac{c\beta}{l}\right) \sin\left(\frac{bs}{l}\right)}{(1. - 1.g^2)^{0.5}\, kl^2 s} - \frac{0.31831 e^{\frac{c\alpha}{l}} \nu ps \cos\left(\frac{sy}{l}\right) \cos\left(\frac{c\beta}{l}\right) \sin\left(\frac{bs}{l}\right)}{(1. - 1.g^2)^{0.5}\, kl^2} \right) \tag{B.43}$$

$$R14 = \frac{0.31831 d e^{\frac{c\alpha}{l}} p \cos\left(\frac{sy}{l}\right) \cos\left(\frac{c\beta}{l}\right) \sin\left(\frac{bs}{l}\right)}{(1. - 1.g^2)^{0.5}\, ks} \left(- \frac{1.e^{\frac{c\alpha}{l}} p \cos\left(\frac{sy}{l}\right) \cos\left(\frac{c\beta}{l}\right) \sin\left(\frac{bs}{l}\right) \beta^3}{(1. - 1.g^2)^{0.5}\, kls} + \frac{3.e^{\frac{c\alpha}{l}} p\alpha^2 \cos\left(\frac{sy}{l}\right) \cos\left(\frac{c\beta}{l}\right) \sin\left(\frac{bs}{l}\right) \beta}{(1. - 1.g^2)^{0.5}\, kls} + \frac{e^{\frac{c\alpha}{l}} \nu ps \cos\left(\frac{sy}{l}\right) \cos\left(\frac{c\beta}{l}\right) \sin\left(\frac{bs}{l}\right) \beta}{(1. - 1.g^2)^{0.5}\, kl} - \frac{2.e^{\frac{c\alpha}{l}} ps \cos\left(\frac{sy}{l}\right) \cos\left(\frac{c\beta}{l}\right) \sin\left(\frac{bs}{l}\right) \beta}{(1. - 1.g^2)^{0.5}\, kl} - \frac{2.e^{\frac{c\alpha}{l}} gp \cos\left(\frac{sy}{l}\right) \cos\left(\frac{c\beta}{l}\right) \sin\left(\frac{bs}{l}\right) \beta}{(1. - 1.g^2)^{0.5}\, kls} + \frac{e^{\frac{c\alpha}{l}} p\alpha \left((\nu - 2.)s^2 + \alpha^2 - 3.\beta^2 - 2.g\right) \cos\left(\frac{sy}{l}\right) \sin\left(\frac{bs}{l}\right) \sin\left(\frac{c\beta}{l}\right)}{(1. - 1.g^2)^{0.5}\, kls} \right) \tag{B.44}$$

$$R15 = \frac{0.31831 d e^{\frac{c\alpha}{l}} p \cos\left(\frac{sy}{l}\right) \sin\left(\frac{bs}{l}\right) \sin\left(\frac{c\beta}{l}\right)}{(1. - 1.g^2)\, k^2 s^2 l} \left(e^{\frac{c\alpha}{l}} p\alpha \left((\nu - 2.)s^2 + \alpha^2 - 3.\beta^2 - 2.g\right) \cos\left(\frac{sy}{l}\right) \cos\left(\frac{c\beta}{l}\right) \sin\left(\frac{bs}{l}\right) e^{\frac{c\alpha}{l}} p\beta \left(-1.(\nu - 2.)s^2 - 3.\alpha^2 + \beta^2 + 2.g\right) \cos\left(\frac{sy}{l}\right) \sin\left(\frac{c\beta}{l}\right) \sin\left(\frac{bs}{l}\right) \right) \tag{B.45}$$

$$
\begin{aligned}
Q4 = & \frac{0.31831 e^{-\frac{1.c\alpha}{l}} p \cos\left(\frac{sy}{l}\right) \sin\left(\frac{bs}{l}\right) \sin\left(\frac{c\beta}{l}\right) \alpha^2}{\left(1. - 1.g^2\right)^{0.5} kl^2 s} \\
& - \frac{0.63662 e^{-\frac{1.c\alpha}{l}} p\beta \cos\left(\frac{sy}{l}\right) \cos\left(\frac{c\beta}{l}\right) \sin\left(\frac{bs}{l}\right) \alpha}{\left(1. - 1.g^2\right)^{0.5} kl^2 s} \\
& - \frac{0.31831 e^{-\frac{1.c\alpha}{l}} p\beta^2 \cos\left(\frac{sy}{l}\right) \sin\left(\frac{bs}{l}\right) \sin\left(\frac{c\beta}{l}\right)}{\left(1. - 1.g^2\right)^{0.5} kl^2 s} \\
& - \frac{0.31831 e^{-\frac{1.c\alpha}{l}} \nu ps \cos\left(\frac{sy}{l}\right) \sin\left(\frac{bs}{l}\right) \sin\left(\frac{c\beta}{l}\right)}{\left(1. - 1.g^2\right)^{0.5} kl^2}
\end{aligned}
\tag{B.46}
$$

$$
A1 = 0.31831 e^{-\frac{x\alpha}{l}} p \cos\left(\frac{sy}{l}\right) \cos\left(\frac{x\beta}{l}\right) \sin\left(\frac{bs}{l}\right) \tag{B.47}
$$

$$
\begin{aligned}
B1 = & \frac{0.31831 e^{-\frac{1.c\alpha}{l}} p \cos\left(\frac{sy}{l}\right) \sin\left(\frac{bs}{l}\right) \sin\left(\frac{c\beta}{l}\right) \alpha^2}{\left(1. - 1.g^2\right)^{0.5} kl^2 s} \\
& - \frac{0.63662 e^{-\frac{1.c\alpha}{l}} p\beta \cos\left(\frac{sy}{l}\right) \cos\left(\frac{c\beta}{l}\right) \sin\left(\frac{bs}{l}\right) \alpha}{\left(1. - 1.g^2\right)^{0.5} kl^2 s} \\
& - \frac{0.31831 e^{-\frac{1.c\alpha}{l}} p\beta^2 \cos\left(\frac{sy}{l}\right) \sin\left(\frac{bs}{l}\right) \sin\left(\frac{c\beta}{l}\right)}{\left(1. - 1.g^2\right)^{0.5} kl^2 s} \\
& - \frac{0.31831 e^{-\frac{1.c\alpha}{l}} \nu ps \cos\left(\frac{sy}{l}\right) \sin\left(\frac{bs}{l}\right) \sin\left(\frac{c\beta}{l}\right)}{\left(1. - 1.g^2\right)^{0.5} kl^2}
\end{aligned}
\tag{B.48}
$$

$$
\begin{aligned}
C1 = & \frac{0.202642 de^{\frac{2.c\alpha}{l}} p^2 \alpha\beta \cos^2\left(\frac{sy}{l}\right) \cos^2\left(\frac{c\beta}{l}\right) \sin^2\left(\frac{bs}{l}\right)}{\left(1. - 1.g^2\right)^{1.} k^2 l^2 s^2} \\
& + \frac{0.202642 de^{\frac{2.c\alpha}{l}} p^2 \alpha\beta \cos^2\left(\frac{sy}{l}\right) \sin^2\left(\frac{c\beta}{l}\right) \sin^2\left(\frac{bs}{l}\right)}{\left(1. - 1.g^2\right)^{1.} k^2 l^2 s^2}
\end{aligned}
\tag{B.49}
$$

$$
\begin{aligned}
DD1 = & \frac{e^{\frac{c\alpha}{l}} p\alpha \left((\nu - 2.)s^2 + \alpha^2 - 3.\beta^2 - 2.g\right) \cos\left(\frac{sy}{l}\right) \cos\left(\frac{c\beta}{l}\right) \sin\left(\frac{bs}{l}\right)}{\left(1. - 1.g^2\right)^{0.5} kls} \\
& + \frac{e^{\frac{c\alpha}{l}} p\beta \left(-1.(\nu - 2.)s^2 - 3.\alpha^2 + \beta^2 + 2.g\right) \cos\left(\frac{sy}{l}\right) \sin\left(\frac{c\beta}{l}\right) \sin\left(\frac{bs}{l}\right)}{\left(1. - 1.g^2\right)^{0.5} kls}
\end{aligned}
\tag{B.50}
$$

$$DD2 = \frac{0.31831 e^{-\frac{1.(a+c)\alpha}{l}} p \cos\left(\frac{sy}{l}\right) \sin\left(\frac{bs}{l}\right)}{\left(1. - 1.g^2\right)^{0.5} ks \left(s^4 + 2.gs^2 + 1.\right)} \left(-1.e^{\frac{2.a\alpha}{l}} \sqrt{1. - 1.g^2} \cos\left(\frac{(c-1.a)\beta}{l}\right) + \sqrt{1. - 1.g^2} \cos\left(\frac{(a+c)\beta}{l}\right) + \left(s^2 + g\right) \left(\sin\left(\frac{(a+c)\beta}{l}\right) - 1.e^{\frac{2.a\alpha}{l}} \sin\left(\frac{(c-1.a)\beta}{l}\right) \right) \right) + \frac{0.31831 dp \cos\left(\frac{sy}{l}\right) \sin\left(\frac{bs}{l}\right)}{\left(1. - 1.g^2\right)^{0.5} ks \left(s^4 + 2.gs^2 + 1.\right)} \left(e^{\frac{(a-1.c)\alpha}{l}} \left(\sqrt{1. - 1.g^2} \cos\left(\frac{(c-1.a)\beta}{l}\right) + \left(s^2 + g\right) \sin\left(\frac{(c-1.a)\beta}{l}\right) \right) - 1.e^{-\frac{1.(a+c)\alpha}{l}} \left(\sqrt{1. - 1.g^2} \cos\left(\frac{(a+c)\beta}{l}\right) + \left(s^2 + g\right) \sin\left(\frac{(a+c)\beta}{l}\right) \right) \right) \tag{B.51}$$

$$E1 = \frac{0.31831 de^{\frac{c\alpha}{l}} p \cos\left(\frac{sy}{l}\right) \cos\left(\frac{c\beta}{l}\right) \sin\left(\frac{bs}{l}\right)}{\left(1. - 1.g^2\right)^{0.5} ks} \left(-\frac{1.e^{\frac{c\alpha}{l}} p \cos\left(\frac{sy}{l}\right) \cos\left(\frac{c\beta}{l}\right) \sin\left(\frac{bs}{l}\right) \beta^3}{\left(1. - 1.g^2\right)^{0.5} kls} + \frac{3.e^{\frac{c\alpha}{l}} p\alpha^2 \cos\left(\frac{sy}{l}\right) \cos\left(\frac{c\beta}{l}\right) \sin\left(\frac{bs}{l}\right) \beta}{\left(1. - 1.g^2\right)^{0.5} kls} + \frac{e^{\frac{c\alpha}{l}} \nu ps \cos\left(\frac{sy}{l}\right) \cos\left(\frac{c\beta}{l}\right) \sin\left(\frac{bs}{l}\right) \beta}{\left(1. - 1.g^2\right)^{0.5} kl} - \frac{2.e^{\frac{c\alpha}{l}} ps \cos\left(\frac{sy}{l}\right) \cos\left(\frac{c\beta}{l}\right) \sin\left(\frac{bs}{l}\right) \beta}{\left(1. - 1.g^2\right)^{0.5} kl} - \frac{2.e^{\frac{c\alpha}{l}} gp \cos\left(\frac{sy}{l}\right) \cos\left(\frac{c\beta}{l}\right) \sin\left(\frac{bs}{l}\right) \beta}{\left(1. - 1.g^2\right)^{0.5} kls} + \frac{e^{\frac{c\alpha}{l}} p\alpha \left((\nu - 2.)s^2 + \alpha^2 - 3.\beta^2 - 2.g\right) \cos\left(\frac{sy}{l}\right) \sin\left(\frac{bs}{l}\right) \sin\left(\frac{c\beta}{l}\right)}{\left(1. - 1.g^2\right)^{0.5} kls} \right) \tag{B.52}$$

$$E2 = \frac{0.31831 de^{\frac{c\alpha}{l}} p \cos\left(\frac{sy}{l}\right) \sin\left(\frac{bs}{l}\right) \sin\left(\frac{c\beta}{l}\right)}{\left(1. - 1.g^2\right) k^2 s^2 l} \left(e^{\frac{c\alpha}{l}} p\alpha \left((\nu - 2.)s^2 + \alpha^2 - 3.\beta^2 - 2.g\right) \cos\left(\frac{sy}{l}\right) \cos\left(\frac{c\beta}{l}\right) \sin\left(\frac{bs}{l}\right) e^{\frac{c\alpha}{l}} p\beta \left(-1.(\nu - 2.)s^2 - 3.\alpha^2 + \beta^2 + 2.g\right) \cos\left(\frac{sy}{l}\right) \sin\left(\frac{c\beta}{l}\right) \sin\left(\frac{bs}{l}\right) \right) \tag{B.53}$$

$$G1 = \frac{0.31831 e^{\frac{c\alpha}{l}} p \cos\left(\frac{sy}{l}\right) \cos\left(\frac{c\beta}{l}\right) \sin\left(\frac{bs}{l}\right) \alpha^2}{\left(1. - 1.g^2\right)^{0.5} kl^2 s} - \frac{0.63662 e^{\frac{c\alpha}{l}} p\beta \cos\left(\frac{sy}{l}\right) \sin\left(\frac{bs}{l}\right) \sin\left(\frac{c\beta}{l}\right) \alpha}{\left(1. - 1.g^2\right)^{0.5} kl^2 s} - \frac{0.31831 e^{\frac{c\alpha}{l}} p\beta^2 \cos\left(\frac{sy}{l}\right) \cos\left(\frac{c\beta}{l}\right) \sin\left(\frac{bs}{l}\right)}{\left(1. - 1.g^2\right)^{0.5} kl^2 s} - \frac{0.31831 e^{\frac{c\alpha}{l}} \nu ps \cos\left(\frac{sy}{l}\right) \cos\left(\frac{c\beta}{l}\right) \sin\left(\frac{bs}{l}\right)}{\left(1. - 1.g^2\right)^{0.5} kl^2} \tag{B.54}$$

$$G2 = \frac{0.31831 e^{-\frac{1.(a+c)\alpha}{l}} p \cos\left(\frac{sy}{l}\right) \sin\left(\frac{bs}{l}\right)}{\left(1. - 1.g^2\right)^{0.5} ks \left(s^4 + 2.gs^2 + 1.\right)} \left(-1.e^{\frac{2.a\alpha}{l}} \sqrt{1. - 1.g^2} \cos\left(\frac{(c - 1.a)\beta}{l}\right) + \sqrt{1. - 1.g^2} \cos\left(\frac{(a+c)\beta}{l}\right) + \left(s^2 + g\right) \left(\sin\left(\frac{(a+c)\beta}{l}\right) - 1.e^{\frac{2.a\alpha}{l}} \sin\left(\frac{(c - 1.a)\beta}{l}\right)\right)\right) \tag{B.55}$$

$$G3 = \frac{0.31831 dp \cos\left(\frac{sy}{l}\right) \sin\left(\frac{bs}{l}\right)}{\left(1. - 1.g^2\right)^{0.5} ks \left(s^4 + 2.gs^2 + 1.\right)} \left(e^{\frac{(a-1.c)\alpha}{l}} \left(\sqrt{1. - 1.g^2} \cos\left(\frac{(c - 1.a)\beta}{l}\right) + \left(s^2 + g\right) \sin\left(\frac{(c - 1.a)\beta}{l}\right)\right) - 1.e^{-\frac{1.(a+c)\alpha}{l}} \left(\sqrt{1. - 1.g^2} \cos\left(\frac{(a+c)\beta}{l}\right) + \left(s^2 + g\right) \sin\left(\frac{(a+c)\beta}{l}\right)\right)\right) \tag{B.56}$$

$$G4 = \frac{0.202642 de^{\frac{2.c\alpha}{l}} p^2 \alpha\beta \cos^2\left(\frac{sy}{l}\right) \cos^2\left(\frac{c\beta}{l}\right) \sin^2\left(\frac{bs}{l}\right)}{\left(1. - 1.g^2\right)^{1.} k^2 l^2 s^2} + \frac{0.202642 de^{\frac{2.c\alpha}{l}} p^2 \alpha\beta \cos^2\left(\frac{sy}{l}\right) \sin^2\left(\frac{c\beta}{l}\right) \sin^2\left(\frac{bs}{l}\right)}{\left(1. - 1.g^2\right)^{1.} k^2 l^2 s^2} \tag{B.57}$$

$$H1 = 0.31831 de^{\frac{c\alpha}{l}} p \cos\left(\frac{sy}{l}\right) \cos\left(\frac{c\beta}{l}\right) \sin\left(\frac{bs}{l}\right) \tag{B.58}$$

$$H2 = \frac{e^{-\frac{1.c\alpha}{l}} p \cos\left(\frac{sy}{l}\right) \cos\left(\frac{c\beta}{l}\right) \sin\left(\frac{bs}{l}\right) \beta^3}{\left(1. - 1.g^2\right)^{0.5} kls} - \frac{3.e^{-\frac{1.c\alpha}{l}} p\alpha^2 \cos\left(\frac{sy}{l}\right) \cos\left(\frac{c\beta}{l}\right) \sin\left(\frac{bs}{l}\right) \beta}{\left(1. - 1.g^2\right)^{0.5} kls} - \frac{1.e^{-\frac{1.c\alpha}{l}} \nu ps \cos\left(\frac{sy}{l}\right) \cos\left(\frac{c\beta}{l}\right) \sin\left(\frac{bs}{l}\right) \beta}{\left(1. - 1.g^2\right)^{0.5} kl} + \frac{2.e^{-\frac{1.c\alpha}{l}} ps \cos\left(\frac{sy}{l}\right) \cos\left(\frac{c\beta}{l}\right) \sin\left(\frac{bs}{l}\right) \beta}{\left(1. - 1.g^2\right)^{0.5} kl} + \frac{2.e^{-\frac{1.c\alpha}{l}} gp \cos\left(\frac{sy}{l}\right) \cos\left(\frac{c\beta}{l}\right) \sin\left(\frac{bs}{l}\right) \beta}{\left(1. - 1.g^2\right)^{0.5} kls} + \frac{e^{-\frac{1.c\alpha}{l}} p\alpha \left((\nu - 2.)s^2 + \alpha^2 - 3.\beta^2 - 2.g\right) \cos\left(\frac{sy}{l}\right) \sin\left(\frac{bs}{l}\right) \sin\left(\frac{c\beta}{l}\right)}{\left(1. - 1.g^2\right)^{0.5} kls} \tag{B.59}$$

$$H3 = \left(1 - 1.g^2\right)^{0.5} ks \tag{B.60}$$

$$H4 = \frac{0.31831 e^{-\frac{1.c\alpha}{l}} p \cos\left(\frac{sy}{l}\right) \sin\left(\frac{bs}{l}\right) \sin\left(\frac{c\beta}{l}\right)}{\left(1. - 1.g^2\right) k^2 s^2 l} \left(e^{\frac{c\alpha}{l}} p\alpha \left((\nu - 2.)s^2 + \alpha^2 - 3.\beta^2 - 2.g\right) \cos\left(\frac{sy}{l}\right) \cos\left(\frac{c\beta}{l}\right) \sin\left(\frac{bs}{l}\right) + e^{\frac{c\alpha}{l}} p\beta \left(-1.(\nu - 2.)s^2 - 3.\alpha^2 + \beta^2 + 2.g\right) \cos\left(\frac{sy}{l}\right) \sin\left(\frac{c\beta}{l}\right) \sin\left(\frac{bs}{l}\right)\right) \tag{B.61}$$

$$J123 = \frac{0.31831 e^{-\frac{1.c\alpha}{l}} p \cos\left(\frac{sy}{l}\right) \sin\left(\frac{bs}{l}\right) \sin\left(\frac{c\beta}{l}\right)}{\left(1. - 1.g^2\right)^{0.5} ks} \left(\frac{0.31831 e^{\frac{c\alpha}{l}} p \cos\left(\frac{sy}{l}\right) \cos\left(\frac{c\beta}{l}\right) \sin\left(\frac{bs}{l}\right) \alpha^2}{\left(1. - 1.g^2\right)^{0.5} kl^2 s} - \frac{0.63662 e^{\frac{c\alpha}{l}} p\beta \cos\left(\frac{sy}{l}\right) \sin\left(\frac{bs}{l}\right) \sin\left(\frac{c\beta}{l}\right) \alpha}{\left(1. - 1.g^2\right)^{0.5} kl^2 s} - \frac{0.31831 e^{\frac{c\alpha}{l}} p\beta^2 \cos\left(\frac{sy}{l}\right) \cos\left(\frac{c\beta}{l}\right) \sin\left(\frac{bs}{l}\right)}{\left(1. - 1.g^2\right)^{0.5} kl^2 s} - \frac{0.31831 e^{\frac{c\alpha}{l}} \nu ps \cos\left(\frac{sy}{l}\right) \cos\left(\frac{c\beta}{l}\right) \sin\left(\frac{bs}{l}\right)}{\left(1. - 1.g^2\right)^{0.5} kl^2} \right) \tag{B.62}$$

$$J4 = 0.31831 d e^{\frac{c\alpha}{l}} p \cos\left(\frac{sy}{l}\right) \cos\left(\frac{c\beta}{l}\right) \sin\left(\frac{bs}{l}\right) \tag{B.63}$$

$$\begin{aligned} J5 = & -\frac{1. e^{\frac{c\alpha}{l}} p \cos\left(\frac{sy}{l}\right) \cos\left(\frac{c\beta}{l}\right) \sin\left(\frac{bs}{l}\right) \beta^3}{\left(1. - 1.g^2\right)^{0.5} kls} + \frac{3. e^{\frac{c\alpha}{l}} p\alpha^2 \cos\left(\frac{sy}{l}\right) \cos\left(\frac{c\beta}{l}\right) \sin\left(\frac{bs}{l}\right) \beta}{\left(1. - 1.g^2\right)^{0.5} kls} \\ & + \frac{e^{\frac{c\alpha}{l}} \nu ps \cos\left(\frac{sy}{l}\right) \cos\left(\frac{c\beta}{l}\right) \sin\left(\frac{bs}{l}\right) \beta}{\left(1. - 1.g^2\right)^{0.5} kl} - \frac{2. e^{\frac{c\alpha}{l}} ps \cos\left(\frac{sy}{l}\right) \cos\left(\frac{c\beta}{l}\right) \sin\left(\frac{bs}{l}\right) \beta}{\left(1. - 1.g^2\right)^{0.5} kl} \\ & - \frac{2. e^{\frac{c\alpha}{l}} gp \cos\left(\frac{sy}{l}\right) \cos\left(\frac{c\beta}{l}\right) \sin\left(\frac{bs}{l}\right) \beta}{\left(1. - 1.g^2\right)^{0.5} kls} \\ & + \frac{e^{\frac{c\alpha}{l}} p\alpha \left((\nu - 2.)s^2 + \alpha^2 - 3.\beta^2 - 2.g\right) \cos\left(\frac{sy}{l}\right) \sin\left(\frac{bs}{l}\right) \sin\left(\frac{c\beta}{l}\right)}{\left(1. - 1.g^2\right)^{0.5} kls} \end{aligned} \tag{B.64}$$

$$J6 = \left(1. - 1.g^2\right)^{0.5} ks \tag{B.65}$$

$$\begin{aligned} J7 = & \frac{0.31831 d e^{\frac{c\alpha}{l}} p \cos\left(\frac{sy}{l}\right) \sin\left(\frac{bs}{l}\right) \sin\left(\frac{c\beta}{l}\right)}{\left(1. - 1.g^2\right)^{0.5} kls} \left(e^{\frac{c\alpha}{l}} p\alpha \left((\nu - 2.)s^2 + \alpha^2 - 3.\beta^2 \right.\right. \\ & \left. - 2.g\right) \cos\left(\frac{sy}{l}\right) \cos\left(\frac{c\beta}{l}\right) \sin\left(\frac{bs}{l}\right) \\ & \left. + e^{\frac{c\alpha}{l}} p\beta \left(-1.(\nu - 2.)s^2 - 3.\alpha^2 + \beta^2 + 2.g\right) \cos\left(\frac{sy}{l}\right) \sin\left(\frac{c\beta}{l}\right) \sin\left(\frac{bs}{l}\right) \right) \end{aligned} \tag{B.66}$$

$$J8 = \left(1. - 1.g^2\right)^{0.5} ks \tag{B.67}$$

$$K1 = \tag{B.68}$$
$$-\frac{0.31831 e^{\frac{(a-1.c)\alpha}{l}} \nu ps \cos\left(\frac{sy}{l}\right) \sin\left(\frac{bs}{l}\right) \left(\sqrt{1. - 1.g^2} \cos\left(\frac{(c-1.a)\beta}{l}\right) + (s^2 + g) \sin\left(\frac{(c-1.a)\beta}{l}\right)\right)}{\left(1. - 1.g^2\right)^{0.5} kl^2 \left(s^4 + 2.gs^2 + 1.\right)}$$

$$K2 = \frac{0.31831 e^{-\frac{1.(a+c)\alpha}{l}} \nu ps \cos\left(\frac{sy}{l}\right) \sin\left(\frac{bs}{l}\right) \left(\sqrt{1. - 1.g^2} \cos\left(\frac{(a+c)\beta}{l}\right) + (s^2 + g) \sin\left(\frac{(a+c)\beta}{l}\right)\right)}{\left(1. - 1.g^2\right)^{0.5} kl^2 \left(s^4 + 2.gs^2 + 1.\right)} \tag{B.69}$$

$$K3 = 0.31831e^{-\frac{2.c\alpha}{l}} p\cos\left(\frac{sy}{l}\right)\sin\left(\frac{bs}{l}\right)\left(e^{\frac{(a+c)\alpha}{l}}\left(\sqrt{1.-1.g^2}\alpha^2 - 2.\left(s^2+g\right)\beta\alpha - 1.\sqrt{1.-1.g^2}\beta^2\right)\cos\left(\frac{(c-1.a)\beta}{l}\right) - 1.e^{\frac{(c-1.a)\alpha}{l}}\left(\sqrt{1.-1.g^2}\alpha^2 - 2.\left(s^2+g\right)\beta\alpha - 1.\sqrt{1.-1.g^2}\beta^2\right)\cos\left(\frac{(a+c)\beta}{l}\right) + \left(\left(\alpha^2-1.\beta^2\right)s^2 + 2.\sqrt{1.-1.g^2}\alpha\beta + g\left(\alpha^2-1.\beta^2\right)\right)\left(e^{\frac{(a+c)\alpha}{l}}\sin\left(\frac{(c-1.a)\beta}{l}\right) - 1.e^{\frac{(c-1.a)\alpha}{l}}\sin\left(\frac{(a+c)\beta}{l}\right)\right)\right) \tag{B.70}$$

$$K4 = \left(1.-1.g^2\right)^{0.5} kl^2 s\left(s^4 + 2.gs^2 + 1.\right) \tag{B.71}$$

$$D1 = \left(1-g^2\right)^{0.5} ks\left((L1)\left((L2)\left(L345+L678\right) - 1.\left(L91011\right)\left(M123-M456\right)\right) - 1.\left(M7\right)\left((M8)\left(M91011+M121314\right) - 1.\left(M151617\right)\left(M181920-M212223\right)\right)\right) \tag{B.72}$$

$$\begin{aligned} L1 = {} & \frac{0.31831e^{-\frac{1.c\alpha}{l}} p\cos\left(\frac{sy}{l}\right)\sin\left(\frac{bs}{l}\right)\sin\left(\frac{c\beta}{l}\right)\alpha^2}{\left(1.-1.g^2\right)^{0.5} kl^2 s} \\ & - \frac{0.63662e^{-\frac{1.c\alpha}{l}} p\beta\cos\left(\frac{sy}{l}\right)\cos\left(\frac{c\beta}{l}\right)\sin\left(\frac{bs}{l}\right)\alpha}{\left(1.-1.g^2\right)^{0.5} kl^2 s} \\ & - \frac{0.31831e^{-\frac{1.c\alpha}{l}} p\beta^2\cos\left(\frac{sy}{l}\right)\sin\left(\frac{bs}{l}\right)\sin\left(\frac{c\beta}{l}\right)}{\left(1.-1.g^2\right)^{0.5} kl^2 s} \\ & - \frac{0.31831e^{-\frac{1.c\alpha}{l}} \nu ps\cos\left(\frac{sy}{l}\right)\sin\left(\frac{bs}{l}\right)\sin\left(\frac{c\beta}{l}\right)}{\left(1.-1.g^2\right)^{0.5} kl^2} \end{aligned} \tag{B.73}$$

$$\begin{aligned} L2 = {} & \frac{0.202642de^{\frac{2c\alpha}{l}} p^2\alpha\beta\cos^2\left(\frac{sy}{l}\right)\cos^2\left(\frac{c\beta}{l}\right)\sin^2\left(\frac{bs}{l}\right)}{\left(1.-1.g^2\right)^{1.} k^2 l^2 s^2} \\ & + \frac{0.202642de^{\frac{2c\alpha}{l}} p^2\alpha\beta\cos^2\left(\frac{sy}{l}\right)\sin^2\left(\frac{c\beta}{l}\right)\sin^2\left(\frac{bs}{l}\right)}{\left(1.-1.g^2\right)^{1.} k^2 l^2 s^2} \end{aligned} \tag{B.74}$$

$$\begin{aligned} L345 = {} & \frac{0.31831de^{\frac{c\alpha}{l}} p\cos\left(\frac{sy}{l}\right)\cos\left(\frac{c\beta}{l}\right)\sin\left(\frac{bs}{l}\right)}{\left(1.-1.g^2\right)^{0.5} ks}\left(\frac{e^{-\frac{1.c\alpha}{l}} p\cos\left(\frac{sy}{l}\right)\cos\left(\frac{c\beta}{l}\right)\sin\left(\frac{bs}{l}\right)\alpha^3}{\left(1.-1.g^2\right)^{0.5} kls}\right. \\ & - \frac{3.e^{-\frac{1.c\alpha}{l}} p\beta^2\cos\left(\frac{sy}{l}\right)\cos\left(\frac{c\beta}{l}\right)\sin\left(\frac{bs}{l}\right)\alpha}{\left(1.-1.g^2\right)^{0.5} kls} + \frac{e^{-\frac{1.c\alpha}{l}} \nu ps\cos\left(\frac{sy}{l}\right)\cos\left(\frac{c\beta}{l}\right)\sin\left(\frac{bs}{l}\right)\alpha}{\left(1.-1.g^2\right)^{0.5} kl} \\ & - \frac{2.e^{-\frac{1.c\alpha}{l}} ps\cos\left(\frac{sy}{l}\right)\cos\left(\frac{c\beta}{l}\right)\sin\left(\frac{bs}{l}\right)\alpha}{\left(1.-1.g^2\right)^{0.5} kl} - \frac{2.e^{-\frac{1.c\alpha}{l}} gp\cos\left(\frac{sy}{l}\right)\cos\left(\frac{c\beta}{l}\right)\sin\left(\frac{bs}{l}\right)\alpha}{\left(1.-1.g^2\right)^{0.5} kls} \\ & \left. - \frac{1.e^{-\frac{1.c\alpha}{l}} p\beta\left(-1.(\nu-2.)s^2 - 3.\alpha^2 + \beta^2 + 2.g\right)\cos\left(\frac{sy}{l}\right)\sin\left(\frac{bs}{l}\right)\sin\left(\frac{c\beta}{l}\right)}{\left(1.-1.g^2\right)^{0.5} kls}\right) \end{aligned} \tag{B.75}$$

$$L678 = \frac{0.31831 e^{-\frac{1.c\alpha}{l}} p \cos\left(\frac{sy}{l}\right) \cos\left(\frac{c\beta}{l}\right) \sin\left(\frac{bs}{l}\right)}{(1. - 1.g^2)\, k^2 s^2 l} \left(e^{\frac{c\alpha}{l}} p\alpha \left((\nu - 2.)s^2 + \alpha^2 - 3.\beta^2 - 2.g\right) \cos\left(\frac{sy}{l}\right) \cos\left(\frac{c\beta}{l}\right) \sin\left(\frac{bs}{l}\right) + e^{\frac{c\alpha}{l}} p\beta \left(-1.(\nu - 2.)s^2 - 3.\alpha^2 + \beta^2 + 2.g\right) \cos\left(\frac{sy}{l}\right) \sin\left(\frac{c\beta}{l}\right) \sin\left(\frac{bs}{l}\right) \right) \tag{B.76}$$

$L91011$

$$= \frac{0.31831 e^{-\frac{1.c\alpha}{l}} p \cos\left(\frac{sy}{l}\right) \cos\left(\frac{c\beta}{l}\right) \sin\left(\frac{bs}{l}\right)}{(1. - 1.g^2)^{0.5}\, ks} \left(\frac{0.31831 e^{\frac{c\alpha}{l}} p \cos\left(\frac{sy}{l}\right) \cos\left(\frac{c\beta}{l}\right) \sin\left(\frac{bs}{l}\right) \alpha^2}{(1. - 1.g^2)^{0.5}\, kl^2 s} - \frac{0.63662 e^{\frac{c\alpha}{l}} p\beta \cos\left(\frac{sy}{l}\right) \sin\left(\frac{bs}{l}\right) \sin\left(\frac{c\beta}{l}\right) \alpha}{(1. - 1.g^2)^{0.5}\, kl^2 s} - \frac{0.31831 e^{\frac{c\alpha}{l}} p\beta^2 \cos\left(\frac{sy}{l}\right) \cos\left(\frac{c\beta}{l}\right) \sin\left(\frac{bs}{l}\right)}{(1. - 1.g^2)^{0.5}\, kl^2 s} - \frac{0.31831 e^{\frac{c\alpha}{l}} \nu ps \cos\left(\frac{sy}{l}\right) \cos\left(\frac{c\beta}{l}\right) \sin\left(\frac{bs}{l}\right)}{(1. - 1.g^2)^{0.5}\, kl^2} \right) \tag{B.77}$$

$$M123 = \frac{0.31831 d e^{\frac{c\alpha}{l}} p \cos\left(\frac{sy}{l}\right) \cos\left(\frac{c\beta}{l}\right) \sin\left(\frac{bs}{l}\right)}{(1. - 1.g^2)^{0.5}\, ks} \left(- \frac{1.e^{\frac{c\alpha}{l}} p \cos\left(\frac{sy}{l}\right) \cos\left(\frac{c\beta}{l}\right) \sin\left(\frac{bs}{l}\right) \beta^3}{(1. - 1.g^2)^{0.5}\, kls} + \frac{3.e^{\frac{c\alpha}{l}} p\alpha^2 \cos\left(\frac{sy}{l}\right) \cos\left(\frac{c\beta}{l}\right) \sin\left(\frac{bs}{l}\right) \beta}{(1. - 1.g^2)^{0.5}\, kls} + \frac{e^{\frac{c\alpha}{l}} \nu ps \cos\left(\frac{sy}{l}\right) \cos\left(\frac{c\beta}{l}\right) \sin\left(\frac{bs}{l}\right) \beta}{(1. - 1.g^2)^{0.5}\, kl} - \frac{2.e^{\frac{c\alpha}{l}} ps \cos\left(\frac{sy}{l}\right) \cos\left(\frac{c\beta}{l}\right) \sin\left(\frac{bs}{l}\right) \beta}{(1. - 1.g^2)^{0.5}\, kl} - \frac{2.e^{\frac{c\alpha}{l}} gp \cos\left(\frac{sy}{l}\right) \cos\left(\frac{c\beta}{l}\right) \sin\left(\frac{bs}{l}\right) \beta}{(1. - 1.g^2)^{0.5}\, kls} + \frac{e^{\frac{c\alpha}{l}} p\alpha \left((\nu - 2.)s^2 + \alpha^2 - 3.\beta^2 - 2.g\right) \cos\left(\frac{sy}{l}\right) \sin\left(\frac{bs}{l}\right) \sin\left(\frac{c\beta}{l}\right)}{(1. - 1.g^2)^{0.5}\, kls} \right) \tag{B.78}$$

$$M456 = \frac{0.31831 d e^{\frac{c\alpha}{l}} p \cos\left(\frac{sy}{l}\right) \sin\left(\frac{bs}{l}\right) \sin\left(\frac{c\beta}{l}\right)}{(1. - 1.g^2)\, k^2 s^2 l} \left(e^{\frac{c\alpha}{l}} p\alpha \left((\nu - 2.)s^2 + \alpha^2 - 3.\beta^2 - 2.g\right) \cos\left(\frac{sy}{l}\right) \cos\left(\frac{c\beta}{l}\right) \sin\left(\frac{bs}{l}\right) + e^{\frac{c\alpha}{l}} p\beta \left(-1.(\nu - 2.)s^2 - 3.\alpha^2 + \beta^2 + 2.g\right) \cos\left(\frac{sy}{l}\right) \sin\left(\frac{c\beta}{l}\right) \sin\left(\frac{bs}{l}\right) \right) \tag{B.79}$$

$$
\begin{aligned}
M7 = & \frac{0.31831 e^{-\frac{1.c\alpha}{l}} p \cos\left(\frac{sy}{l}\right) \cos\left(\frac{c\beta}{l}\right) \sin\left(\frac{bs}{l}\right) \alpha^2}{\left(1. - 1.g^2\right)^{0.5} kl^2 s} \\
& + \frac{0.63662 e^{-\frac{1.c\alpha}{l}} p\beta \cos\left(\frac{sy}{l}\right) \sin\left(\frac{bs}{l}\right) \sin\left(\frac{c\beta}{l}\right) \alpha}{\left(1. - 1.g^2\right)^{0.5} kl^2 s} \\
& - \frac{0.31831 e^{-\frac{1.c\alpha}{l}} p\beta^2 \cos\left(\frac{sy}{l}\right) \cos\left(\frac{c\beta}{l}\right) \sin\left(\frac{bs}{l}\right)}{\left(1. - 1.g^2\right)^{0.5} kl^2 s} \\
& - \frac{0.31831 e^{-\frac{1.c\alpha}{l}} \nu ps \cos\left(\frac{sy}{l}\right) \cos\left(\frac{c\beta}{l}\right) \sin\left(\frac{bs}{l}\right)}{\left(1. - 1.g^2\right)^{0.5} kl^2}
\end{aligned} \tag{B.80}
$$

$$
\begin{aligned}
M8 = & \frac{0.202642 d e^{\frac{2c\alpha}{l}} p^2 \alpha\beta \cos^2\left(\frac{sy}{l}\right) \cos^2\left(\frac{c\beta}{l}\right) \sin^2\left(\frac{bs}{l}\right)}{\left(1. - 1.g^2\right)^{1.} k^2 l^2 s^2} \\
& + \frac{0.202642 d e^{\frac{2c\alpha}{l}} p^2 \alpha\beta \cos^2\left(\frac{sy}{l}\right) \sin^2\left(\frac{c\beta}{l}\right) \sin^2\left(\frac{bs}{l}\right)}{\left(1. - 1.g^2\right)^{1.} k^2 l^2 s^2}
\end{aligned} \tag{B.81}
$$

$$
\begin{aligned}
M91011 = & \frac{0.31831 d e^{\frac{c\alpha}{l}} p \cos\left(\frac{sy}{l}\right) \cos\left(\frac{c\beta}{l}\right) \sin\left(\frac{bs}{l}\right)}{\left(1. - 1.g^2\right)^{0.5} ks} \left(\frac{e^{-\frac{1.c\alpha}{l}} p \cos\left(\frac{sy}{l}\right) \cos\left(\frac{c\beta}{l}\right) \sin\left(\frac{bs}{l}\right) \beta^3}{\left(1. - 1.g^2\right)^{0.5} kls} \right. \\
& - \frac{3. e^{-\frac{1.c\alpha}{l}} p\alpha^2 \cos\left(\frac{sy}{l}\right) \cos\left(\frac{c\beta}{l}\right) \sin\left(\frac{bs}{l}\right) \beta}{\left(1. - 1.g^2\right)^{0.5} kls} \\
& - \frac{1. e^{-\frac{1.c\alpha}{l}} \nu ps \cos\left(\frac{sy}{l}\right) \cos\left(\frac{c\beta}{l}\right) \sin\left(\frac{bs}{l}\right) \beta}{\left(1. - 1.g^2\right)^{0.5} kl} \\
& + \frac{2. e^{-\frac{1.c\alpha}{l}} ps \cos\left(\frac{sy}{l}\right) \cos\left(\frac{c\beta}{l}\right) \sin\left(\frac{bs}{l}\right) \beta}{\left(1. - 1.g^2\right)^{0.5} kl} + \frac{2. e^{-\frac{1.c\alpha}{l}} gp \cos\left(\frac{sy}{l}\right) \cos\left(\frac{c\beta}{l}\right) \sin\left(\frac{bs}{l}\right) \beta}{\left(1. - 1.g^2\right)^{0.5} kls} \\
& \left. + \frac{e^{-\frac{1.c\alpha}{l}} p\alpha \left((\nu - 2.)s^2 + \alpha^2 - 3.\beta^2 - 2.g\right) \cos\left(\frac{sy}{l}\right) \sin\left(\frac{bs}{l}\right) \sin\left(\frac{c\beta}{l}\right)}{\left(1. - 1.g^2\right)^{0.5} kls} \right)
\end{aligned} \tag{B.82}
$$

$$
\begin{aligned}
M121314 = & \frac{0.31831 e^{-\frac{1.c\alpha}{l}} p \cos\left(\frac{sy}{l}\right) \sin\left(\frac{bs}{l}\right) \sin\left(\frac{c\beta}{l}\right)}{\left(1. - 1.g^2\right) k^2 s^2 l} \left(e^{\frac{c\alpha}{l}} p\alpha \left((\nu - 2.)s^2 + \alpha^2 - 3.\beta^2 \right.\right. \\
& \left. - 2.g\right) \cos\left(\frac{sy}{l}\right) \cos\left(\frac{c\beta}{l}\right) \sin\left(\frac{bs}{l}\right) \\
& \left. + e^{\frac{c\alpha}{l}} p\beta \left(-1.(\nu - 2.)s^2 - 3.\alpha^2 + \beta^2 + 2.g\right) \cos\left(\frac{sy}{l}\right) \sin\left(\frac{c\beta}{l}\right) \sin\left(\frac{bs}{l}\right) \right)
\end{aligned} \tag{B.83}
$$

$$M151617 = \frac{0.31831 e^{-\frac{1.c\alpha}{l}} p \cos\left(\frac{sy}{l}\right) \sin\left(\frac{bs}{l}\right) \sin\left(\frac{c\beta}{l}\right)}{\left(1. - 1.g^2\right)^{0.5} ks} \left(\frac{0.31831 e^{\frac{c\alpha}{l}} p \cos\left(\frac{sy}{l}\right) \cos\left(\frac{c\beta}{l}\right) \sin\left(\frac{bs}{l}\right) \alpha^2}{\left(1. - 1.g^2\right)^{0.5} kl^2 s} - \frac{0.63662 e^{\frac{c\alpha}{l}} p\beta \cos\left(\frac{sy}{l}\right) \sin\left(\frac{bs}{l}\right) \sin\left(\frac{c\beta}{l}\right) \alpha}{\left(1. - 1.g^2\right)^{0.5} kl^2 s} - \frac{0.31831 e^{\frac{c\alpha}{l}} p\beta^2 \cos\left(\frac{sy}{l}\right) \cos\left(\frac{c\beta}{l}\right) \sin\left(\frac{bs}{l}\right)}{\left(1. - 1.g^2\right)^{0.5} kl^2 s} - \frac{0.31831 e^{\frac{c\alpha}{l}} \nu ps \cos\left(\frac{sy}{l}\right) \cos\left(\frac{c\beta}{l}\right) \sin\left(\frac{bs}{l}\right)}{\left(1. - 1.g^2\right)^{0.5} kl^2} \right) \tag{B.84}$$

$$M181920 = \frac{0.31831 de^{\frac{c\alpha}{l}} p \cos\left(\frac{sy}{l}\right) \cos\left(\frac{c\beta}{l}\right) \sin\left(\frac{bs}{l}\right)}{\left(1. - 1.g^2\right)^{0.5} ks} \left(-\frac{1.e^{\frac{c\alpha}{l}} p \cos\left(\frac{sy}{l}\right) \cos\left(\frac{c\beta}{l}\right) \sin\left(\frac{bs}{l}\right) \beta^3}{\left(1. - 1.g^2\right)^{0.5} kls} + \frac{3.e^{\frac{c\alpha}{l}} p\alpha^2 \cos\left(\frac{sy}{l}\right) \cos\left(\frac{c\beta}{l}\right) \sin\left(\frac{bs}{l}\right) \beta}{\left(1. - 1.g^2\right)^{0.5} kls} + \frac{e^{\frac{c\alpha}{l}} \nu ps \cos\left(\frac{sy}{l}\right) \cos\left(\frac{c\beta}{l}\right) \sin\left(\frac{bs}{l}\right) \beta}{\left(1. - 1.g^2\right)^{0.5} kl} - \frac{2.e^{\frac{c\alpha}{l}} ps \cos\left(\frac{sy}{l}\right) \cos\left(\frac{c\beta}{l}\right) \sin\left(\frac{bs}{l}\right) \beta}{\left(1. - 1.g^2\right)^{0.5} kl} - \frac{2.e^{\frac{c\alpha}{l}} gp \cos\left(\frac{sy}{l}\right) \cos\left(\frac{c\beta}{l}\right) \sin\left(\frac{bs}{l}\right) \beta}{\left(1. - 1.g^2\right)^{0.5} kls} + \frac{e^{\frac{c\alpha}{l}} p\alpha \left((\nu - 2.)s^2 + \alpha^2 - 3.\beta^2 - 2.g\right) \cos\left(\frac{sy}{l}\right) \sin\left(\frac{bs}{l}\right) \sin\left(\frac{c\beta}{l}\right)}{\left(1. - 1.g^2\right)^{0.5} kls} \right) \tag{B.85}$$

$$M212223 = \frac{0.31831 de^{\frac{c\alpha}{l}} p \cos\left(\frac{sy}{l}\right) \sin\left(\frac{bs}{l}\right) \sin\left(\frac{c\beta}{l}\right)}{\left(1. - 1.g^2\right) k^2 s^2} \left(e^{\frac{c\alpha}{l}} p\alpha \left((\nu - 2.)s^2 + \alpha^2 - 3.\beta^2 - 2.g\right) \cos\left(\frac{sy}{l}\right) \cos\left(\frac{c\beta}{l}\right) \sin\left(\frac{bs}{l}\right) + e^{\frac{c\alpha}{l}} p\beta \left(-1.(\nu - 2.)s^2 - 3.\alpha^2 + \beta^2 + 2.g\right) \cos\left(\frac{sy}{l}\right) \sin\left(\frac{c\beta}{l}\right) \sin\left(\frac{bs}{l}\right) \right) \tag{B.86}$$

$$N3 = \frac{1}{\left(1 - g^2\right)^{0.5} k\pi s \left(s^4 + 2gs^2 + 1\right)} p \cos\left(\frac{sy}{l}\right) \sin\left(\frac{bs}{l}\right) \left(e^{-\frac{(x-a)\alpha}{l}} \left(\sqrt{1 - g^2} \cos\left(\frac{(x-a)\beta}{l}\right) + \left(s^2 + g\right) \sin\left(\frac{(x-a)\beta}{l}\right) \right) - e^{-\frac{(a+x)\alpha}{l}} \left(\sqrt{1 - g^2} \cos\left(\frac{(a+x)\beta}{l}\right) + \left(s^2 + g\right) \sin\left(\frac{(a+x)\beta}{l}\right) \right) \right) \tag{B.87}$$